



**UNIVERSIDAD DE INVESTIGACIÓN DE TECNOLOGÍA  
EXPERIMENTAL YACHAY**

**Escuela de Ciencias Físicas y Nanotecnología**

**TÍTULO: Computational studies of the metal-organic framework  
 $\text{Cu}_2(\text{CO}_2)_4 + \text{H}_2\text{ABDC-X}$ , (X = F, Cl, Br): stability, electronic structure,  
and defects.**

Trabajo de integración curricular presentado como requisito para la  
obtención  
del título de FÍSICO

**Autor:**

Eder René Vera Guzmán

**Tutor:**

Ph.D Henry Pinto

**Co-Tutor:**

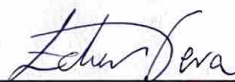
Ph.D Alicja Mikolajczyk

Urcuquí, Julio 2023

## AUTORÍA

Yo, **Vera Guzmán Eder René**, con cédula de identidad **0951198779**, declaro que las ideas, juicios, valoraciones, interpretaciones, consultas bibliográficas, definiciones y conceptualizaciones expuestas en el presente trabajo; así cómo, los procedimientos y herramientas utilizadas en la investigación, son de absoluta responsabilidad de el/la autora (a) del trabajo de integración curricular. Así mismo, me acojo a los reglamentos internos de la Universidad de Investigación de Tecnología Experimental Yachay.

Urcuquí, Julio 2023.



---

Eder René Vera Guzmán

CI: 0951198779

## AUTORIZACIÓN DE PUBLICACIÓN

Yo, **Vera Guzmán Eder René**, con cédula de identidad **0951198779**, cedo a la Universidad de Investigación de Tecnología Experimental Yachay, los derechos de publicación de la presente obra, sin que deba haber un reconocimiento económico por este concepto. Declaro además que el texto del presente trabajo de titulación no podrá ser cedido a ninguna empresa editorial para su publicación u otros fines, sin contar previamente con la autorización escrita de la Universidad.

Asimismo, autorizo a la Universidad que realice la digitalización y publicación de este trabajo de integración curricular en el repositorio virtual, de conformidad a lo dispuesto en el Art. 144 de la Ley Orgánica de Educación Superior.

Urcuquí, Julio 2023.



---

Eder René Vera Guzmán

CI: 0951198779

## Acknowledgements

My sincere gratitude will always be given first to my family: to my parents, Milton Vera and Monica Guzmán for raising a curious boy and supporting every crazy idea along the way. To my siblings, Catherine and Milton for their long-lasting unconditional support and for for being my worst and best friends. I will always love you.

I would also like to thank my dear friends for the enriching talks and for making this journey simply beautiful: *F.V., O.S., M.C., M.V., S.V., A.D., J.G.*, Punto de Encuentro, PAT28, Cabos. To all of you, you will always be remembered.

In the same way, I am immensely grateful to all professors at Yachay Tech for their continuous guidance and encouragement, many of whom did more than just teach, in particular, to my advisor and friend Henry Pinto. I would also like to offer my heartfelt appreciation to Alicja Mikolajczyk for co-advising this work.

Many thanks to Yachay Tech University for being my home all these years. Special thanks to Task Supercomputer Center in Gdańsk for sharing computational resources for the good of science.



*To Samantha, because life just seems simple when we are together. You have bettered me in every possible way. You make seem unreasonable applying the laws of physics to explain a world without you. To you, my love.*

*Eder V.*



## Abstract

In the light of new technologies to fight climate change, MOFs are proven to be quite useful. Metal-organic frameworks (MOFs) are porous materials formed by linking organic units with metal clusters as nodes (SBU). Large porosity and surface area values make them a good candidate for any application where storage is involved (e.g., drug delivery, water harvesting, hydrogen and methane storage, carbon dioxide capture, and catalysis applications.) In this work, we have presented spin-density functional theory calculations (spin-DFT) to study the electronic properties of three different MOFs based on copper SBU and functionalized linker ABDC-X, X = F, Cl, Br (cf. Fig 3.7 from ref<sup>1</sup>) to assess photocatalytic applications. Electronic relaxation with meta-GGA functionals (r<sup>2</sup>SCAN + rVV10) yielded an antiferromagnetic phase (AFM2) as the optimal state. All AFM2 structures show band gap energies inside the visible spectra,  $E_g = 2.5 - 2.7$  eV showing good photoabsorption capabilities. Spin projected atomic density of states calculated with hybrid functional HSE06 displays ligand-to-metal (LMCT) and ligand-to-ligand (LLCT) charge transfer band gap excitations are present in all stable MOFs, which creates charge-separated states essential for photocatalysis. Aligned band edge positions against redox potentials of water splitting and CO<sub>2</sub> reduction enabled MOF photocatalysis activity evaluation. Our findings encourage the application of copper based MOF functionalized with ABDC-X for photocatalytic water splitting and CO<sub>2</sub> reduction. Future research will focus on ABDC-X functionalization with X = I, NH<sub>2</sub>, NO<sub>2</sub>, and explore other type of defects that could present even better electronic properties.

**Keywords:** MOF, DFT, magnetism, ABDC, LMCT, photocatalysis, CO<sub>2</sub> reduction.





## Resumen

A la luz de las nuevas tecnologías de lucha contra el cambio climático, los MOFs han demostrado ser bastante útiles. Las estructuras metal-orgánicas (MOF, por sus siglas en inglés) son materiales porosos formados por la unión de unidades orgánicas con clústeres metálicos como nodos (SBU). Sus altos valores de porosidad y área superficial los convierten en buenos candidatos para cualquier aplicación que implique almacenamiento (por ejemplo, entrega de fármacos, captación de agua, almacenamiento de hidrógeno y metano, captura de dióxido de carbono, así como también aplicaciones de catálisis). En este trabajo, se presenta cálculos de teoría funcional de densidad de espín (spin-DFT) para estudiar las propiedades electrónicas de tres MOFs diferentes construidos a partir de nodos de cobre y ligando ABDC-X funcionalizado con X = F, Cl, Br, para evaluar sus aplicaciones fotocatalíticas. La relajación electrónica con funcionales meta-GGA ( $r^2$ SCAN + rVV10) dio como resultado que la fase antiferromagnética (AFM2) es la más óptima. Todas las estructuras AFM2 muestran energías de banda dentro del espectro visible,  $E_g = 2,5 - 2,7$  eV mostrando buenas capacidades de fotoabsorción. La densidad de estados atómica proyectada de spin calculada con el funcional híbrido HSE06 muestra que las excitaciones de carga de ligando a metal (LMCT) y de ligando a ligando (LLCT) están presentes en todos los MOF estables, lo que crea estados separados de carga esenciales para la fotocatalisis. Alineación de las posiciones de las energías de banda con los potenciales redox de división de agua y reducción de CO<sub>2</sub> permitió la evaluación de la actividad de fotocatalisis de los MOFs. Nuestros resultados alientan la aplicación de MOF basados en SBU de cobre y ligando ABDC-X funcionalizado con X = F, Cl, Br para la división fotocatalítica del agua y la reducción de CO<sub>2</sub>. La investigación futura se centrará en la funcionalización de ABDC-X, X = I, NH<sub>2</sub>, NO<sub>2</sub>, así como explorar otros tipos de defectos que podrían presentar propiedades electrónicas aún mejores.

**Palabras claves:** DFT, magnetismo, ABDC, LMCT, fotocatalisis, reducción de CO<sub>2</sub>.



# Contents

<b>List of Figures</b>	<b>xii</b>
<b>List of Tables</b>	<b>xvi</b>
<b>1 Introduction</b>	<b>1</b>
1.1 Problem Statement . . . . .	3
1.2 General and Specific Objectives . . . . .	3
1.3 Overview . . . . .	4
<b>2 Theoretical Background</b>	<b>7</b>
2.1 Many-Body Schrödinger equation . . . . .	7
2.1.1 Hartree-Fock equations . . . . .	9
2.2 Density Functional Theory . . . . .	10
2.2.1 Hohenberg-Khon theorem . . . . .	11
2.2.2 Kohn-Sham equations . . . . .	11
2.2.3 DFT Functionals . . . . .	12
2.3 Density Functional Theory and magnetic materials . . . . .	14
2.3.1 The Dirac equation and Spin . . . . .	15
2.3.2 Spin in Density Functional Theory . . . . .	16
2.4 Computational methods . . . . .	17
2.4.1 Plane Waves . . . . .	17
2.4.2 Pseudopotentials . . . . .	18
2.4.3 Vienna ab initio Simulation Package (VASP) . . . . .	18
2.4.4 Density functional tight binding (DFTB+) . . . . .	18
2.4.5 Birch-Murnaghan equation of state . . . . .	19

2.5	Density of States . . . . .	19
2.5.1	Local Density of States . . . . .	20
<b>3</b>	<b>Methodology</b>	<b>21</b>
3.1	Construction of MOF . . . . .	21
3.1.1	Introducing magnetic order . . . . .	23
3.1.2	Introducing defects . . . . .	24
3.2	Relaxation using DFTB+ . . . . .	24
3.3	VASP implementation . . . . .	24
3.4	Band Alignment . . . . .	25
<b>4</b>	<b>Results and Discussion</b>	<b>29</b>
4.1	The M5-F . . . . .	29
4.1.1	Cut-off energy and k-Points . . . . .	29
4.1.2	Bulk Structure . . . . .	32
4.1.3	Density of States & Band Alignment . . . . .	33
4.2	M5-Cl . . . . .	37
4.2.1	Bulk Structure . . . . .	37
4.2.2	Density of States & Band Alignment . . . . .	39
4.3	M5-Br . . . . .	42
4.3.1	Bulk Structure . . . . .	42
4.3.2	Density of States & Band Alignment . . . . .	44
4.4	Photocatalysis Activity . . . . .	47
4.5	Defects . . . . .	50
4.5.1	Zirconium substitution (Def-Zr) . . . . .	50
4.5.2	Magnesium substitution (Def-Mg) . . . . .	52
<b>5</b>	<b>Conclusions &amp; Outlook</b>	<b>55</b>
<b>A</b>	<b>Detailed spin-projected atomic-pDOS</b>	<b>57</b>
<b>B</b>	<b>Detailed spin-projected atomic orbital-pDOS</b>	<b>61</b>
	<b>Bibliography</b>	<b>77</b>

# List of Figures

1.1	3D periodic view of MOF using a copper SBU connected by functionalized ABDC linker. Color code: gray, C; red, O; white, H; salmon, Cu; blue, N; light green, F. . . . .	5
3.1	<b>a)</b> ditopic carboxylate linker functionalized by monosubstitution by X = F, Cl Br, and a 4-connecting dinuclear paddle-wheel copper-based secondary building unit <b>b)</b> periodic representation of M5. Color code: gray, C; red, O; white, H; salmon, Cu; blue, N; light blue, substituent X. . . . .	22
3.2	Unit cell of M5 displaying four different magnetic order: <b>a)</b> non-magnetic (NM), <b>b)</b> ferromagnetic (FM), <b>c)</b> antiferromagnetic type A (AFM1), <b>d)</b> antiferromagnetic type C (AFM2). Color code same as Fig 3.1. H atoms are omitted for simplicity. . . . .	26
3.3	Unit cell of M5 with a different atom introduced to one SBU simulating defect: <b>a)</b> magnesium (green), <b>b)</b> zirconium (bigger light blue. Color code same as Fig 3.1. H atoms are omitted for simplicity) . . . . .	27
3.4	<b>a)</b> M5-F unit cell enclosing a 9 Å-radius yellow sphere representing the main pore. <b>b)</b> Contour map of electrostatic potential at the main pore. Dashed circles of radii = 1, 2, 4 Å are plotted to give an idea of the sampled area for vacuum level calculation. Color code same as Fig 3.1. H atoms are omitted for simplicity . . . . .	28
4.1	<b>a)</b> Plane wave cut-off energy convergence of M5-F. Inset displays a zoom of 1 meV/atom showing convergence starts at 850 eV. <b>b)</b> Energy convergence as a function of $k$ -points in terms of $\Delta k/2\pi$ . . . . .	30
4.2	Birch-Murnaghan equation of states of M5-F fitted with data obtained by relaxation with functionals $r^2$ SCAN+rVV10. To the right a zoom of the dashed-selected area. . . . .	31

4.3	Spin-separated atomic pDOS ( $r^2$ SCAN+rVV10//HSE06) for all M5-F magnetic configurations. Band gap ( $E_g$ ) and band edge positions are aligned with their vacuum level according to table 4.2. Nomenclature is given by MOF name-SBU functionalization-Magnetic state (e.g. M5-F-NM). Workfunction is represented by the Greek letter $\Phi$ . . . . .	35
4.4	Contour plot of 2D sections at half the distance of the lattice vectors showing the electrostatic potential of M5-F-AFM2. The intersection of the three planes is taken as the center of the pore. In the bottom, each 2D plane with their corresponding Miller indices. Color code same as Fig 4.3. . . . .	36
4.5	Birch-Murnaghan equation of states of M5-Cl fitted with data obtained by relaxation with functionals $r^2$ SCAN+rVV10. . . . .	38
4.6	Spin-separated atomic pDOS ( $r^2$ SCAN+rVV10//HSE06) for all MOF-Cl magnetic configurations. Band gap ( $E_g$ ) and band edge positions are aligned with their vacuum level according to table 4.4. Nomenclature is given by MOF name-SBU functionalization-Magnetic state (e.g. M5-Cl-NM). Workfunction is represented by the greek letter $\Phi$ . . . . .	40
4.7	Contour plot of 2D sections at half the distance of the lattice vectors showing the electrostatic potential of M5-Cl-AFM2. The intersection of the three planes is taken as the center of the pore. In the bottom, each 2D plane with the corresponding Miller indices. Color code same as Fig 4.6. . . . .	41
4.8	Birch-Murnaghan equation of states of M5-Br fitted with data obtained by relaxation with functionals $r^2$ SCAN+rVV10. . . . .	43
4.9	Spin-separated atomic pDOS ( $r^2$ SCAN+rVV10//HSE06) for all MOF-Br magnetic configurations. Band gap ( $E_g$ ) and band edge positions are aligned with their vacuum level according to table 4.6. Nomenclature is given by MOF name-SBU functionalization-Magnetic state (e.g. M5-Br-NM). Workfunction is represented by the greek letter $\Phi$ . . . . .	45
4.10	Contour plot of 2D sections at half the distance of the lattice vectors showing the electrostatic potential of M5-Br-AFM2. The intersection of the three planes is taken as the center of the pore. In the bottom, each 2D plane with the corresponding Miller indices. Color code same as Fig. 4.9. . . . .	46
4.11	Absolute band edge positions and bangaps for magnetic states of MOF-F, Cl, Br. Magenta dashed lines represent energy levels corresponding to redox potentials for water splitting, and the green and dark yellow lines represent energy levels corresponding to redox potentials for various CO <sub>2</sub> reduction reactions as listed in Table 4.7. A zoom of the region of interest is depicted in the bottom. . . . .	48

4.12	Absolute band edge positions and band gaps of all AFM2 states. Purple, green and dark yellow dashed lines represent the same redox potential energy as Fig 4.11. Although some CO <sub>2</sub> reduction reactions fall above the LUCO, they still overlap with available states in the CBM. . . . .	49
4.13	<b>a)</b> Aligned spin-separated atomic pDOS (r <sup>2</sup> SCAN+rVV10//HSE06) of Def-Zr, <b>b)</b> 3D view of Def-Zr with electrostatic potential 2D sections contour map at half the distance of lattice vectors. . . . .	51
4.14	<b>a)</b> Aligned spin-separated atomic pDOS (r <sup>2</sup> SCAN+rVV10//HSE06) of Def-Mg, <b>b)</b> 3D view of Def-Mg with electrostatic potential 2D sections contour map at half the distance of lattice vectors. . . . .	53
4.15	Absolute band edge positions and band gaps of Def-Zr, Mg. Purple, green and dark yellow dashed lines represent the same redox potential energy as Fig 4.11. Although some CO <sub>2</sub> reduction reactions fall above the LUCO, they still overlap with available states in the CBM. . . . .	54
A.1	r <sup>2</sup> SCAN+rVV10//HSE06 detailed atomic partial density of states for all M5-F magnetic configurations: antiferromagnetic AFM, ferromagnetic FM and non-magnetic NM. . . . .	58
A.2	r <sup>2</sup> SCAN+rVV10//HSE06 detailed atomic partial density of states for all M5-Cl magnetic configurations: antiferromagnetic AFM, ferromagnetic FM and non-magnetic NM. . . . .	59
A.3	r <sup>2</sup> SCAN+rVV10//HSE06 detailed atomic partial density of states for all M5-Br magnetic configurations: antiferromagnetic AFM, ferromagnetic FM and non-magnetic NM. . . . .	60
B.1	r <sup>2</sup> SCAN+rVV10//HSE06 detailed atomic orbital partial density of states of M5-F-NM. . . . .	62
B.2	r <sup>2</sup> SCAN+rVV10//HSE06 detailed atomic orbital partial density of states of M5-F-FM. . . . .	63
B.3	r <sup>2</sup> SCAN+rVV10//HSE06 detailed atomic orbital partial density of states of M5-F-AFM1. . . . .	64
B.4	r <sup>2</sup> SCAN+rVV10//HSE06 detailed atomic orbital partial density of states of M5-F-AFM2. . . . .	65
B.5	r <sup>2</sup> SCAN+rVV10//HSE06 detailed atomic orbital partial density of states of M5-Cl-NM. . . . .	66
B.6	r <sup>2</sup> SCAN+rVV10//HSE06 detailed atomic orbital partial density of states of M5-Cl-FM. . . . .	67
B.7	r <sup>2</sup> SCAN+rVV10//HSE06 detailed atomic orbital partial density of states of M5-Cl-AFM1. . . . .	68
B.8	r <sup>2</sup> SCAN+rVV10//HSE06 detailed atomic orbital partial density of states of M5-Cl-AFM2. . . . .	69
B.9	r <sup>2</sup> SCAN+rVV10//HSE06 detailed atomic orbital partial density of states of M5-Br-NM. . . . .	70
B.10	r <sup>2</sup> SCAN+rVV10//HSE06 detailed atomic orbital partial density of states of M5-Br-FM. . . . .	71
B.11	r <sup>2</sup> SCAN+rVV10//HSE06 detailed atomic orbital partial density of states of M5-Br-AFM1. . . . .	72
B.12	r <sup>2</sup> SCAN+rVV10//HSE06 detailed atomic orbital partial density of states of M5-Br-AFM2. . . . .	73
B.13	r <sup>2</sup> SCAN+rVV10//HSE06 detailed atomic orbital partial density of states of Def-Zr. . . . .	74



B.14  $r^2$ SCAN+rVV10//HSE06 detailed atomic orbital partial density of states of Def-Mg. . . . 75

# List of Tables

2.1	Jacob’s ladder of DFT functionals adapted from Mancuso et al <sup>2</sup> . As accuracy increases so does the computational cost. In this table, the computational cost increases from bottom to top. Some common functionals are also listed. . . . .	13
4.1	Computed r <sup>2</sup> SCAN+rVV10 crystallographic data and properties of all four M5-F magnetic states: antiferromagnetic AFM, ferromagnetic FM and non-magnetic NM. <i>a, b, c</i> are the lattice parameters and the corresponding angles $\alpha, \beta$ and $\gamma$ . The optimal volume <i>V</i> , bulk modulus <i>B</i> <sub>0</sub> . The relative energy $\Delta E$ with respect to the most stable phase AFM2 and the absolute values of the local magnetic moment $ m_{\text{Cu}} $ at the Cu sites are computed from the r <sup>2</sup> SCAN+rVV10//HSE06 results. . . . .	32
4.2	Mean electrostatic potential at pore for each M5-F magnetic state. . . . .	34
4.3	Computed r <sup>2</sup> SCAN+rVV10 crystallographic data and properties of all four M5-Cl magnetic states: antiferromagnetic AFM, ferromagnetic FM and non-magnetic NM. <i>a, b, c</i> are the lattice parameters and the corresponding angles $\alpha, \beta$ and $\gamma$ . The optimal volume <i>V</i> , bulk modulus <i>B</i> <sub>0</sub> . The relative energy $\Delta E$ with respect to the most stable phase AFM2 and the absolute values of the local magnetic moment $ m_{\text{Cu}} $ at the Cu sites are computed from the r <sup>2</sup> SCAN+rVV10//HSE06 results. . . . .	37
4.4	Mean electrostatic potential at pore for each M5-Cl magnetic state. . . . .	39
4.5	Computed r <sup>2</sup> SCAN+rVV10 crystallographic data and properties of all four M5-Br magnetic states: antiferromagnetic AFM, ferromagnetic FM and non-magnetic NM. <i>a, b, c</i> are the lattice parameters and the corresponding angles $\alpha, \beta$ and $\gamma$ . The optimal volume <i>V</i> , bulk modulus <i>B</i> <sub>0</sub> . The relative energy $\Delta E$ with respect to the most stable phase AFM2 and the absolute values of the local magnetic moment $ m_{\text{Cu}} $ at the Cu sites are computed from the r <sup>2</sup> SCAN+rVV10//HSE06 results. . . . .	42
4.6	Mean electrostatic potential at pore for each M5-Br magnetic state. . . . .	44

4.7	Standard electrode potentials ( $\varepsilon^\circ$ , in V) and $\Delta G$ (in eV) at pH = 7 and T = 298.15 ) of selected reactions. Taken from <sup>3</sup> . . . . .	50
4.8	Computed r <sup>2</sup> SCAN+rVV10 crystallographic data and properties of Def-Zr, Mg. $a$ , $b$ , $c$ are the lattice parameters and the corresponding angles $\alpha$ , $\beta$ and $\gamma$ . The optimal volume $V$ , bulk modulus $B_0$ . The relative energy $\Delta E$ with respect to the most stable phase AFM2 and the absolute values of the local magnetic moment $ m_{\text{Cu}} $ at the Cu sites are computed from the r <sup>2</sup> SCAN+rVV10/HSE06 results. . . . .	52

# Chapter 1

## Introduction

The manipulation of materials has always characterized how we live and progress. We have even named entire periods after the predominant material used (Stone, Bronze, Iron ages). The development of modern technology is based mainly on semiconductors, and some may not be wrong to call the current period The Silicon Age. However, as science and technology progress, we explore different and more complex materials. Nanoscience combines the fields of physics, chemistry, and nanotechnology to develop nanomaterials with applications in energy, the electronic industry, solar cells, and biotechnology, to name some of the fields.

The history of nanomaterials can be traced back to the early 20th century, with the proposal of the existence of 'nanoparticles' by Richard Feynman in his famous 1959 seminar 'There's Plenty of Room at the Bottom'<sup>4</sup>. However, it was not until much later that a proper definition categorized materials of dimensions in the range of 1 to 100 nm as nanomaterials. The invention of various spectroscopic techniques sped up innovation and research in nanotechnology. IBM researchers developed scanning tunneling microscopy (STM) in 1982, and with STM, it became feasible to obtain images of single atoms on surfaces. Atomic force microscopy (AFM) was invented in 1986, and it is regarded as the most crucial scanning probe microscope technique which fed the current progress of materials science at the time. Nowadays, we have vast ways of producing and characterizing nanomaterials, both experimental and computationally. Density-functional theory (DFT) is a powerful computational approach to study nanostructures, molecules, solids, surfaces, and interfaces by solving the electronic structure using quantum mechanics<sup>5</sup>.

Metal-organic frameworks (MOFs) are a relatively new kind of material that has been gaining pop-

ularity due to their diverse applications in the storage of fuels (hydrogen and methane), carbon dioxide capture<sup>6</sup>, and catalysis applications<sup>7</sup>, among others<sup>8</sup>. MOFs result from linking metal ions or clusters, also called secondary building units (SBUs), with organic linkers. The flexibility of their geometry, size, and functionality has allowed a vast landscape of materials with modular properties, sharing, however, one similarity: crystalline structures with a typical porosity greater than 50% of the total volume as well as surface area values of 1000 to 10000m<sup>2</sup>/g,<sup>6</sup>. In recent years, the number of reported MOF structures has increased exponentially. Although at first, linkers such as bipyridines and nitriles were used, they were later replaced by charged chelating linkers with binding groups such as carboxylates, phosphates, tetrazolates, pyrazolates, catecholates, and imidazolates<sup>1</sup>. These organic linkers can have 2 to 12 points of extension, and we refer to them as ditopic, tritopic, tetratopic, etc. The number of extensions gives the number of connections a linker can make. The base of the organic linker used in this work uses two benzene as extending units connected by a nitrogen-nitrogen bridge and have a carboxyl group at each end, which is a ditopic linker with an offset in its geometry due to the nitrogen-nitrogen bond.

The secondary building units (SBUs) are typically polynuclear clusters of metal ions, where the binding groups of the linkers are an intrinsic part of these units. In the structures of carboxylate-based MOFs, as the one being studied in this work, the carboxylates can bind to the metal centers in different ways: ionic bonds, unidentate, symmetric chelating binding modes, and a variety of bridging binding modes, where the nature of the R-COO-M bond ranges from purely ionic to partially covalent. The connectivity of SBUs ranges from 3 to 12. The precise geometry of the linker and the SBU defines the resulting topology of the framework<sup>9</sup>. In this work, we use a dinuclear paddle wheel copper-based SBU, in which each ion is coordinated in a square-pyramidal fashion by four oxygen of the bridging carboxylates, periodic representation can be seen in Fig. 1.1

On the other hand, inspired by the natural photosynthesis of plants, photocatalytic CO<sub>2</sub> reduction is also known as artificial photosynthesis that converts CO<sub>2</sub> through solar energy to produce carbon-based fuels, such as CO, CH<sub>3</sub>OH, HCOOH, CH<sub>4</sub> and other chemicals<sup>10</sup>. In this context, MOFs have attracted great attention of researchers in the fields of material and photocatalysis as they show certain similarities to semiconductors.

## 1.1 Problem Statement

Humankind is probably facing its greatest problem, climate change, affecting our planet and its inhabitants completely. There is no excuse not to be involved in the path to avoid a climate disaster. One way to tackle global warming is to change how we produce, consume, and recycle energy. In this context, new technologies are being created every day. Metal-organic frameworks (MOFs) have been considered a good option for emerging technologies such as carbon capture and storage, water harvesting<sup>11</sup>, catalysis and photovoltaic materials among others<sup>8</sup>.

In this work, we study the electronic structure of copper-based MOF  $\text{Cu}_2(\text{CO}_2)_4$  with the organic linker, (E)-4,4'-(diazene-1,2-diyl)bis(2-methylbenzoic acid), which we'll call by its abbreviation  $\text{H}_2\text{ABDC}$  (cf. Fig 3.7 from ref<sup>1</sup>), functionalized by monosubstitution for photocatalytic purposes.

## 1.2 General and Specific Objectives

The main goal of this thesis is to study the properties of a metal-organic framework based on a 4-connecting dinuclear paddle-wheel copper-based secondary building unit,  $\text{Cu}_2(\text{CO}_2)_4$ , and the variations of the functionalized organic linker  $\text{H}_2\text{ABDC-X}$ , where substituent  $\text{X} = \text{F}, \text{Cl}, \text{Br}$ .

Specific objectives of this work include:

- Describe the theoretical background of DFT including spin-polarized calculations and apply it to study metal-organic framework systems.
- Compute mechanical properties and stability of MOFs studied in this work considering different magnetic phases.
- Predict the electronic structure of MOFs using spin-polarized DFT calculations employing meta-GGA and hybrid functionals
- Predict the valence and conduction band edge energy positions respect to the vacuum energy with electronic structure calculations using hybrid functionals.
- Screen out potential candidates for photocatalysis based on redox potential energy levels.

### **1.3 Overview**

The first chapter states the problem and the motivation to execute this work. Chapter 2, will state the basis and the development of density-functional theory. To make the analysis simpler, some approximations will be performed. Finally, since the results performed with DFT would depend on the type of functionals we use to compute the electronic structure, these will also be explained. In Chapter 3, I will describe the computational procedure, that is, DFTB+ and VASP calculations. Chapter 4 focuses on the results and discusses the three different MOFs structures. Finally, in Chapter 5, I present the conclusions and outlook of this work.

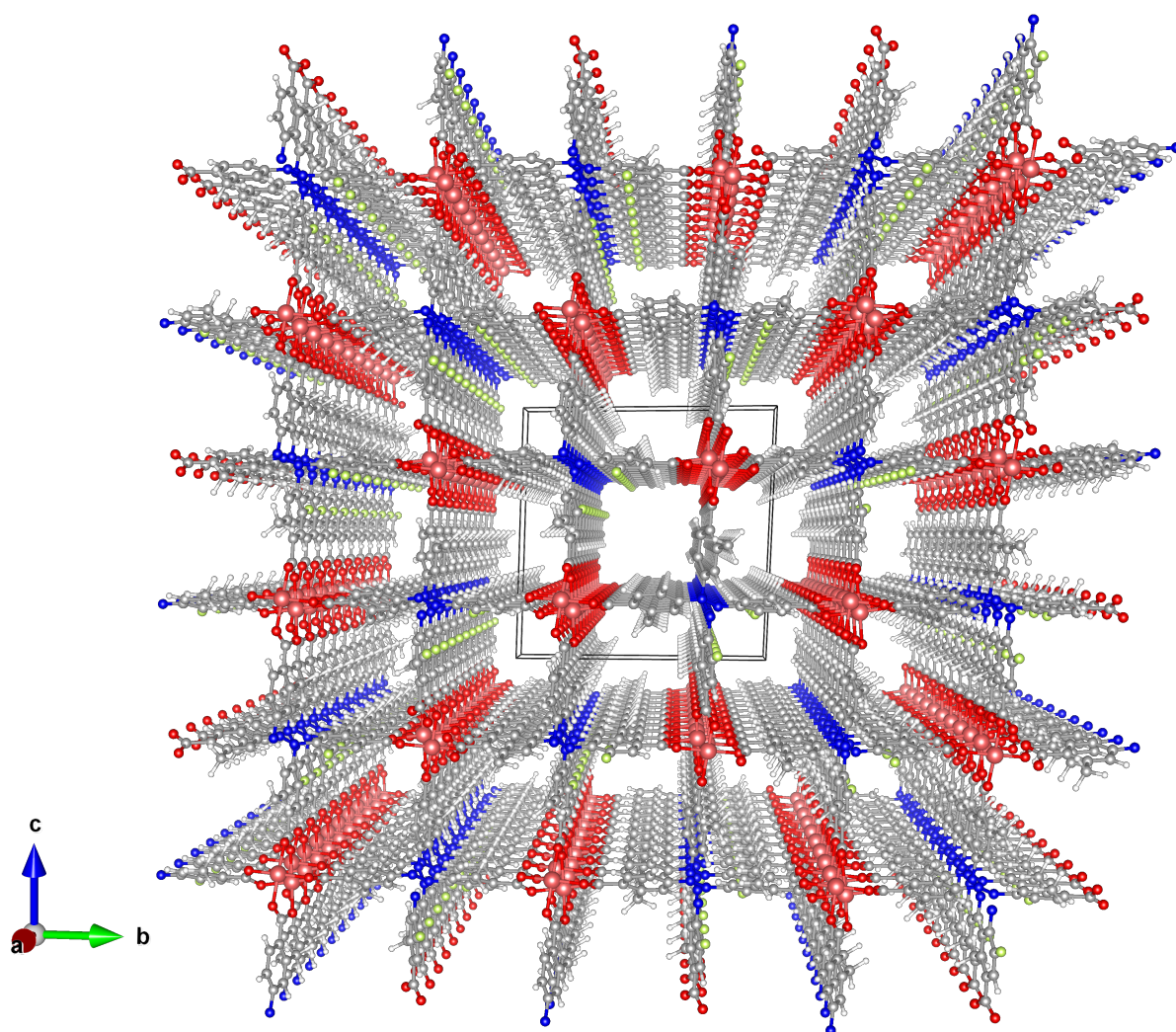


Figure 1.1: 3D periodic view of MOF using a copper SBU connected by functionalized ABDC linker. Color code: gray, C; red, O; white, H; salmon, Cu; blue, N; light green, F.





## Chapter 2

# Theoretical Background

This chapter is mainly dedicated to the foundations and the formalism of density functional theory. In the same way, how we can apply these concepts to metal-organic frameworks and the procedure to perform calculations using the Vienna Ab Initio Package.

### 2.1 Many-Body Schrödinger equation

From quantum mechanics, we learn that in order to understand the behavior of quantum particles we must solve the Schrödinger equation and determine the wavefunction,  $\psi(r)$ , where  $r$  denotes position. If we only consider the stationary electronic states, then we are left with the time-independent version of the Schrödinger equation (TISE), the TISE has the following form:

$$(K + V)\psi = E\psi \quad (2.1)$$

where  $K$  and  $V$  represent the kinetic and potential energy and  $E$  is the total energy eigenvalue for the stationary state described by the wavefunction  $\psi$ . For a given electron eqn 2.1 can be written as:

$$\left[ \frac{\mathbf{p}^2}{2m_e} + V(\mathbf{r}) \right] \psi(\mathbf{r}) = E\psi(\mathbf{r}) \quad (2.2)$$

where  $m_e$  is the electron mass and  $\mathbf{p}$  is the quantum mechanical momentum operator. Suppose now that we add many electrons and nuclei, we get what it is called the many-body wavefunction,  $\Psi$ , which depends on each electron and nuclei's position. For  $N$  electrons and  $M$  nuclei their coordinates are given by  $r_1, r_2, \dots, r_N$  and  $R_1, R_2, \dots, R_M$ , respectively and so we have:

$$\Psi = \Psi(r_1, r_2, \dots, r_N; R_1, R_2, \dots, R_M) \quad (2.3)$$

Now, if we consider the many-body wavefunction,  $\Psi$ , instead of the single-particle wavefunction,  $\psi$ , eqn 2.1 takes the form of:

$$\left[ \underbrace{-\sum_i \frac{\hbar^2}{2m_e} \nabla_i^2}_{K_{electrons}} - \underbrace{\sum_I \frac{\hbar^2}{2M_I} \nabla_I^2}_{K_{nuclei}} + \underbrace{\frac{1}{2} \sum_{i \neq j} \frac{e^2}{4\pi\epsilon_0} \frac{1}{|\mathbf{r}_i - \mathbf{r}_j|}}_{V_{e-e}} + \underbrace{\frac{1}{2} \sum_{I \neq J} \frac{e^2}{4\pi\epsilon_0} \frac{Z_I Z_J}{|\mathbf{R}_I - \mathbf{R}_J|}}_{V_{n-n}} - \underbrace{\sum_{i,I} \frac{e^2}{4\pi\epsilon_0} \frac{Z_I}{|\mathbf{r}_i - \mathbf{R}_I|}}_{V_{e-n}} \right] \Psi = E_{tot} \Psi \quad (2.4)$$

where the first two terms represent the kinetic energy of each electron and nuclei, respectively. In the same way, the last three terms represent the potential energy between electron-electron, nucleus-nucleus and electron-nucleus, respectively; notice the excluded indices,  $i = j$ , since an electron does not repel itself and we divide the summation by two to avoid double counting. Eqn 2.4 is the many-body Schrödinger equation<sup>12</sup>. Excluding the time dependence, the interaction with external electromagnetic fields as well as relativistic corrections eqn 2.4 represents almost everything we need to know about the behavior of materials. At this point, should we be to solve eqn 2.4 and find the ground-state of the system (lowest energy), we would be able to infer elastic, thermal and electronic properties of materials. However, solving this equation is no easy task, and most of the times it is practically impossible which is why we make some approximations to it.

In addition to the approximations done to solve eqn 2.4, we also like to express it in a more readable way. The values of  $\hbar$ ,  $m_e$ ,  $e$ , and  $\epsilon_0$  are fundamental constants and do not depend on the particular material under analysis. Using a semi-classical argument we set the value of the electron charge,  $e = 1$  and we define the Hartree energy as the Coulomb energy between an electron and a proton:

$$E_{Ha} = \frac{e^2}{4\pi\epsilon_0 a_0} \quad (2.5)$$

where  $a_0$  is the Bohr radius. Then, we can find that the typical size of the potential energies in eqn 2.4 is of the order of  $E_{Ha}$ . In the same way, we can get to the conclusion that the kinetic energy of eqn 2.4 is also of the order of  $E_{Ha}$ . Therefore, by measuring energies in units of  $E_{Ha}$  we can simplify Schrödinger equation to:

$$\left[ -\sum_i \frac{\nabla_i^2}{2} - \sum_I \frac{\nabla_I^2}{2M_I} + \frac{1}{2} \sum_{i \neq j} \frac{1}{|\mathbf{r}_i - \mathbf{r}_j|} + \frac{1}{2} \sum_{I \neq J} \frac{Z_I Z_J}{|\mathbf{R}_I - \mathbf{R}_J|} - \sum_{i,I} \frac{Z_I}{|\mathbf{r}_i - \mathbf{R}_I|} \right] \Psi = E_{TOT} \Psi \quad (2.6)$$

with the Hartree atomic units:

$$1Ha = 27.2114 eV = 4.3597 \cdot 10^{-18} J$$

$$1 bohr = 0.529177 \text{Å}$$

$$1 a.u.ofmass = 9.109383 \cdot 10^{-31} kg$$

Other approximations now applied to eqn 2.6 include the clamped nuclei approximation, in which the nucleus is thought to be so heavy compared to electrons,  $M_I \rightarrow \infty$ , that we can neglect its kinetic energy and the Coulomb interaction between nuclei, thus  $V_{n-n}$  is simply a constant. We can then rewrite eqn 2.6 as:

$$\left[ -\sum_i \frac{\nabla_i^2}{2} + \sum_i V_n(\mathbf{r}_i) + \frac{1}{2} \sum_{i \neq j} \frac{1}{|\mathbf{r}_i - \mathbf{r}_j|} \right] \Psi = E \Psi,$$

$$V_n(\mathbf{r}) = -\sum_I \frac{Z_I}{|\mathbf{r}_i - \mathbf{R}_I|} \quad (2.7)$$

### 2.1.1 Hartree-Fock equations

Eqn 2.7 is now a much simpler equation to deal with, however, the last term on the left hand side still represents a problem. What if we could ignore the electron-electron interaction but still account for the Coulomb repulsion in some form? Such a thing is obtained when we consider the independent electron and mean field approximations; we could write the many-body wavefunctions as a Slater determinant and obtain the single-particle wavefunctions as solutions of the simpler single-particle Schrödinger equation. In the same way, if we go back to classical electrostatics for a moment, we remember that a distribution of charge,  $n(r)$ , will generate an electrostatic potential of the Poisson's form which we call the Hartree potential:

$$\nabla^2 V_H(\mathbf{r}) = -4\pi n(\mathbf{r}) \quad (2.8)$$

Since every *independent* electron in the system experiences this average potential, we can write the Schrödinger equation as:

$$\left[ \frac{-\nabla^2}{2} + V_n(\mathbf{r}) + V_H(\mathbf{r}) \right] \phi_i(\mathbf{r}) = \epsilon_i \phi_i(\mathbf{r}) \quad (2.9)$$

where,  $\phi_i(r)$ , are the wavefunctions for each single electron. This method is better explained by Hartree<sup>13 14 15</sup>. Now, if we minimize the energy,  $E$ , with respect to the variations of the wavefunctions  $\phi_i(r)$  we introduce the non-local potential,  $V_X(r, r')$ , that arises mainly from Pauli's exclusion principle, and we obtain the Hartree-Fock equations:

$$\left[ \frac{-\nabla^2}{2} + V_n(\mathbf{r}) + V_H(\mathbf{r}) \right] \phi_i(\mathbf{r}) + \int d\mathbf{r}' V_X(\mathbf{r}, \mathbf{r}') \phi_i(\mathbf{r}') = \epsilon_i \phi_i(\mathbf{r}), \quad (2.10)$$

$$n(\mathbf{r}) = \sum_i |\phi_i(\mathbf{r})|^2, \quad (2.11)$$

$$\nabla^2 V_H(r) = -4\pi n(\mathbf{r}) \quad (2.12)$$

with:

$$V_X(\mathbf{r}, \mathbf{r}') = - \sum_j \frac{\phi_j^*(\mathbf{r}') \phi_j(\mathbf{r})}{|\mathbf{r} - \mathbf{r}'|} \quad (2.13)$$

where the sum covers all the occupied single-particle states. The function  $V_X$  is also called the Fock exchange potential<sup>12</sup>. It is important to remember that the potentials,  $V_H$  and  $V_X$ , come from the result of eliminating the electron-electron potential,  $V_{e-e}$ , in eqn 2.7. However, the description of the electrons is not complete, it is intuitive to think that the probability of finding an electron somewhere decreases if there is another electron nearby, we describe this repulsion yet with another potential,  $V_c(r)$ , where 'c' stands for correlation. And so the single-particle Schrödinger equation reads:

$$\left[ \frac{-\nabla^2}{2} + V_n(\mathbf{r}) + V_H(\mathbf{r}) + V_X(\mathbf{r}) + V_c(\mathbf{r}) \right] \phi_i(\mathbf{r}) = \epsilon_i \phi_i(\mathbf{r}) \quad (2.14)$$

## 2.2 Density Functional Theory

Now that we have reduced the complexity of the Schrödinger equation, that is, transforming from 3N-dimensional many-body equation into 3-dimensional N equations, we are ready to analyze the total energy of the system.

### 2.2.1 Hohenberg-Khon theorem

Remembering the Hamiltonian of eqn 2.7:

$$\hat{H}(r_1, r_2, \dots, r_N) = - \sum_i \frac{\nabla_i^2}{2} + \sum_i V_n(\mathbf{r}_i) + \frac{1}{2} \sum_{i \neq j} \frac{1}{|\mathbf{r}_i - \mathbf{r}_j|} \quad (2.15)$$

we notice that the structure of  $\hat{H}$  does not depend on the material under consideration, i.e. any variation of the energy,  $E$ , of the system is associated with variations in the many-body wavefunction, mathematically:

$$E = F[\Psi] \quad (2.16)$$

Hohenberg and Khon developed this statement<sup>16</sup> and concluded that:

1. The ground-state electron density,  $n_0(r)$ , of a system of interacting electrons determines uniquely the external potential  $V(r)$  in which the electrons move, and therefore the Hamiltonian and all physical properties of the system.
2. The ground-state energy  $E_0$  can be written as a functional of ground-state electron density

$$E_0 = F[n_0] \quad (2.17)$$

3. There exists a functional  $F[n]$  such that

$$F[n] = \int d\mathbf{r} n(\mathbf{r}) V_n(\mathbf{r}) + \langle \Psi | \hat{T} + \hat{W} | \Psi \rangle; \quad (2.18)$$

$$\hat{T} = - \sum_i \frac{1}{2} \nabla_i^2, \quad \hat{W} = \frac{1}{2} \sum_{i \neq j} \frac{1}{|\mathbf{r}_i - \mathbf{r}_j|}$$

### 2.2.2 Kohn-Sham equations

As we saw in the previous section, Hohenberg and Khon tell us that the ground-state energy  $E_0$  can be written as a functional of ground-state electron density. Nonetheless, this theorem does not mention how to construct such functional. It was Khon and Sham's idea<sup>17</sup> to split the second term in eqn 2.18 into the kinetic and Coulomb energy of independent electrons plus an extra term accounting for the exchange and correlation energy,  $E_{xc}$ :

$$E = F[n] = \int d\mathbf{r} n(\mathbf{r}) V_n(\mathbf{r}) - \sum_i \int d\mathbf{r} \phi_i^*(\mathbf{r}) \frac{\nabla^2}{2} \phi_i(\mathbf{r}) + \frac{1}{2} \iint d\mathbf{r} d\mathbf{r}' \frac{n(\mathbf{r}) n(\mathbf{r}')}{|\mathbf{r} - \mathbf{r}'|} + E_{xc}[n] \quad (2.19)$$

Now the construction of an entire functional  $F[n]$  has been reduced to a much simpler functional,  $E_{xc}[n]$ , the exchange and correlation contribution. If we knew this, then calculating the ground-state energy based on electron density would be straightforward. The main problem now remains with how we determine the electron density. It turns out that the function that minimizes the total energy,  $E = F[n]$ , is actually the ground-state density,  $n_0$ . This interesting fact is referred to as the "Hohenberg-Kohn variational principle"<sup>16</sup>.

$$\left. \frac{\delta F[n]}{\delta n} \right|_{n_0} = 0 \quad (2.20)$$

After solving eqn 2.20 and requiring the wavefunctions to be orthonormal we get to an equation very similar to eqn 2.14:

$$\left[ -\frac{\nabla^2}{2} + V_n(\mathbf{r}) + V_H(\mathbf{r}) + V_{xc}(\mathbf{r}) \right] \phi_i(\mathbf{r}) = \epsilon_i \phi_i(\mathbf{r}) \quad (2.21)$$

with the kinetic, nuclear, and Hartree potentials  $-\frac{\nabla^2}{2}$ ,  $V_n$ ,  $V_H$  plus an extra term  $V_{xc}$  which is called the energy and correlation potential, given by:

$$V_{xc}(\mathbf{r}) = \left. \frac{\delta E_{xc}[n]}{\delta n} \right|_{n(\mathbf{r})} \quad (2.22)$$

The set of equations resulting from eqn 2.21 are the Kohn-Sham equations and by solving them we can find many materials' properties. Nonetheless, since there isn't until now a known functional that perfectly satisfies eqn 2.21, we instead construct a range of functionals that approximate the exchange-correlation term as we will see in the next section.

### 2.2.3 DFT Functionals

In practice, the Kohn-Sham theory is used to set up the ground-state electron density of interacting electrons in the presence of a static potential from density functions. Nevertheless, constructing an accurate exchange-correlation functional,  $E_{xc}[n]$  demands great effort<sup>18</sup>. Such functionals are divided into their accuracy and the computational cost they demand. This hierarchy of electronic structure approaches is known as Jacob's ladder<sup>19</sup>, see Table 2.1.

The bottom or first rung is made up of local (spin) density approximation or LDA (LSDA) functionals, these assume a homogeneous distribution of electrons throughout the material, i.e. they best apply to metal-like materials, those with available energy states at the Fermi level. Examples of LDA functionals include VWN<sup>20</sup>, PZ81<sup>21</sup>.

Table 2.1: Jacob’s ladder of DFT functionals adapted from Mancuso et al<sup>2</sup>. As accuracy increases so does the computational cost. In this table, the computational cost increases from bottom to top. Some common functionals are also listed.

Chemical Accuracy	Functionals
Beyond DFT	
Double Hybrid	B2K-PLYP, wB97X-2
Hybrid	HSE06, B3LYP
Meta-GGA	M06-L, TPSS
GGA	PW91, PBE
LDA	VWN, PZ81
Hartree Fock	

The next rung in Jacob’s ladder pertains to generalized gradient approximation functionals (GGA). Since these functionals consider the electron density as well as its gradient these apply to more complicated systems such as molecules, 2D materials, interfaces, MOFs, etc. Common GGA functionals include PBE<sup>22</sup> and PW91<sup>23</sup>. However, although GGA functionals have a better description of the electronic structure they still are not able to describe the electron exchange and correlation correctly. Since most MOFs are systems containing spin-polarized, metal-based nodes, it is mandatory to account for exchange and correlation corrections in their electronic structure. Which meta-GGA functionals do when including the first and second derivatives of the electron density (e.g. M06-L<sup>24</sup> and TPSS<sup>25</sup>).

### Restored-regularized strongly constrained and appropriately normed (r<sup>2</sup>SCAN)

For a meta-GGA functional to be accurate and physically meaningful, such that it is used to correctly describe a wide range of chemical and physical systems, it must satisfy all the 17 exact constraints known\*. SCAN is the first meta-GGA non-empirical semilocal functional to do so<sup>26</sup>. A semilocal approximation can be written as:

$$E_{xc}[n_{\uparrow}, n_{\downarrow}] = \int d\mathbf{r} n \epsilon_{xc}(n_{\uparrow}, n_{\downarrow}, \nabla n_{\uparrow}, \nabla n_{\downarrow}, \tau_{\uparrow}, \tau_{\downarrow}) \quad (2.23)$$

where the functional not only depends on spin density,  $n_{\uparrow}, n_{\downarrow}$ , but also on its gradient,  $\nabla n_{\uparrow}, \nabla n_{\downarrow}$ , as well as the kinetic energy density,  $\tau$ . The SCAN functional presented numerical difficulties, which is

\*Such constraints are listed in the supplementary material of the work of Sun et al.<sup>26</sup>



why it was later 'regularized' for better computational performance<sup>27</sup>. However, in doing this five of the exact conditions SCAN was designed to obey were broken. rSCAN also hinders the generation of pseudopotentials and thus loses accuracy in atomization energies resulting in MAE (mean absolute error) values greater than the original SCAN functional for a specific set of molecules<sup>28</sup>. Restored-regularized or  $r^2$ SCAN improves numerical efficiency and recovers exact constraint adherence as well as presenting convergence with fewer iterations than SCAN<sup>29</sup>. In this work, because we are working with highly porous systems we need to account for van der Waals (vdW) interaction.  $r^2$ SCAN is good for intermediate-range but it misses the long-range interaction which is why we use the  $r^2$ SCAN + rVV10 functional.

### **Revised non-local van der Waals density functional (rVV10)**

For structures such as molecules, COF, or MOFs, dispersion interactions such as vdW must be taken into account in DFT calculations. The VV10 functional developed by Vydrov and Voorhis<sup>30</sup> is a non-local van der Waals functional using only the electron density as input to describe the intra- and inter-molecular dispersion interaction. In this work, we use the revised form of the VV10 functional (rVV10) that allow us to work in a plane wave framework<sup>31</sup>. In the same way, It still maintains an accurate description of the structural properties of representative ionic, covalent, and metallic solids.

### **Heyd-Scuseria-Ernzerhof (HSE06)**

The next two rungs of Jacobs's ladder pertain to hybrid functionals. Hybrid functionals include a fraction of exact (Hartree-Fock) exchange mixed with more computationally efficient semi-local exchange-correlation functionals. The HSE functional can be also thought of as the addition of the PBE functional with 25% of HF exchange developed by Heyd, Scuseria and Ernzerhof when<sup>32</sup>. Upon addition of a screened potential, it becomes the HSE06. This functional already describes the long and range interactions, however, it is more computationally demanding. For this reason, it will be used in the final step to find the density of states and band gap (HOMO - LUMO) once we have found the most stable structure using the  $r^2$ SCAN + rVV10 functional.

## **2.3 Density Functional Theory and magnetic materials**

Magnetism is also an important property of materials that has a wide range of applications in various fields, including spintronics, data storage, energy conversion, as well as biomedical technologies. To dwell

on the theory of magnetism the reader can refer to Kittel or Blundell<sup>33 34</sup>. In this section, we will see how density functional theory includes magnetism to perform spin-DFT calculations.

### 2.3.1 The Dirac equation and Spin

Let us consider a single electron in an electromagnetic field. Electrodynamics tells us that the magnetic field,  $\mathbf{B}(\mathbf{r},t)$ , and electric field,  $\mathbf{E}(\mathbf{r},t)$  can be written in terms of a vector  $\mathbf{A}(\mathbf{r},t)$  and a scalar function,  $\varphi(\mathbf{r},t)$ :

$$\mathbf{B}(\mathbf{r},t) = \nabla \times \mathbf{A}(\mathbf{r},t), \quad \mathbf{E}(\mathbf{r},t) = -\nabla\varphi(\mathbf{r},t) - \frac{\partial\mathbf{A}(\mathbf{r},t)}{\partial t} \quad (2.24)$$

then, the Hamiltonian of an electron in an electromagnetic field can be expressed as:

$$\hat{H} = \frac{1}{2m_e}(\mathbf{p} + e\mathbf{A})^2 - e\varphi \quad (2.25)$$

The quantum generalization of eqn 2.25 is:

$$i\hbar \frac{\partial}{\partial t} \psi(\mathbf{r},t) = \left[ \frac{1}{2m_e}(\mathbf{p} + e\mathbf{A})^2 - e\varphi \right] \psi(\mathbf{r},t) \quad (2.26)$$

where  $\mathbf{p}$  is the quantum mechanical momentum operator and  $\psi(\mathbf{r},t)$  is the electron wavefunction. Equation 2.26 is the most general form of the time-dependent Schrödinger equation for an electron in an electromagnetic field. However, it is not invariant under the Lorentz transformation, that is, it doesn't obey Einstein's special relativity. In order to circumvent this problem, Dirac proposed a more general version of the Schrödinger equation satisfying two postulates<sup>35 36</sup>: i) by construction the Dirac equation obeys the principles of special relativity, and ii) at velocities,  $v \ll c$ , the Dirac equation reduces to eqn 2.26, then the Dirac equation is:

$$i\hbar \frac{\partial}{\partial t} \Psi(\mathbf{r},t) = \left[ c \boldsymbol{\alpha} \cdot (\mathbf{p} + e\mathbf{A}) - e\varphi + \beta m_e c^2 \right] \Psi(\mathbf{r},t) \quad (2.27)$$

where the wavefunction,  $\Psi$ , has now become a array of four functions:

$$\Psi(\mathbf{r},t) = \begin{bmatrix} \psi(\mathbf{r},t;1) \\ \psi(\mathbf{r},t;2) \\ \psi(\mathbf{r},t;3) \\ \psi(\mathbf{r},t;4) \end{bmatrix}, \quad \text{with} \quad \boldsymbol{\Psi}(\mathbf{r},t) = \begin{bmatrix} \psi(\mathbf{r},t;1) \\ \psi(\mathbf{r},t;2) \end{bmatrix} \quad \text{and} \quad \psi(\mathbf{r},t) = \begin{bmatrix} \psi(\mathbf{r},t;3) \\ \psi(\mathbf{r},t;4) \end{bmatrix}$$

In the same way,  $\boldsymbol{\alpha}$  and  $\beta$  are both  $4 \times 4$  matrices:

$$\alpha = \begin{pmatrix} \mathbf{0} & \sigma \\ \sigma & \mathbf{0} \end{pmatrix}, \quad \beta = \begin{pmatrix} \mathbf{1} & \mathbf{0} \\ \mathbf{0} & -\mathbf{1} \end{pmatrix}$$

where  $\mathbf{0}$  is a  $2 \times 2$  matrix of zeros and  $\mathbf{1}$  is the  $2 \times 2$  identity matrix. The quantity  $\sigma$  is also a  $2 \times 2$  matrix, called Pauli matrices, and are defined as follows:

$$\sigma_x = \begin{pmatrix} 0 & 1 \\ 1 & 0 \end{pmatrix}, \quad \sigma_y = \begin{pmatrix} 0 & -i \\ i & 0 \end{pmatrix}, \quad \sigma_z = \begin{pmatrix} 1 & 0 \\ 0 & -1 \end{pmatrix} \quad (2.28)$$

Considering only stationary solutions of eqn 2.27 after some algebra we get to the expression<sup>12</sup>:

$$\left[ \frac{1}{2m_e} (\mathbf{p} + e\mathbf{A})^2 - e\varphi + \frac{2\mu_B}{\hbar} \mathbf{S} \cdot \mathbf{B} \right] \Psi = E \Psi \quad (2.29)$$

This equation is the Pauli equation<sup>37</sup>. The most important message to take home is that the last term of the left side of eqn 2.29 is similar to the form of magnetic coupling, to which we can say the electron has an intrinsic degree of freedom somehow similar to an angular momentum.

### 2.3.2 Spin in Density Functional Theory

Similarly, as to Section 2.2, we can reach an equation of the form of eqn 2.21 with the inclusion of the spin with the idea of the Hohenberg-Kohn theorem and the variational principle. Since the Dirac equation (eqn 2.27) is a matrix differential equation written in the four components of the Dirac spinor, it is intuitive to think that the scalar electron density of standard DFT will be replaced by a four-component function in relativistic DFT. Rajagopal and Callaway proved that the total energy of a system of electrons in its ground-state is a unique functional of the 'relativistic 4-current  $J_\mu(\mathbf{r})$ ',<sup>38</sup>.  $J_\mu(\mathbf{r})$  encloses three quantities: the electron density,  $n(\mathbf{r})$ , the electron spin density,  $\mathbf{s}(\mathbf{r})$  and the electron current density. Spin-density functional theory only considers the electron density and spin density contribution of  $J_\mu(\mathbf{r})$ , i.e., the total energy of the system is now a functional of the electron and spin density:

$$E = G[n(\mathbf{r}), \mathbf{s}(\mathbf{r})] \quad (2.30)$$

we can write these two quantities in terms of a compact object called *density matrix* defined as:

$$n_{\alpha\beta}(\mathbf{r}) = \sum_i \phi_i^*(\mathbf{r}; \alpha) \phi_i(\mathbf{r}; \beta) \quad (2.31)$$

where  $\alpha$  and  $\beta$  are integers of value 1 or 2 to identify the spinor components. Then the functional of the density matrix representing the energy in the ground-state is:

$$E = G[n_{\alpha\beta}(\mathbf{r})] \quad (2.32)$$

Similarly as to standard DFT, we can apply the formalism of Kohn-Sham saying that the density matrix in its ground-state,  $n_{\alpha\beta}^0$ , minimized the functional,  $G$ :

$$\left. \frac{\delta G[n_{\alpha\beta}]}{\delta n_{\alpha\beta}} \right|_{n_{\alpha\beta}^0} = 0 \quad (2.33)$$

In the same way, if we require the spinors to be orthonormal we obtained a relation similar to eqn 2.21

$$\left[ -\frac{\nabla^2}{2} + V_n(\mathbf{r}) + V_H(\mathbf{r}) + V_{xc}(\mathbf{r}) + \mu_B \sigma \cdot \mathbf{B}_{xc}(\mathbf{r}) \right] \Psi_i(\mathbf{r}) = \epsilon_i \Psi_i(\mathbf{r}) \quad (2.34)$$

This expression represents the Kohn-Sham equations for spin-DFT. Here the exchange and correlation magnetic field,  $\mathbf{B}_{xc}(\mathbf{r})$ , is generated by the presence of each electron's magnetic field. This extra field tends to align the spin of the electrons and may give magnetic order to the system. As we will see later in Section 3, we have considered four types of spin alignment in our structure for spin-DFT calculations.

## 2.4 Computational methods

### 2.4.1 Plane Waves

The reliability of DFT calculations depends not only on the structure or the functionals chosen to include exchange-correlation activity but also on the basis set the wavefunction is decomposed on. In solids state physics, the most common basis set is plane waves, this is what we call the Bloch's theorem

$$\psi_{n\mathbf{k}}(\mathbf{r}) = e^{i\mathbf{k}\cdot\mathbf{r}} u_{n\mathbf{k}}(\mathbf{r}) \quad (2.35)$$

In VASP, the plane waves are used to represent the wavefunctions of the electrons in the crystal lattice. The electron density is then calculated by summing over the contributions of all occupied states. The plane wave basis set is constructed by selecting a maximum kinetic energy cutoff for the electrons. This cutoff determines the maximum energy that an electron can have in the system, and thus the maximum frequency of the plane waves. One of the advantages of using plane waves in DFT calculations is that they form a complete basis set. This means that any electron density can be represented as a linear combination of

plane waves. This completeness property ensures that the DFT calculations are accurate, as any deviation from the exact solution can be systematically reduced by increasing the size of the plane wave basis set.

### 2.4.2 Pseudopotentials

In electronic structure calculations, the solution of the Schrödinger equation is often limited by the computational cost of including all the atomic electrons in the calculations. However, for predicting material properties we do not necessarily have to account for the core electrons, only those on the outer part of the atom. The use of pseudopotentials can reduce this computational cost by treating the core electrons as an effective potential instead of explicitly including them in the calculations. This approach has the advantage of enabling larger systems to be modeled with less computational cost. The pseudopotential is typically constructed using the all-electron wavefunctions and the true atomic potential as a starting point. The process involves removing the core electrons from the wavefunctions and replacing the atomic potential with an effective potential that reproduces the valence electron wavefunctions. The resulting pseudopotential is then used to solve the Schrödinger equation with fewer electrons making the calculation faster.

### 2.4.3 Vienna ab initio Simulation Package (VASP)

The Vienna Ab initio Simulation Package (VASP) is a computer program based on the density functional theory for atomic scale materials modeling. VASP uses the projector-augmented wave (PAW) method to compute an approximate solution to the many-body Schrödinger equation. Furthermore, Green's functions methods (GW quasiparticles, and ACFDT-RPA) and many-body perturbation theory (2nd-order Møller-Plesset) are also available in VASP.

To determine the electronic ground-state, VASP makes use of efficient iterative matrix diagonalization techniques such as the residual minimization method with direct inversion of the iterative subspace (RMM-DIIS) or blocked Davidson algorithms. These are coupled with highly efficient Broyden and Pulay density mixing schemes to speed up the self-consistency cycle<sup>39</sup>.

### 2.4.4 Density functional tight binding (DFTB+)

Density Functional Tight Binding (DFTB+) is a computational software package based on the Density Functional Theory Tight Binding approach. It is designed to simulate the electronic structure of large systems such as molecules and materials, at a lower computational cost compared to standard density

functional theory calculations. In this work, it was used as a previous relaxation before VASP calculations to optimize computational resources.

### 2.4.5 Birch-Murnaghan equation of state

For electronic relaxation, it is desired to choose the volume that optimizes energy, to get such optimal volume we have employed the Birch-Murnaghan equation of state. The general form of the Birch-Murnaghan equation is<sup>40</sup>:

$$P(V) = \frac{3}{2}B_0 \left[ \left( \frac{V_0}{V} \right)^{7/3} - \left( \frac{V_0}{V} \right)^{5/3} \right] \left\{ 1 - \frac{3}{4}(B'_0 - 4) \left[ \left( \frac{V_0}{V} \right)^{2/3} - 1 \right] \right\} \quad (2.36)$$

where  $P(V)$  is the pressure as a function of volume  $V$ ,  $B_0$  is the bulk modulus at equilibrium  $V_0$ , and  $B'_0$  is the first derivative of the bulk modulus with respect to pressure. At zero temperature, the pressure may be written as a function depending only on volume,

$$P(V) = -\frac{dE(V)}{dV}, \quad (2.37)$$

$$E(V) = E_0 + \frac{9V_0B_0}{16} \left\{ \left[ \left( \frac{V_0}{V} \right)^{2/3} - 1 \right]^3 B'_0 + \left[ \left( \frac{V_0}{V} \right)^{2/3} - 1 \right]^2 \left[ 6 - 4 \left( \frac{V_0}{V} \right)^{2/3} \right] \right\}. \quad (2.38)$$

$$(2.39)$$

Now if use Murnaghan's equation of state to fit the theoretical electronic ground-state energy we could obtain thermodynamical quantities like the bulk modulus<sup>41</sup>, which is given as:

$$B_0 = V_0 \frac{\partial^2 E(V)}{\partial V^2} \quad (2.40)$$

Eqn 2.40 is used in this work to report Bulk modulus values and it is a good parameter to indicate the material's resistance when subject to pressure.

## 2.5 Density of States

An important feature, used to describe the electrical and optical properties of solids, of the electronic structure of materials is the density of electronic states as a function of the energy. The density of states,  $g(\epsilon)$ , for energies in the range  $[\epsilon, \epsilon + d\epsilon]$  is defined as the sum over every state labeled by  $n$  with energy  $\epsilon_n$  in the range  $[\epsilon, \epsilon + d\epsilon]$ , per volume  $V$  of the system:

$$g(\epsilon)d\epsilon = \frac{1}{V} \sum_{n, \epsilon_n \in [\epsilon, \epsilon+d\epsilon]} 1 \Rightarrow g(\epsilon) = \frac{1}{V} \sum_n \delta(\epsilon - \epsilon_n) \quad (2.41)$$

where the  $\delta$  function appears as a consequence of taking  $d\epsilon \rightarrow 0$ , centered at the value  $\epsilon_n$

### 2.5.1 Local Density of States

For systems where the electrons are localized, as a consequence of the structure of the material as in MOFs, an important concept is the “localized density of states” or “projected density of states” (PDOS). This concept makes it possible to resolve the total density into components related to specific local orbitals in the system (e.g. atomic orbitals). In such situations, suppose that the state  $|\psi_n\rangle$  can be expressed in the basis of the orthonormal localized orbitals  $|\phi_i\rangle$ :

$$|\psi_n\rangle = \sum_i c_i^{(n)} |\phi_i\rangle, \quad \langle \phi_j | \phi_i \rangle = \delta_{ij} \Rightarrow \langle \psi_n | \psi_n \rangle = \sum_i |c_i^{(n)}|^2 = 1 \quad (2.42)$$

From the definition of the density of states  $g(\epsilon)$  we get:

$$g(\epsilon) = \frac{1}{V} \sum_n \delta(\epsilon - \epsilon_n) \sum_i |c_i^{(n)}|^2 = \sum_i \left[ \frac{1}{V} \sum_n |c_i^{(n)}|^2 \delta(\epsilon - \epsilon_n) \right] = \sum_i g_i(\epsilon) \quad (2.43)$$

with the PDOS,  $g_i(\epsilon)$  corresponding to the orbital  $|\phi_i\rangle$ , defined as:

$$g_i(\epsilon) = \frac{1}{V} \sum_n |c_i^{(n)}|^2 \delta(\epsilon - \epsilon_n) \quad (2.44)$$

This quantity gives the density of states at the value  $\epsilon$  related to the specific orbital  $|\phi_i\rangle$  in the basis. Furthermore, if spin contribution is considered when calculating the DOS, we will have the spin project density of states. In this work, we report the atomic/orbital, spin-projected density of states (cf. Section A, B).

## Chapter 3

# Methodology

This chapter is dedicated to the methods used in this work to construct, compute and analyze the metal-organic framework units considered in this thesis as well as the detailed protocols we followed to study their electronic properties. Software implementation is also explained (input, output files libraries, and packages).

### 3.1 Construction of MOF

Construction of MOFs<sub>sym5</sub>-ABDC-X (M5-X for short), was done in Materials Studio software, and it's obtained by linking the organic unit, (E)-4,4'-(diazene-1,2-diyl)bis(2-methylbenzoic acid) (H<sub>2</sub>ABDC, cf. Fig 3.7 from ref<sup>1</sup>), and copper-based secondary building unit (SBU) Cu<sub>2</sub>(CO<sub>2</sub>)<sub>4</sub> as shown in Fig 3.1a). The organic linker uses two benzene rings as extending units which are connected by a nitrogen-nitrogen bond and have a carboxyl group at the other end, it is a ditopic linker with an offset in its geometry due to the N-N bond, contrary to BDC and BPDC which have been thoroughly reviewed by researchers<sup>3,42-44</sup>; as we'll see later, the effects of the ligand longitude are important for photocatalysis. Resuming the construction, one ligand is connected to each end of the copper-based SBU as shown in Figure 3.1b). We studied M5 with three different linker designs obtained by monosubstituting F, Cl, Br on ABDC. Figure 3.1a) shows the position of the substitution.

The resulting unit cell of M5-X has 140 atoms so we can imagine the VASP calculations are not for the common home PC. Instead, the supercomputer of Gdansk University was used for such calculations.



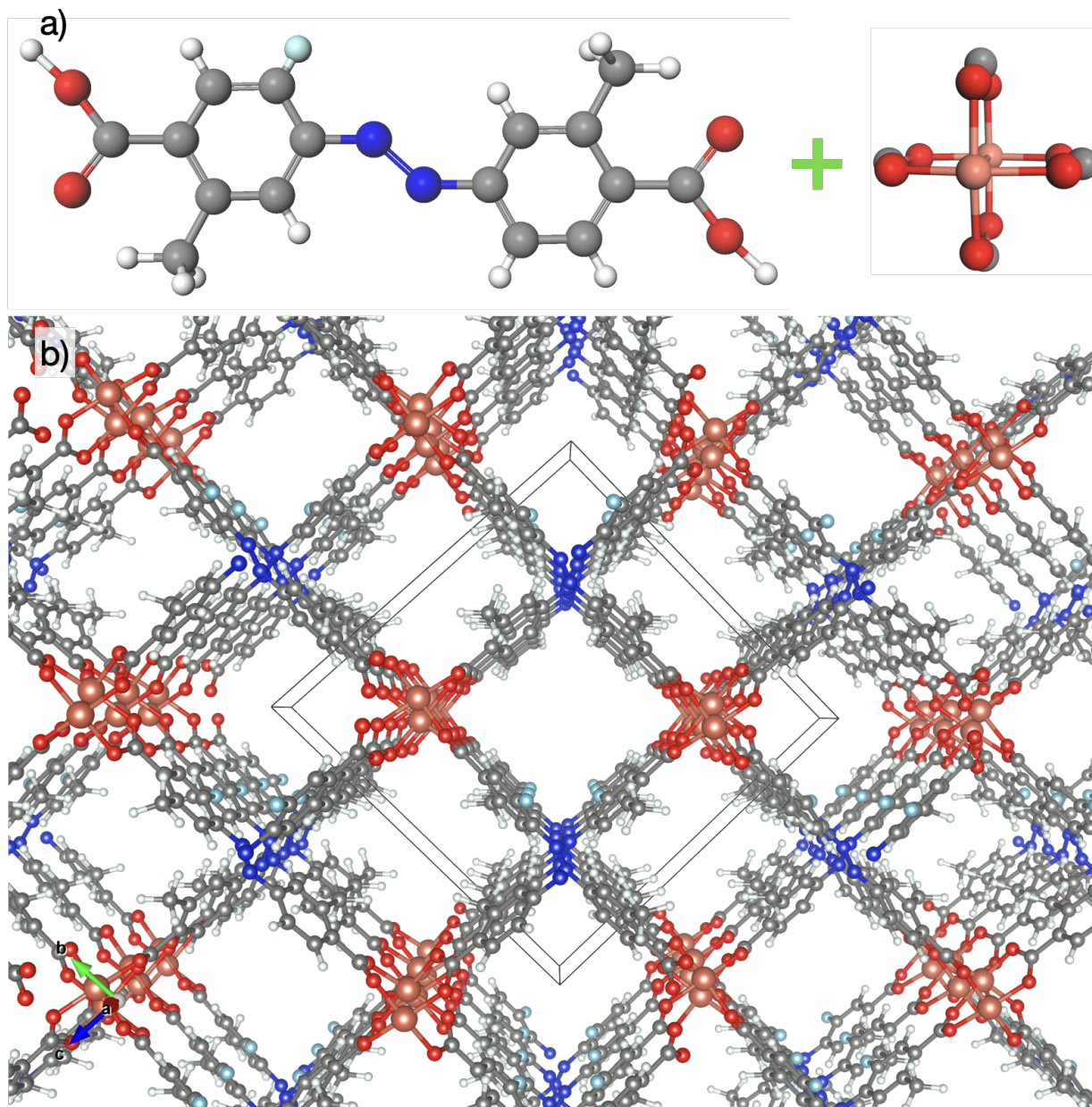


Figure 3.1: **a)** ditopic carboxylate linker functionalized by monosubstitution by  $X = \text{F}, \text{Cl}, \text{Br}$ , and a 4-connecting dinuclear paddle-wheel copper-based secondary building unit **b)** periodic representation of M5. Color code: gray, C; red, O; white, H; salmon, Cu; blue, N; light blue, substituent X.

### 3.1.1 Introducing magnetic order

Exchange interactions play a leading role in defining the bands as well as band edge positions which is why four possible magnetic arrangements were considered to perform spin-DFT calculations; these are displayed in Fig 3.2. Each copper atom has a magnetization of one Bohr magneton. It is important to note that the spin polarization is introduced once obtained the relaxed non-magnetic (NM) state. Then, we perform electronic relaxation again for the other magnetic states: ferromagnetic (FM), antiferromagnetic type A (AFM1), and antiferromagnetic type C (AFM2).

### 3.1.2 Introducing defects

When analyzing photocatalysis properties, it is essential that the band energies of the material under consideration straddle the redox potential of interest. That is, the energy of the conduction band minimum,  $E_{CBM}$ , lies higher in energy than the reaction-free energy corresponding to the reduction potential, and the  $E_{VBM}$ , lies lower in energy than the reaction-free energy corresponding to the oxidation potential<sup>10</sup>, this will be better explained in the following sections. To modify where the band edge position falls under certain material we can try different options such as functionalization with other molecules (e.g.  $\text{NH}_2$ ,  $\text{NO}_2$ ) instead of simple F, Cl, Br, double substitution as opposed to monosubstitution; or introducing defects into the structure. In this work, we tried the latter, and although there exist three types of MOF defects (vacancies, substitutions, interstitials<sup>1</sup>), we chose substitution as it is experimentally feasible by transmetalation. Thus, we tried replacing one copper atom on one node of the unit cell with zirconium or magnesium as seen in Fig 3.3.

## 3.2 Relaxation using DFTB+

As mentioned earlier, calculations with structures having two or more order of magnitudes of the number of atoms mean high computational cost. Inserting the constructed unit cell of M5 from Materials Studio straight to VASP calculations is a wrong move that could mean days of computational processing. This is why we have first relaxed the structure with the package DFTB+. DFTB+ is an implementation of the Density Functional based Tight Binding (DFTB) method that enables simulations of complex systems and long timescales with reasonable accuracy while being two orders of magnitudes faster than ab initio methods. In this way, we can start VASP calculations with a more reasonable structure physically and chemically speaking<sup>45</sup>.

## 3.3 VASP implementation

The Vienna package needs file input files to run an atomic simulation<sup>39</sup>: INCAR, KPOINTS, CONTCAR, POTCAR and the executable file (.sh format). The first thing done was a self-consistent field (SCF) iteration to find the plane wave cut-off energy and  $k$ -point sampling. We specify these values in the INCAR and KPOINTS files respectively. In addition, INCAR also contains tags for which the parameters are chosen to run simulations, here is specified the meta-GGA functional,  $r^2\text{SCAN}$ , plus the non-local electron density correction, rVV10. CONTCAR contains the atomic positions of the atoms of the unit cell. For the first

calculation, this file is taken from the results of DFTB+ relaxation, after so we only use CONTCAR files from VASP itself. POTCAR contains the pseudopotentials of the atoms described in the CONTCAR file given in the same order, these pseudopotentials are only obtained under VASP license. (more information on VASP files can be found on its website<sup>39</sup> )

Once electronic relaxation is obtained for a given material, hybrid functional, HSE06, is used for electronic properties due to its precision. We call this protocol  $r^2$ SCAN+rVV10//HSE06. It is important to notice that HSE06 is not used from the very beginning because of its high computational demand. For instance, calculations of full electronic relaxation with functionals  $r^2$ SCAN+rVV10 can take from 15-30 days with previous DFTB+ relaxation.

### 3.4 Band Alignment

A method developed by Butler et.al.<sup>46</sup> was used to determine the vacuum levels of porous M5 frameworks. Spherical electrostatic probes with radii of 1 – 5 Å located at the center of the large cubical cage ( $\approx 9$  Å) of each M5 framework were used to estimate the electrostatic reference potential (see Fig 3.4). For each case, only values for which the variance of the potential is less than  $10^{-5}$  V were regarded, indicating accurate results; at last, the mean of the electrostatic potential (EP) values was used for band alignment.

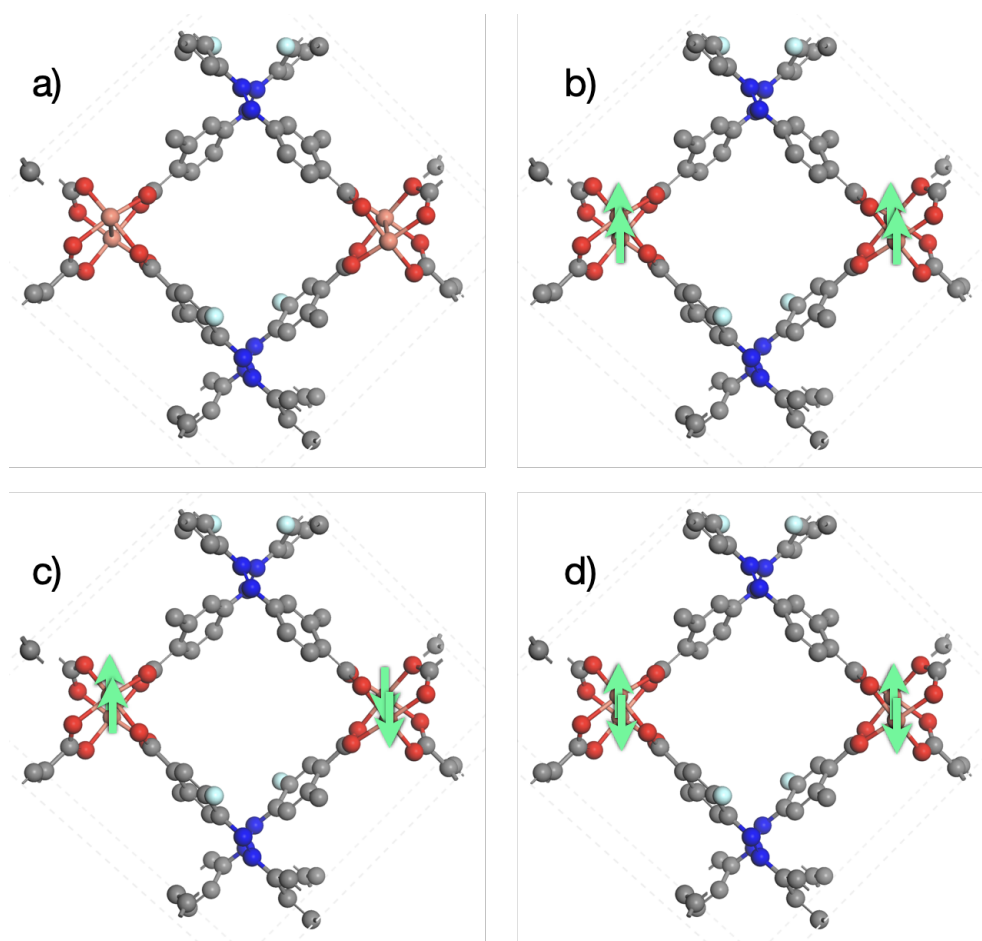


Figure 3.2: Unit cell of M5 displaying four different magnetic order: **a)** non-magnetic (NM), **b)** ferromagnetic (FM), **c)** antiferromagnetic type A (AFM1), **d)** antiferromagnetic type C (AFM2). Color code same as Fig 3.1. H atoms are omitted for simplicity.

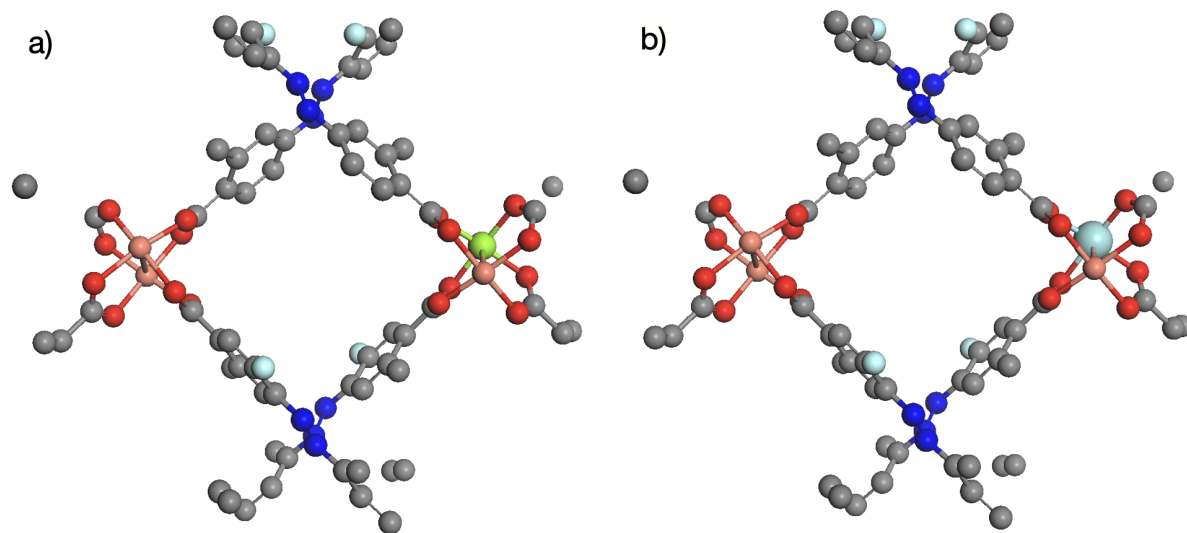


Figure 3.3: Unit cell of M5 with a different atom introduced to one SBU simulating defect: **a)** magnesium (green), **b)** zirconium (bigger light blue. Color code same as Fig 3.1. H atoms are omitted for simplicity)

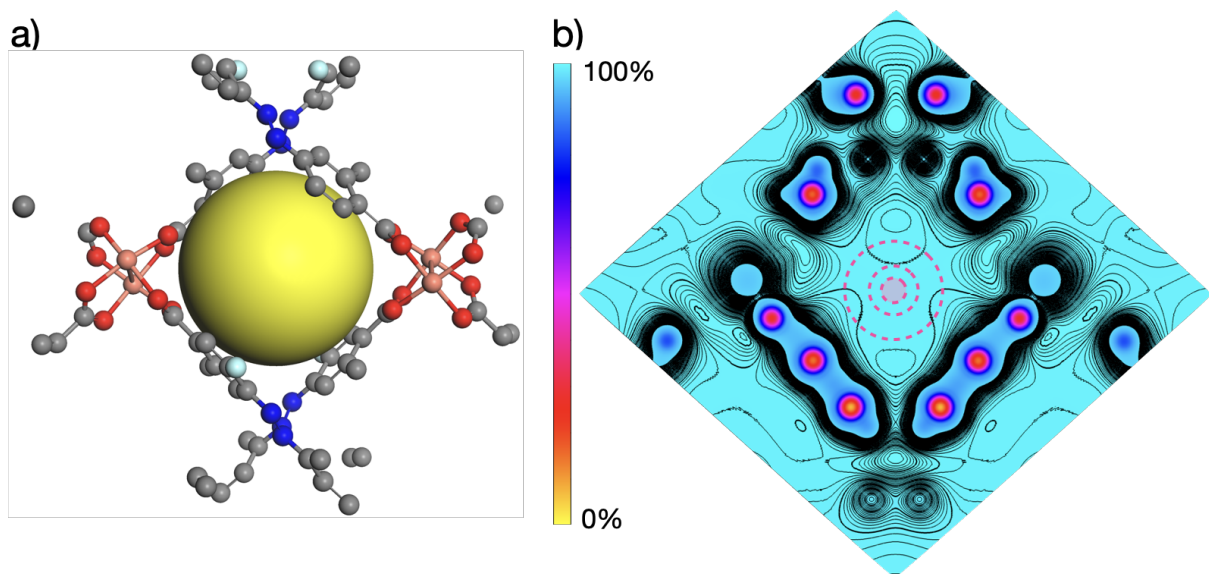


Figure 3.4: **a)** M5-F unit cell enclosing a 9 Å-radius yellow sphere representing the main pore. **b)** Contour map of electrostatic potential at the main pore. Dashed circles of radii = 1, 2, 4 Å are plotted to give an idea of the sampled area for vacuum level calculation. Color code same as Fig 3.1. H atoms are omitted for simplicity

## Chapter 4

# Results and Discussion

This section presents the results of the Spin-DFT  $r^2$ SCAN+rVV10 and HSE06 computed electronic properties for three different MOF structures named here as M5-F, M5-Cl, and M5-Br. Furthermore, nomenclature in plots is given by MOF name-SBU functionalization-magnetic states, i.e. M5-F-AFM1 refers to antiferromagnetic type A state MOF5 constructed with ABDC linker functionalized with F. In addition, plane-wave cut-off energy and  $k$ -points convergence will be checked for the corresponding non-magnetic structures only and then continue using the same values in the other cases. We have computed and studied the equation of state, the partial density of states, magnetic phase stability with respect to the non-magnetic phases, and band alignment with respect to the vacuum energy. Defects were only introduced to the AFM2 cases, which are predicted to be the most stable magnetic phase.

### 4.1 The M5-F

#### 4.1.1 Cut-off energy and k-Points

To start the calculations in VASP, the first step is to calculate the plane wave cutoff energy and  $k$ -points convergence. Fig 4.1 shows that in order to obtain convergence of energy difference to within 1 meV/atom, a plane wave cut-off energy of 850 eV or higher is needed. Then, we choose ENCUT = 850 eV (in the INCAR file) for faster performance. In the same way, The  $k$ -point mesh was sampled using a  $2 \times 1 \times 1$  MonkhorstPack grid (or  $\Delta k = 2\pi \cdot 0.05 \text{ \AA}^{-1}$ ) since it is inside the window of 1 meV/atom convergence.



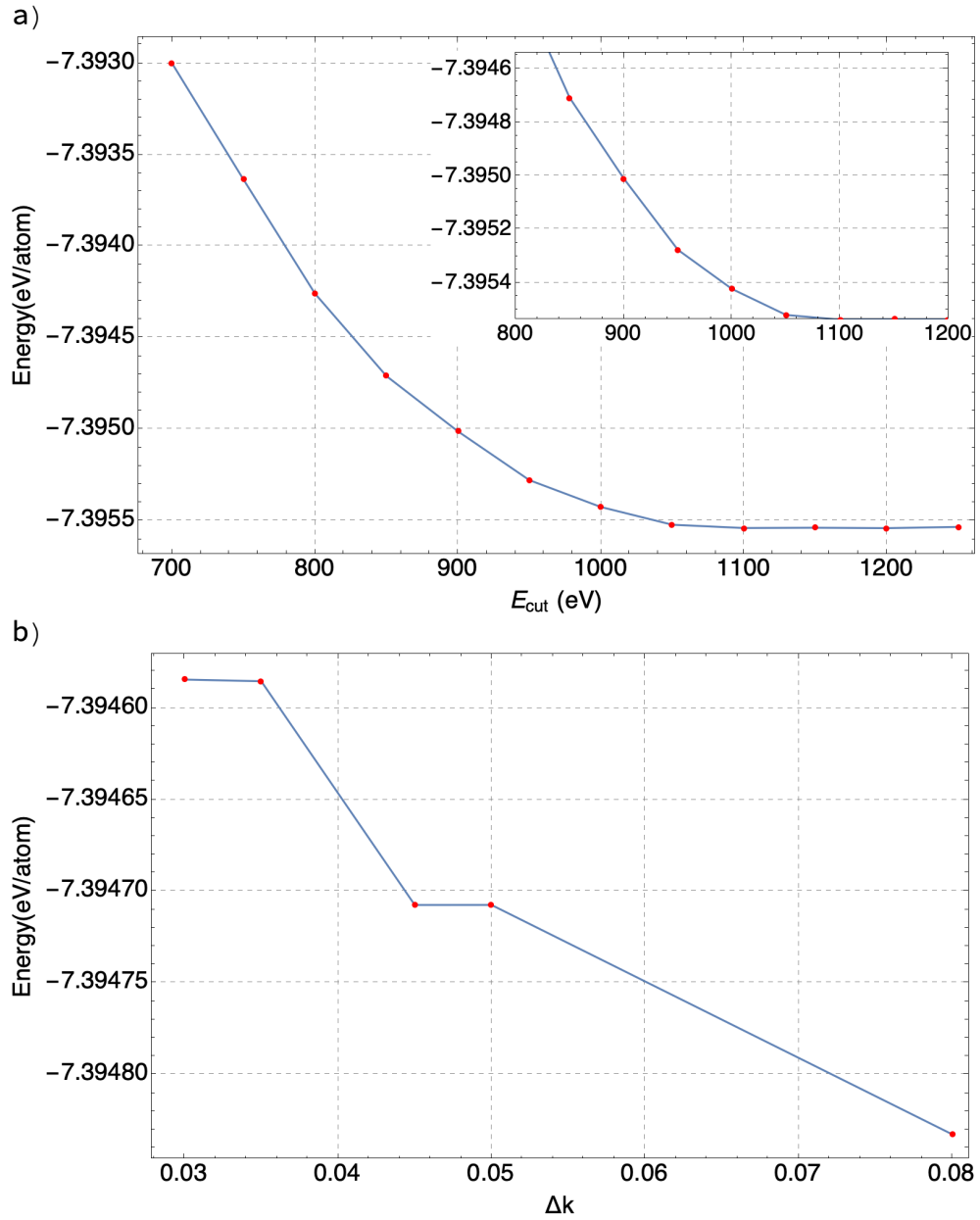


Figure 4.1: **a)** Plane wave cut-off energy convergence of M5-F. Inset displays a zoom of 1 meV/atom showing convergence starts at 850 eV. **b)** Energy convergence as a function of  $k$ -points in terms of  $\Delta k/2\pi$

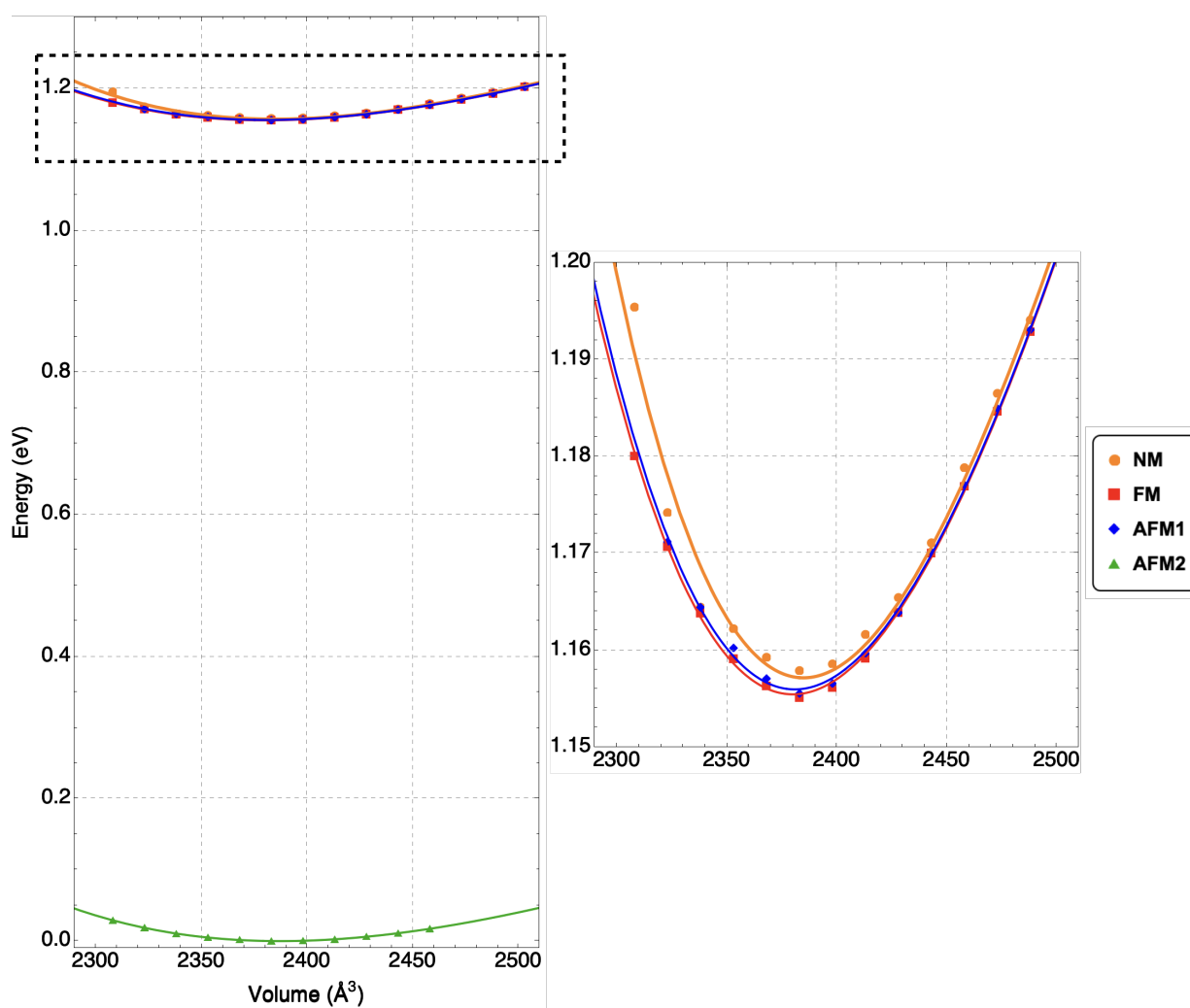


Figure 4.2: Birch-Murnaghan equation of states of M5-F fitted with data obtained by relaxation with functionals  $r^2$ SCAN+rVV10. To the right a zoom of the dashed-selected area.

Table 4.1: Computed  $r^2$ SCAN+rVV10 crystallographic data and properties of all four M5-F magnetic states: antiferromagnetic AFM, ferromagnetic FM and non-magnetic NM.  $a, b, c$  are the lattice parameters and the corresponding angles  $\alpha, \beta$  and  $\gamma$ . The optimal volume  $V$ , bulk modulus  $B_0$ . The relative energy  $\Delta E$  with respect to the most stable phase AFM2 and the absolute values of the local magnetic moment  $|m_{\text{Cu}}|$  at the Cu sites are computed from the  $r^2$ SCAN+rVV10//HSE06 results.

Property	Calculated ( $r^2$ SCAN+rVV10)			
	AFM1	AFM2	FM	NM
Space group	C121			
$a$ (Å)	8.88	8.86	8.83	8.86
$b = c$ (Å)	16.98	17.01	17.01	16.99
$\alpha$ (°)	83.58	83.98	83.75	83.89
$\beta = \gamma$ (°)	74.83	74.88	74.92	74.88
Volume (Å <sup>3</sup> )	2380.82	2387.21	2379.99	2383.45
$B_0$ (GPa)	3.16	3.05	3.14	3.56
$\Delta E$ (eV)	1.156	0.0	1.156	1.157
$ m_{\text{Cu}} $ ( $\mu_B$ )	0.65	0.66	0.66	0.0

### 4.1.2 Bulk Structure

Fig 4.2 shows the  $r^2$ SCAN+rVV10 computed Birch-Murnaghan equation of states (BM-EOS) of all four magnetic arrangements fitted with data obtained with VASP. The AFM2 state was found to be the most stable configuration. The energy difference between AFM2 and the other magnetic phases is  $\Delta E = 1.16$  eV. This difference in energy suggest that it is less demanding to arrange opposite spins in the same node contrary to AFM1 state where nodes as a whole have opposite spins or FM where all spins point in the same direction. Unit cell parameters and other crystallographic data for the four structures are given in table 4.1. Bulk modulus are between 3.0 – 3.6 GPa which is expected since we are dealing with porous structures (e.g. diamond, 440 GPa; silicon, 100Gpa<sup>33</sup>). In fact, others MOFs report values in the range 10 – 20 GPa, the smaller values reported here are due to the use of a longer organic linker (ABDC) which increases the porosity.

### 4.1.3 Density of States & Band Alignment

The partial density of states (PDOS) was computed with the hybrid functional HSE06 using the optimal structure obtained from  $r^2$ SCAN+rVV10, from now on we refer this calculations  $r^2$ SCAN+rVV10//HSE06. PDOS was obtained for each magnetic state, all of them show similar electronic properties but the non-magnetic case, which has smaller band gap and workfunction,  $E_g = 0.81$  eV and  $\Phi = 5.90$  eV. The band gap for the AFM1, AFM2 and FM states are  $E_g = 2.68, 2.73$  and  $2.61$  eV respectively. These values makes them a good candidate for photocatalysts since the visible light region of the solar spectra corresponds to energies of  $1.7 - 3.2$  eV. A desired characteristic of a good photocatalytic is a prolonged lifetime of the excited state, then the photogenerated electrons should present ligand-to-metal charge transfer (LMCT) to form charge separated states that prevent fast recombination of photogenerated charges. This is required for photocatalysis purposes since the promotion of long lifetime charge-separated states enables reduction/oxidation reactions to occur<sup>47</sup>. Considering the LMCT energy,  $E_{LMCT}$ ; an efficient LMCT should have a negative  $E_{LMCT}$  that is the energy change of the photogenerated electron from the photoexcited linker to the lowest unoccupied metal state. Spin projected PDOS is shown in Fig 4.3, here we can notice that AFM1, AFM2, FM states present  $E_{LMCT} = 0$  eV since the lowest unoccupied states are delocalized on the linker and metal states. It is also noted that the PDOS in the ferromagnetic state (FM) is not symmetric due to its intrinsic magnetic arrangement. On the other hand, NM state presents metal-to-metal excitation which is less favorable in photocatalysis.

Band energies are aligned to vacuum levels of each porous MOF according to Butler et.al.<sup>46</sup> which is explained in Section 3.4. MOF's vacuum level energies are taken at the center of the main pore. It is recommended that the selected area is a plateau in electrostatic potential (EP). This procedure is the same for all states, however, only the AFM2 state is depicted below since it is the most stable configuration. Figure 4.4 shows 2D perpendicular planes along the three lattice vectors showing the pore as well as the EP magnitude (color bar). Mean electrostatic potential for each spin arrangement values are reported in table 4.2. We can notice that although the EP magnitude goes from  $0 - 5.35$  eV throughout the material, the mean EP value for M5-F-AFM2 is  $4.04$  eV at the center of the pore. As we'll see later, these EP values are decreased for MOF-Cl, Br due to electronegativity.

Finally, in the AFM2 state, although the PDOS image shows LMCT, there might also exists linker localized excitations which may affect the photocatalysis process as well as the reduction yield (i.e. in the the case of  $CO_2$  reduction). For this reason, we have decided to introduce defects into MOF-F to see if its possible to shift the bands belonging to the linker and leave the SBU-bands only in the CBM (cf. Section

4.4).

Table 4.2: Mean electrostatic potential at pore for each M5-F magnetic state.

	AFM1	AFM2	FM	NM
Potential (eV)	4.08	4.04	4.06	4.04

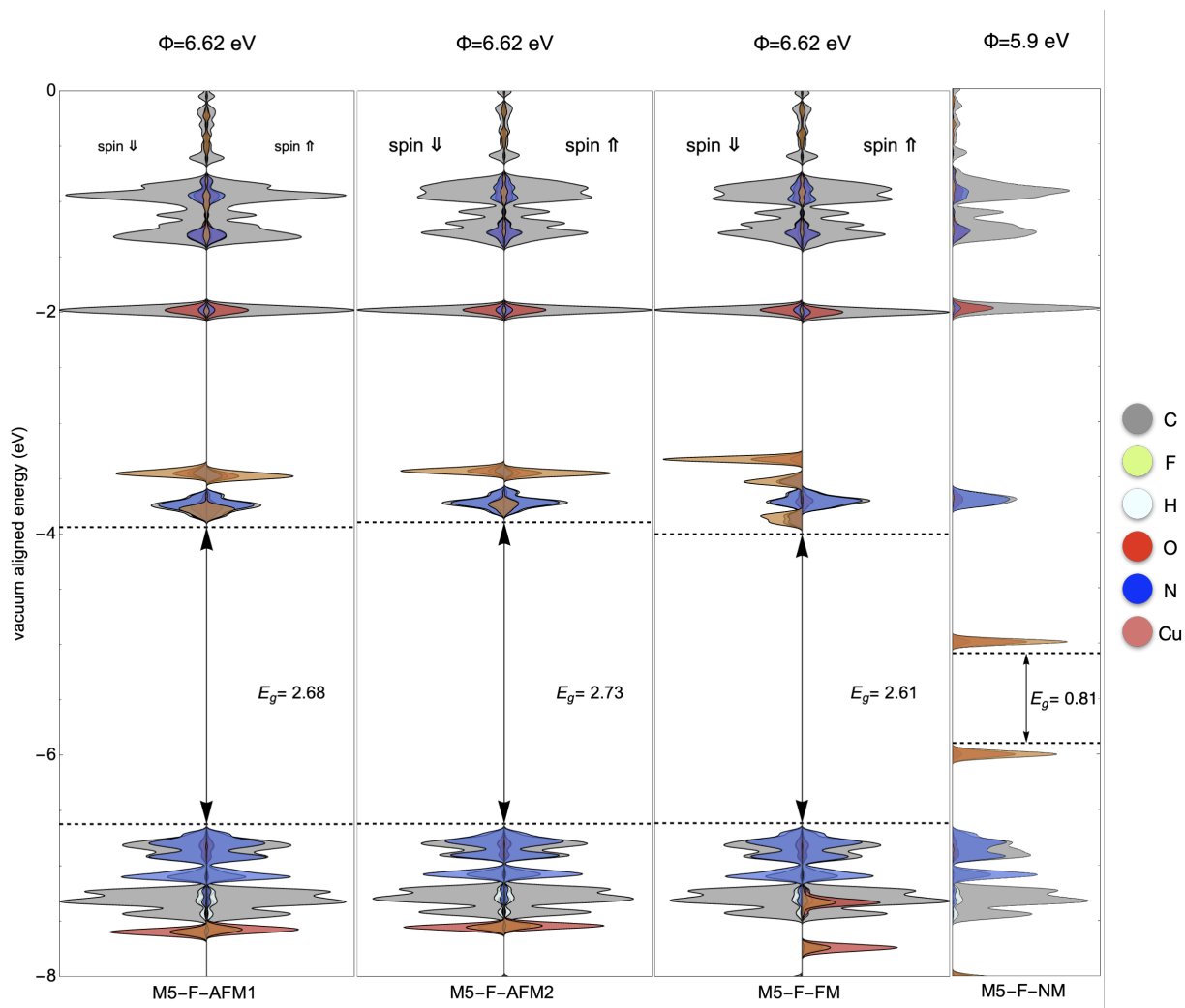


Figure 4.3: Spin-separated atomic pDOS ( $r^2$ SCAN+rVV10/HSE06) for all M5-F magnetic configurations. Band gap ( $E_g$ ) and band edge positions are aligned with their vacuum level according to table 4.2. Nomenclature is given by MOF name-SBU functionalization-Magnetic state (e.g. M5-F-NM). Workfunction is represented by the Greek letter  $\Phi$ .

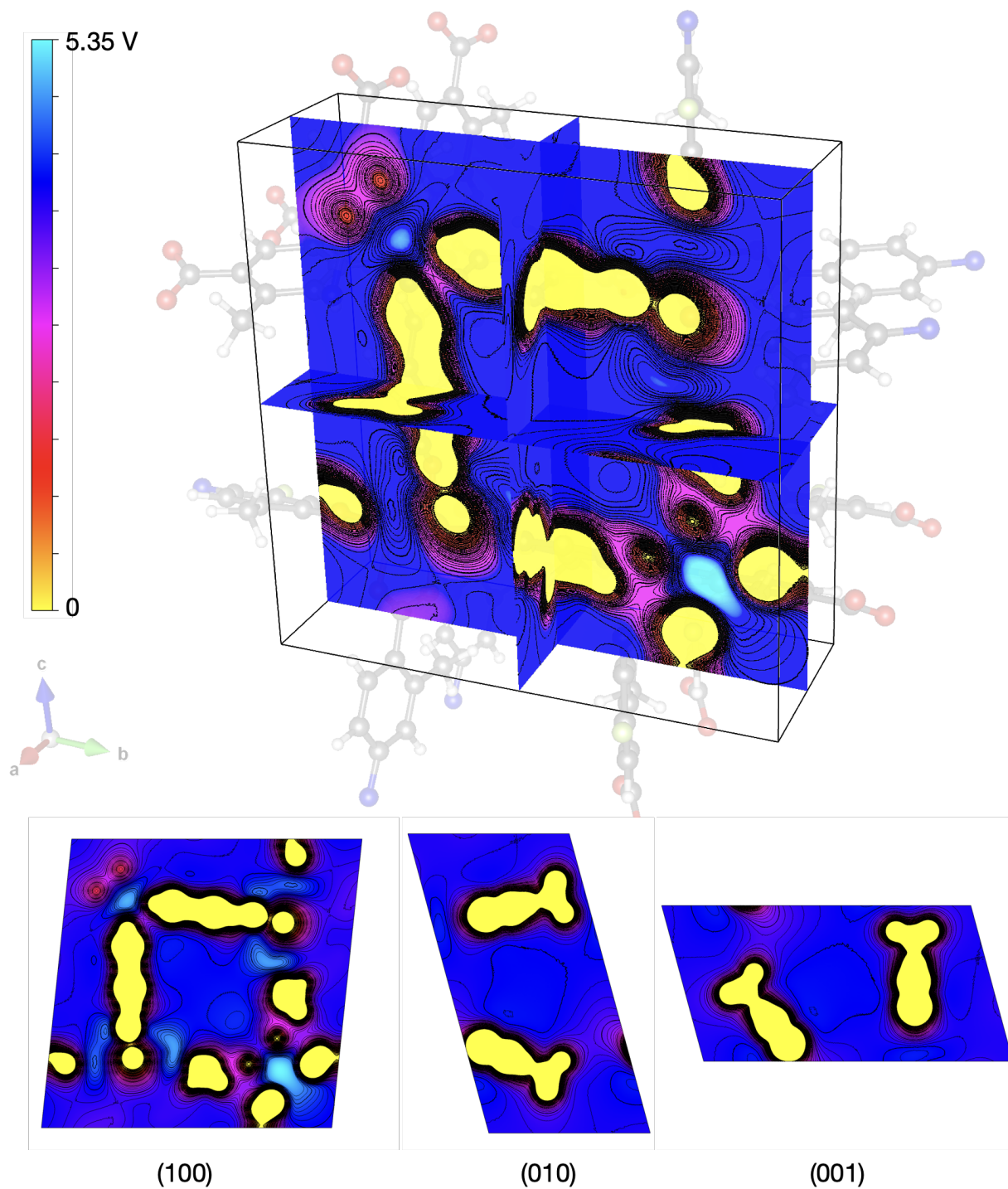


Figure 4.4: Contour plot of 2D sections at half the distance of the lattice vectors showing the electrostatic potential of M5-F-AFM2. The intersection of the three planes is taken as the center of the pore. In the bottom, each 2D plane with their corresponding Miller indices. Color code same as Fig 4.3.

Table 4.3: Computed  $r^2$ SCAN+rVV10 crystallographic data and properties of all four M5-Cl magnetic states: antiferromagnetic AFM, ferromagnetic FM and non-magnetic NM.  $a, b, c$  are the lattice parameters and the corresponding angles  $\alpha, \beta$  and  $\gamma$ . The optimal volume  $V$ , bulk modulus  $B_0$ . The relative energy  $\Delta E$  with respect to the most stable phase AFM2 and the absolute values of the local magnetic moment  $|m_{\text{Cu}}|$  at the Cu sites are computed from the  $r^2$ SCAN+rVV10/HSE06 results.

Property	Calculated ( $r^2$ SCAN+rVV10)			
	AFM1	AFM2	FM	NM
Space group	C121			
$a$ (Å)	8.86	9.49	9.47	9.47
$b = c$	17.02	17.02	17.02	16.99
$\alpha$ (°)	82.94	80.85	81.55	80.44
$\beta = \gamma$ (°)	74.75	73.55	73.61	73.56
Volume (Å <sup>3</sup> )	2387.37	2518.89	2520.38	2504.62
$B_0$ (GPa)	2.85	4.10	4.08	3.61
$\Delta E$ (eV)	4.80	0.0	0.10	1.16
$ m_{\text{Cu}} $ ( $\mu_B$ )	0.66	0.66	0.66	0.0

## 4.2 M5-Cl

### 4.2.1 Bulk Structure

Fig 4.5 shows the  $r^2$ SCAN+rVV10 computed Birch-Murnaghan equation of states (BM-EOS) of all four magnetic arrangements of M5-Cl. In this case, the AFM2 state was also found to be the most stable configuration, however, the FM state have similar energy stability ( $\Delta E = 0.10$  eV). The energy differences between AFM2 and NM, AFM1 states are  $\Delta E = 1.16$  and  $4.80$  eV, respectively. This latter difference in energy suggest that it is less demanding to arrange opposite spins in the same node contrary to AFM1 state where nodes as a whole have opposite spins. Unit cell parameters and other crystallographic data for the four structures are given in table 4.3. The bulk modulus for the FM state is lower following the statement that the FM state is the less stable configuration. For the other states, we noticed an increase of unit cell volume due to Cl monosubstitution. Bulk modulus values stays in the range  $< 4$  Gpa.



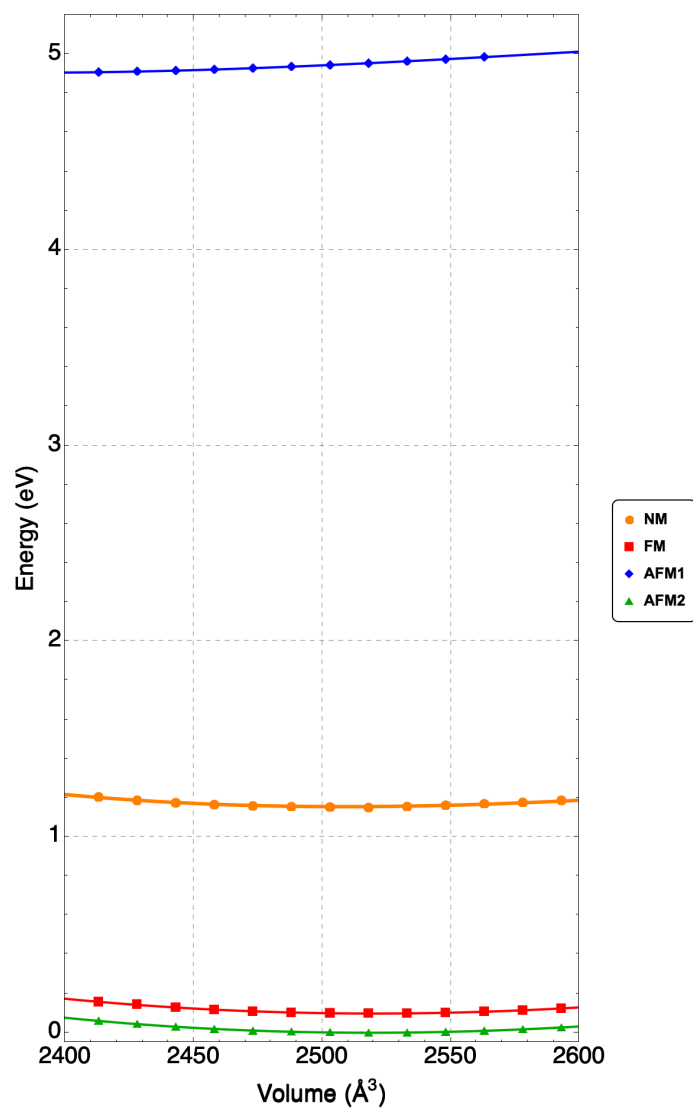


Figure 4.5: Birch-Murnaghan equation of states of M5-Cl fitted with data obtained by relaxation with functionals  $r^2$ SCAN+rVV10.

### 4.2.2 Density of States & Band Alignment

The partial density of states (PDOS) was computed with the hybrid functional HSE06. PDOS was obtained for each magnetic states, all of them show similar electronic properties but the non-magnetic case, which has smaller values for band gap and workfunction,  $E_g = 0.81$  eV and  $\Phi = 5.89$  eV. The band gap for the AFM1, AFM2 and FM states are  $E_g = 2.61, 2.70$  and  $2.61$  eV respectively showing reduced values compared to the MOF-F structures. Nonetheless, the values for the workfunction remain almost identical. PDOS is shown in Fig 4.6. Here we can see that the three magnetic states also present  $E_{LMCT}$ . As in the case of M5-F, NM state only presents metal-to-metal excitation. Similar to MOF-F, we encourage to introduce and study defects into MOF-Cl for isolation of SBU-states in the conduction band minimum\*.

Band energies are aligned to vacuum levels of each porous MOF according to Butler et. al.<sup>46</sup> which is explained in Section 3.4. MOF's vacuum level energies are taken at the center of the main pore. Figure 4.7 shows 2D perpendicular planes along the three lattice vectors showing the pore as well as contour map for the electrostatic potential. This procedure is repeated for each spin arrangement and values are reported in table 4.4. MOF-Cl vacuum energy levels showed reduction compared to MOF-F, in accordance to what one would expect since chloride is less electronegative than fluoride.

Table 4.4: Mean electrostatic potential at pore for each M5-Cl magnetic state.

	AFM1	AFM2	FM	NM
Potential (eV)	4.05	3.99	3.98	4.00

---

\*The reason for not including these effects in this work is related to computational time issues.

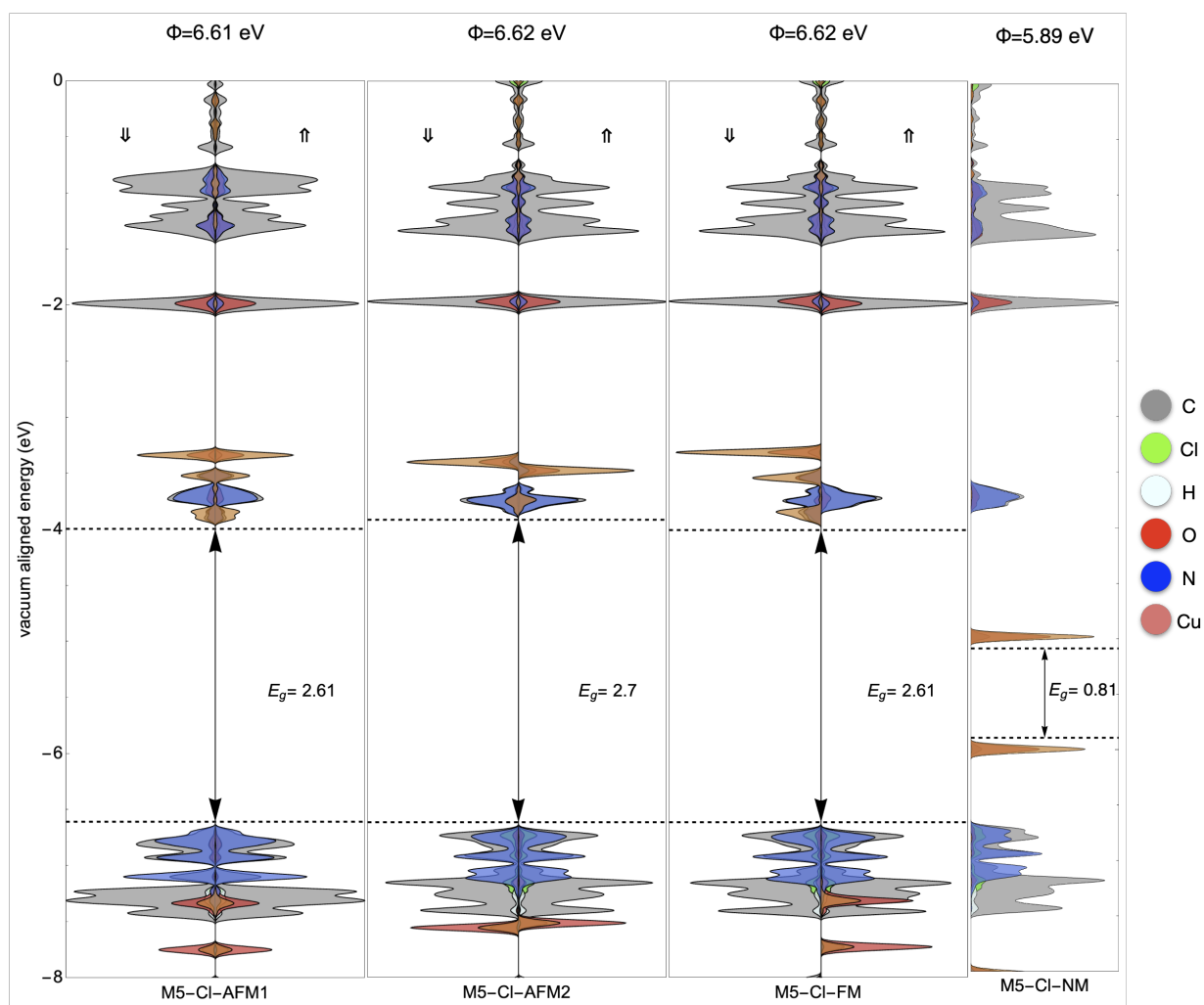


Figure 4.6: Spin-separated atomic pDOS (r<sup>2</sup>SCAN+rVV10//HSE06) for all MOF-Cl magnetic configurations. Band gap ( $E_g$ ) and band edge positions are aligned with their vacuum level according to table 4.4. Nomenclature is given by MOF name-SBU functionalization-Magnetic state (e.g. M5-Cl-NM). Workfunction is represented by the greek letter  $\Phi$ .

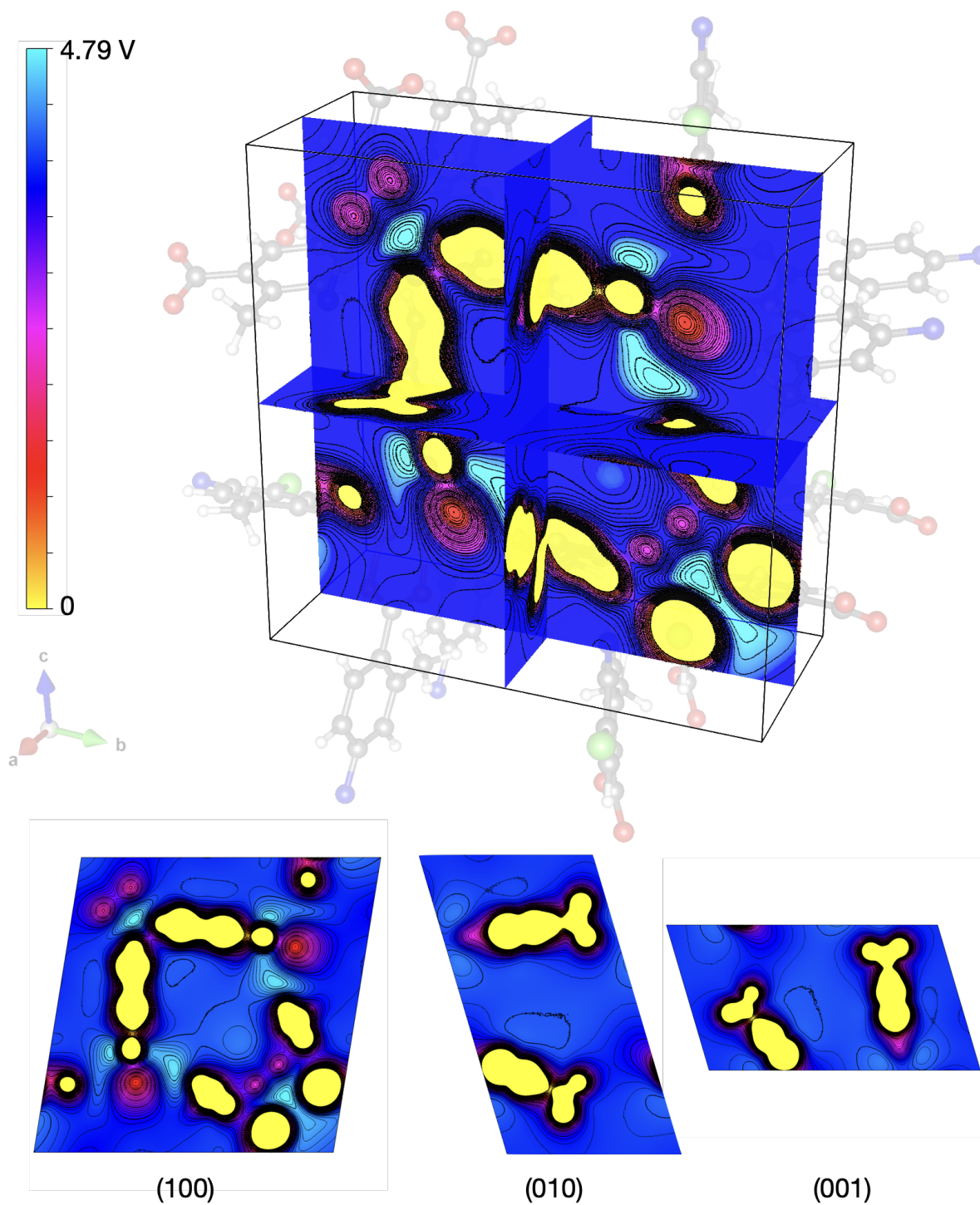


Figure 4.7: Contour plot of 2D sections at half the distance of the lattice vectors showing the electrostatic potential of M5-Cl-AFM2. The intersection of the three planes is taken as the center of the pore. In the bottom, each 2D plane with the corresponding Miller indices. Color code same as Fig 4.6.

## 4.3 M5-Br

### 4.3.1 Bulk Structure

Electronic relaxation with functionals  $r^2$ SCAN+rVV10 yielded the optimal structure. Fig 4.8 shows the Birch-Murnaghan equation of states (BM-EOS) of all four magnetic arrangements of M5-Br fitted with VASP data. As in previous cases, the AFM2 state was also found to be the most stable configuration for MOF-Br. Nonetheless, the AFM1 state is equally stable ( $\Delta E = 0.00$ ), certainly not following the trend of MOF-F, Cl in which the AFM1 state was the less stable state. We believe this stability issue is related to more Br-bands located in the valence band contrary to MOF-F, Cl-AFM1. Furthermore, volume and bulk modulus between AFM1 and AFM2 states are quite similar (tab 4.6).

In addition, the FM state has similar energy stability too,  $\Delta E = 0.10$  leaving the NM states as the only unstable configuration,  $\Delta E = 1.16$ . Unit cell parameters and other crystallographic data for the four structures are given in table 4.5.

Table 4.5: Computed  $r^2$ SCAN+rVV10 crystallographic data and properties of all four M5-Br magnetic states: antiferromagnetic AFM, ferromagnetic FM and non-magnetic NM.  $a, b, c$  are the lattice parameters and the corresponding angles  $\alpha, \beta$  and  $\gamma$ . The optimal volume  $V$ , bulk modulus  $B_0$ . The relative energy  $\Delta E$  with respect to the most stable phase AFM2 and the absolute values of the local magnetic moment  $|m_{\text{Cu}}|$  at the Cu sites are computed from the  $r^2$ SCAN+rVV10//HSE06 results.

Property	Calculated ( $r^2$ SCAN+rVV10)			
	AFM1	AFM2	FM	NM
Space group	C121			
$a$ (Å)	9.73	9.74	9.73	9.71
$b = c$	17.02	17.00	17.03	16.99
$\alpha$ (°)	81.45	81.34	81.41	81.58
$\beta = \gamma$ (°)	73.12	73.14	73.09	73.15
Volume (Å <sup>3</sup> )	2573.62	2573.68	2577.68	2562.40
$B_0$ (GPa)	4.48	4.63	4.16	4.45
$\Delta E$ (eV)	0.0	0.0	0.10	1.16
$ m_{\text{Cu}} $ ( $\mu_B$ )	0.66	0.66	0.66	0.0

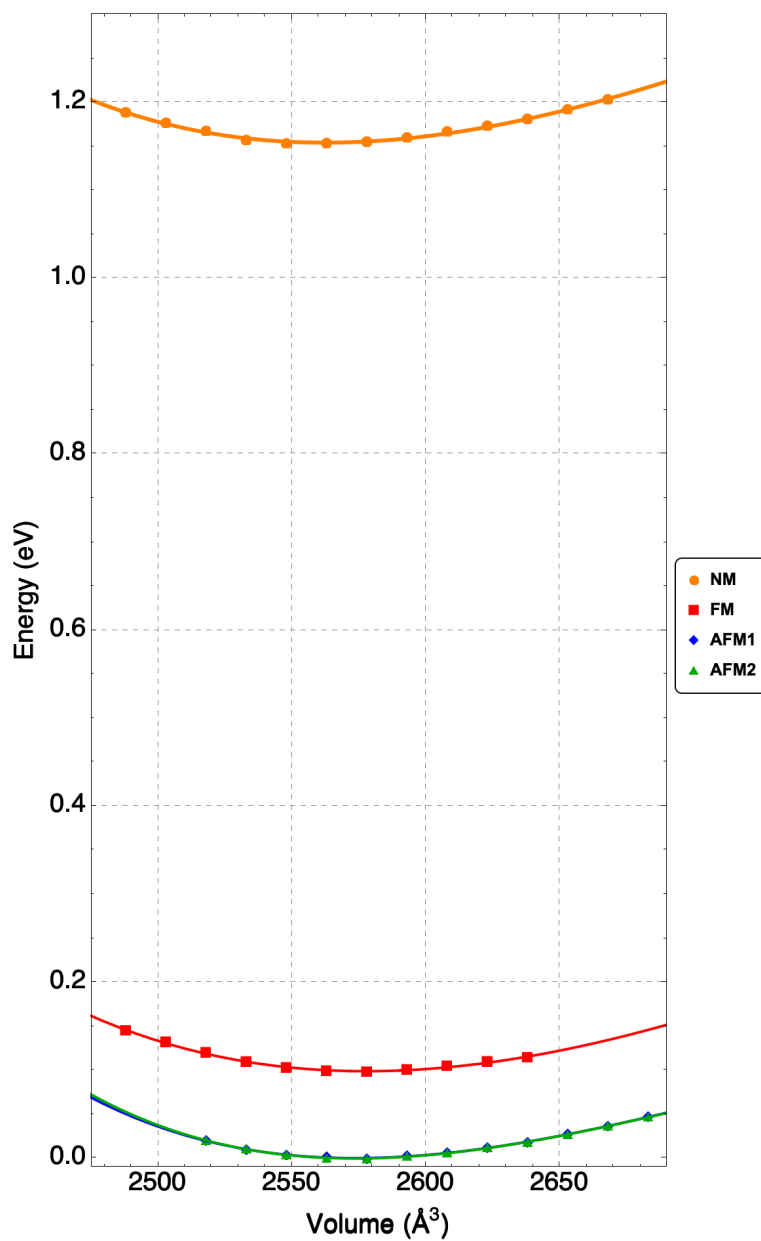


Figure 4.8: Birch-Murnaghan equation of states of M5-Br fitted with data obtained by relaxation with functionals  $r^2$ SCAN+rVV10.

Table 4.6: Mean electrostatic potential at pore for each M5-Br magnetic state.

	AFM1	AFM2	FM	NM
Potential (eV)	3.93	3.92	3.92	3.94

### 4.3.2 Density of States & Band Alignment

The partial density of states (PDOS) was computed with the hybrid functional HSE06. DOS was obtained for each magnetic states, all of them show similar electronic properties but the non-magnetic case, which has smaller values for band gap and workfunction,  $E_g = 0.81$  eV and  $\Phi = 5.88$  eV, respectively. The band gap for the AFM1, AFM2 and FM states are  $E_g = 2.57$ ,  $2.63$  and  $2.56$  eV respectively showing reduced values compared to the MOF-F and MOF-Cl structures. In the same way, the values for the workfunction are also reduced. Partial DOS is shown in Fig 4.9. Here we can see that the three magnetic states also present LMCT and LLCT. As in the case of M5-F, Cl, NM state only presents metal-to-metal excitation. Band energies are aligned to vacuum levels of each porous MOF. Figure 4.7 shows 2D perpendicular planes along the three lattice vectors showing the pore as well as contour map for the electrostatic potential. This procedure is repeated for each spin arrangement and values are reported in table 4.6. MOF-Br vacuum energy levels are further reduced, in accordance to what one would expect since bromide is less electronegative than Cl and F.

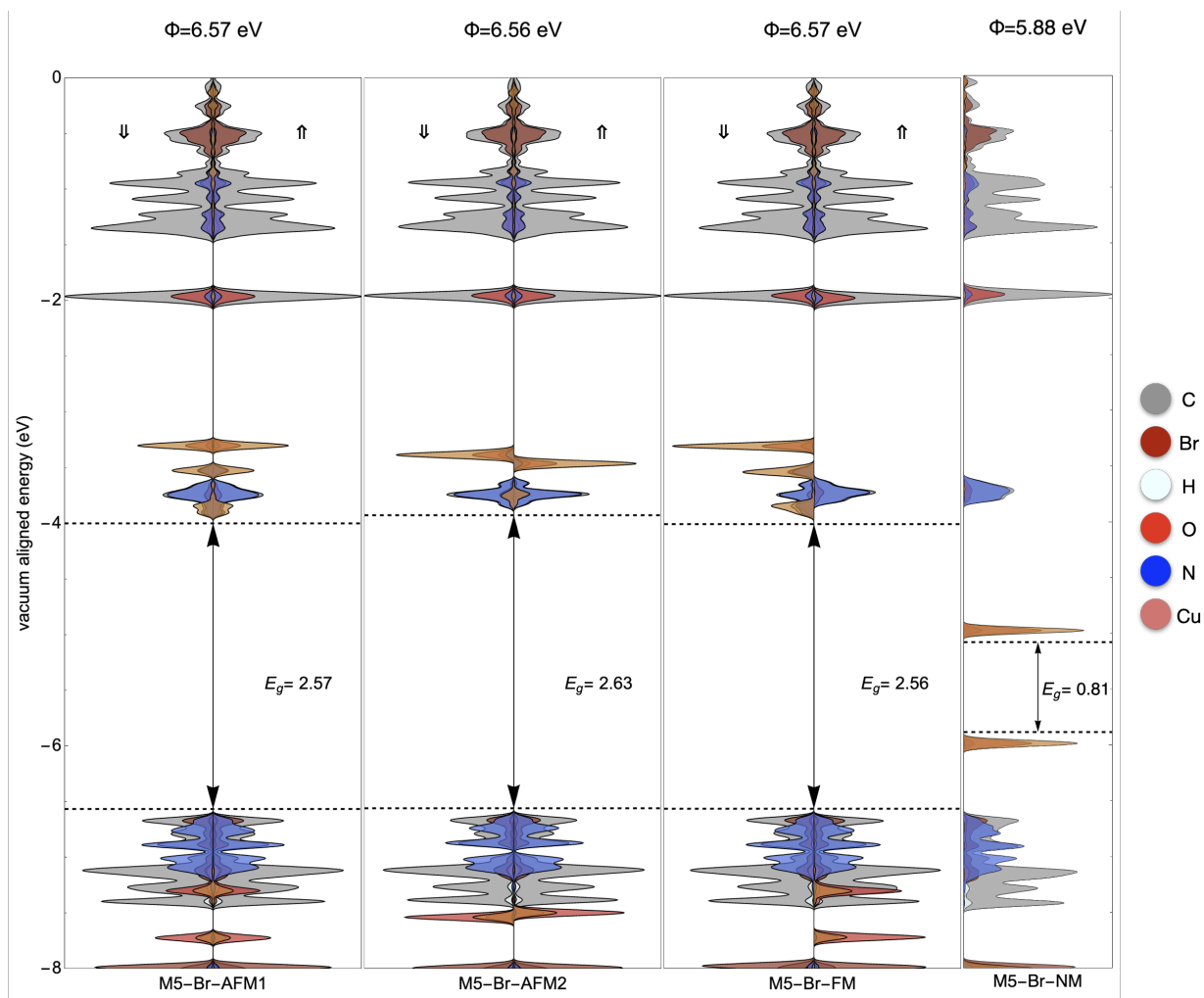


Figure 4.9: Spin-separated atomic pDOS ( $r^2$ SCAN+rVV10//HSE06) for all MOF-Br magnetic configurations. Band gap ( $E_g$ ) and band edge positions are aligned with their vacuum level according to table 4.6. Nomenclature is given by MOF name-SBU functionalization-Magnetic state (e.g. M5-Br-NM). Workfunction is represented by the greek letter  $\Phi$ .



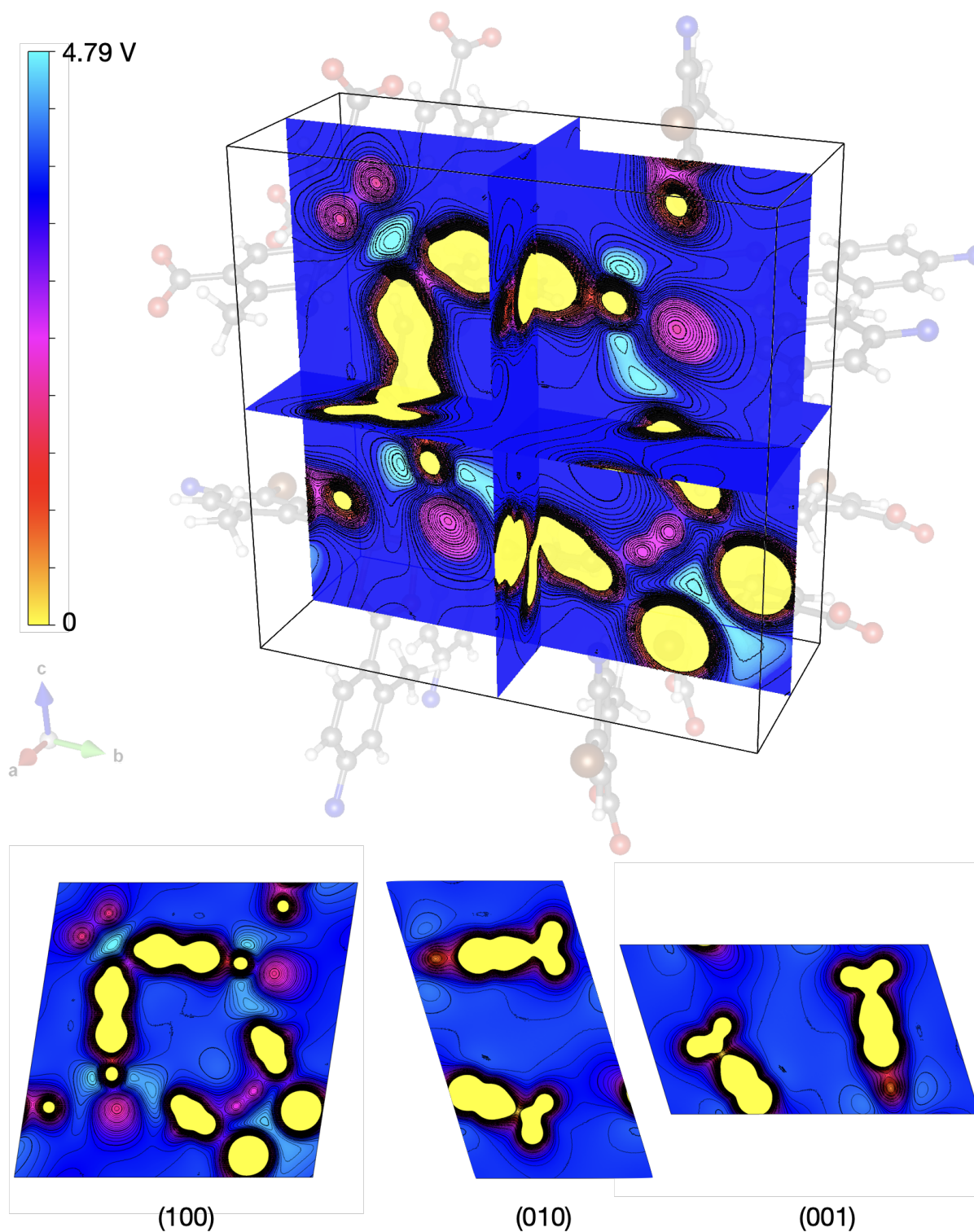


Figure 4.10: Contour plot of 2D sections at half the distance of the lattice vectors showing the electrostatic potential of M5-Br-AFM2. The intersection of the three planes is taken as the center of the pore. In the bottom, each 2D plane with the corresponding Miller indices. Color code same as Fig. 4.9.

## 4.4 Photocatalysis Activity

Previously, it was stated that for photocatalysis to happen it is necessary that the reduction/oxidation potentials energy levels should lie within the band gap for a given semiconductor. That is, for water splitting, the highest occupied crystal orbit (HOCO) energy should be lower than the energy level of the oxygen evolution reaction (OER),  $H_2O \leftrightarrow 2H_{(aq)}^+ + 1/2 O_{2(g)} + 2e^-$ ; and the lowest unoccupied crystal orbit (LUCO) energy should be higher than the energy level of the hydrogen evolution reaction (HER)  $2H_{(aq)}^+ + 2e^- \leftrightarrow H_{2(g)}$ . For CO<sub>2</sub> reduction, the LUCO energy of the photocatalyst should be higher than the energy level of the CO<sub>2</sub> reduction reaction, which depends on the product. Table 4.7 specifies the electrode potential and the free energy change per electron of a reduction reaction at room temperature (298.15 K) and ph = 7 for some selected reactions.

Then, plotting these energy levels corresponding to their redox potentials it is possible to filter out promising MOF-X candidates for photocatalysis. Figure 4.11 shows the band gaps and absolute band edge positions (respect to vacuum level) for all twelve configurations; dashed green (dark yellow) lines represent energy levels corresponding to redox potentials to which CO<sub>2</sub> reduction is (not) feasible. In the same way, dashed purple (light purple) lines represent energy levels corresponding to redox potentials to which water splitting is (not) feasible.

Figure 4.11 is a compact way to represent band edge positions and aligned redox potentials. However, it misses information about the density of states. Figure 4.12 shows that although the redox potential levels are above the lowest unoccupied crystal orbital (LUCO), these still overlap with the free available energy states in the CBM, which suggests MOF-X-AFM2 state (the most stable state) is shown to be a potential photocatalyst for OER and to reduce CO<sub>2</sub> into three different carbon-based fuels, C<sub>2</sub>H<sub>4</sub>, C<sub>2</sub>H<sub>5</sub>OH, CH<sub>4</sub>.

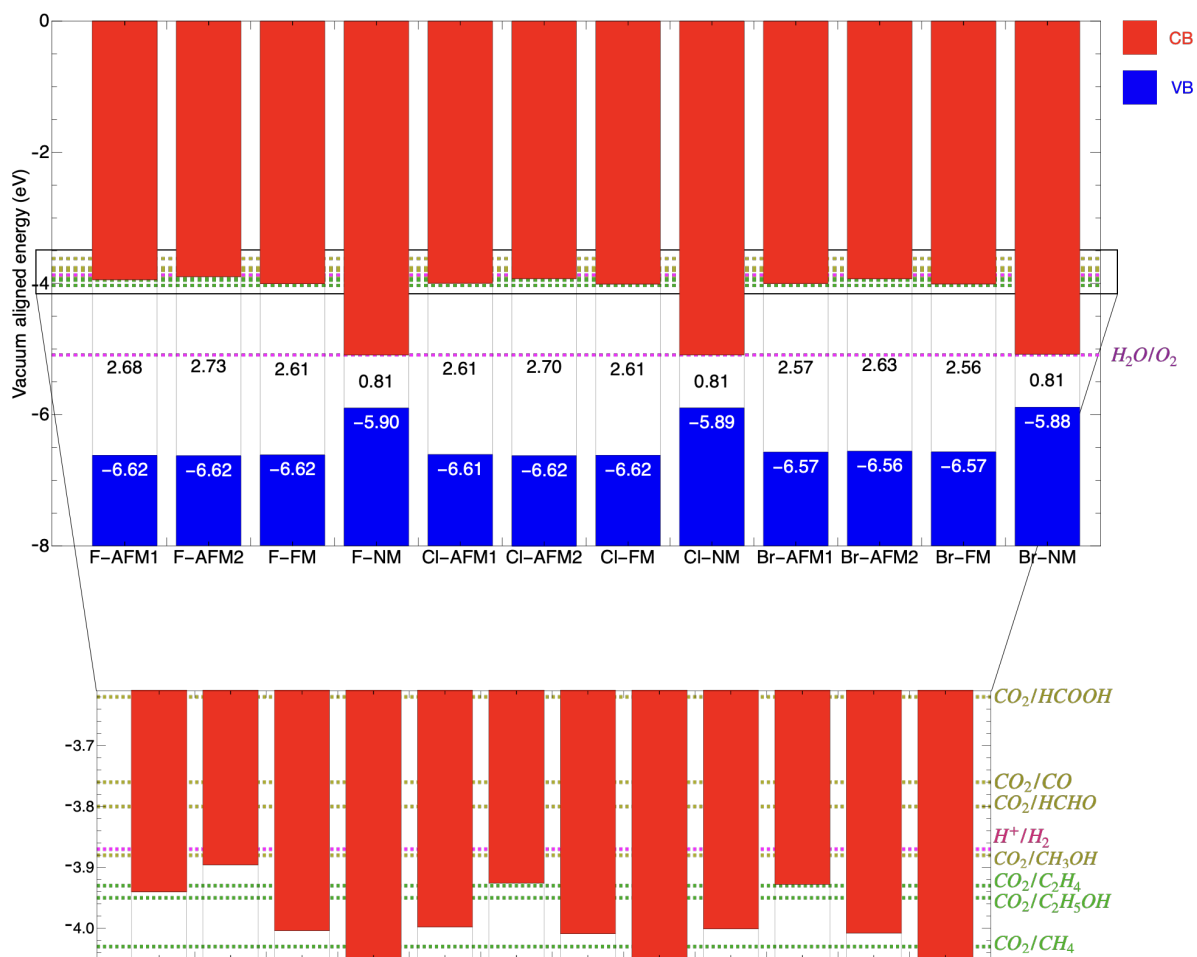


Figure 4.11: Absolute band edge positions and bandgaps for magnetic states of MOF-F, Cl, Br. Magenta dashed lines represent energy levels corresponding to redox potentials for water splitting, and the green and dark yellow lines represent energy levels corresponding to redox potentials for various  $CO_2$  reduction reactions as listed in Table 4.7. A zoom of the region of interest is depicted in the bottom.

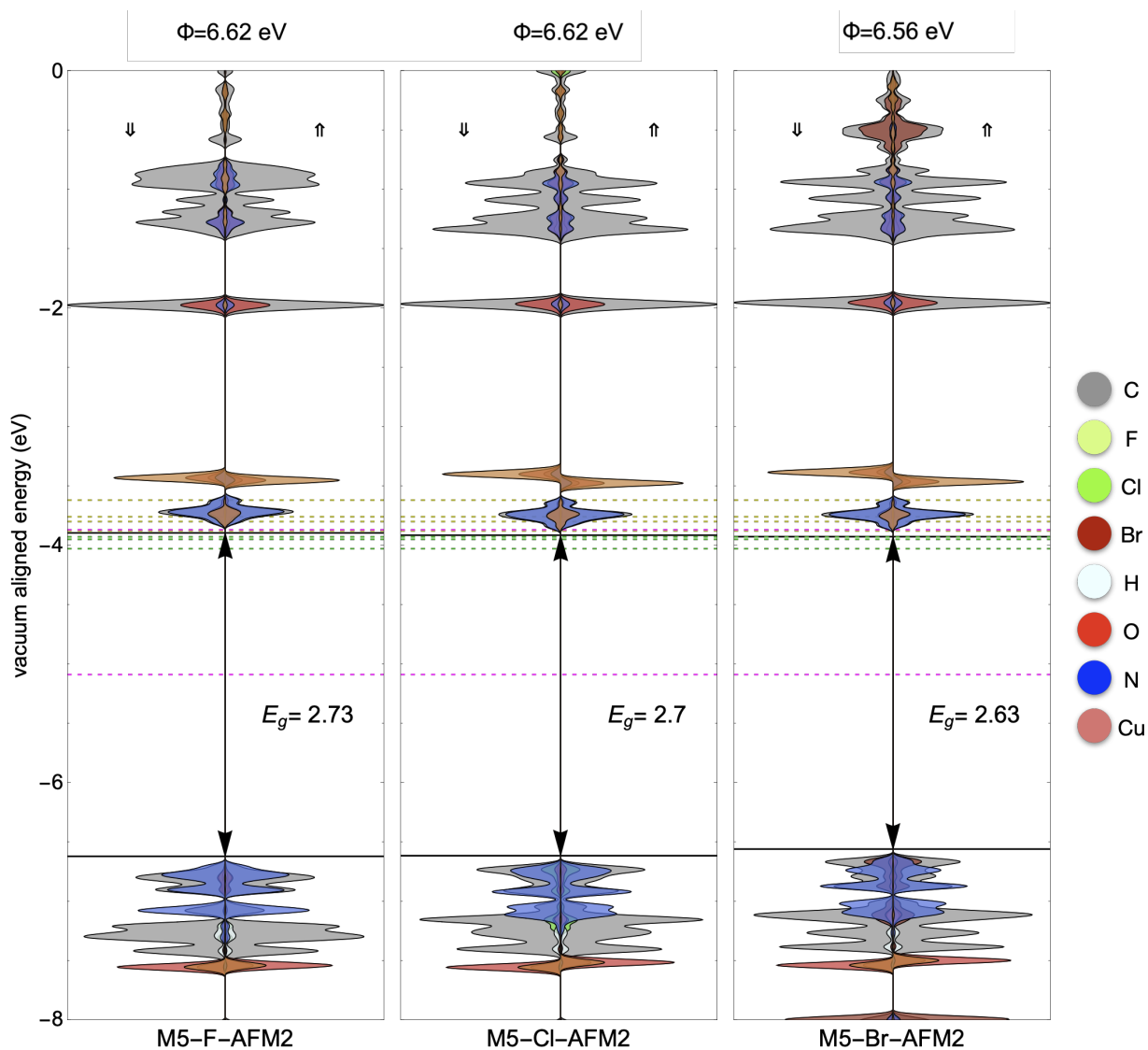


Figure 4.12: Absolute band edge positions and band gaps of all AFM2 states. Purple, green and dark yellow dashed lines represent the same redox potential energy as Fig 4.11. Although some  $\text{CO}_2$  reduction reactions fall above the LUCO, they still overlap with available states in the CBM.

Table 4.7: Standard electrode potentials ( $\varepsilon^\circ$ , in V) and  $\Delta G$  (in eV) at pH = 7 and T = 298.15 ) of selected reactions. Taken from<sup>3</sup>.

Reaction	$\varepsilon^\circ$	$\Delta G$
$H^+/H_2$	0	-3.87
$H_2O/O_2$	1.229	-5.09
$CO_2/HCOOH$	-0.250	-3.62
$CO_2/CO$	-0.106	-3.76
$CO_2/HCHO$	-0.070	-3.80
$CO_2/CH_3OH$	0.016	-3.88
$CO_2/C_2H_4$	0.064	-3.93
$CO_2/C_2H_5OH$	0.084	-3.95
$CO_2/CH_4$	0.169	-4.03

## 4.5 Defects

As it was seen in the previous sections, the density of states of MOF-F, Cl, Br did present ligand-to-metal charge transfer. However, bands belonging to the SBU were not alone in the conduction band minimum, i.e. there is mixing of node and linker available energy states in the CBM. It is possible that the photocatalysis process can be affected by this, to try and isolate node-states only we have introduced defect by substitution into MOF-F-AFM2 as explained in Section 3. The reason to choose this configuration in particular has to be with its greater band gap, which as we saw in Sec 4.4 makes it the best candidate for CO<sub>2</sub> reduction.

### 4.5.1 Zirconium substitution (Def-Zr)

Relaxation with functionals r<sup>2</sup>SCAN+rVV10 yielded the optimal structure, crystal parameters can be found in table 4.8. Zirconium substitution into the nodes incremented the electrostatic potential at the pore giving a mean EP of 4.10 eV. However, the workfunction energy is reduced due to a change in the VBM position which also brings smaller band gap of Def-Zr,  $\Phi = 4.69$  eV and  $E_g = 0.78$  eV. Density of states also shows difference, Def-F no longer presents LMCT or LLCT, instead metal-to-metal and metal-to-ligand transitions are present. This is due to higher Zr orbitals (e.g. **d** orbitals. cf Section B) being occupied shifting the whole valence band down.

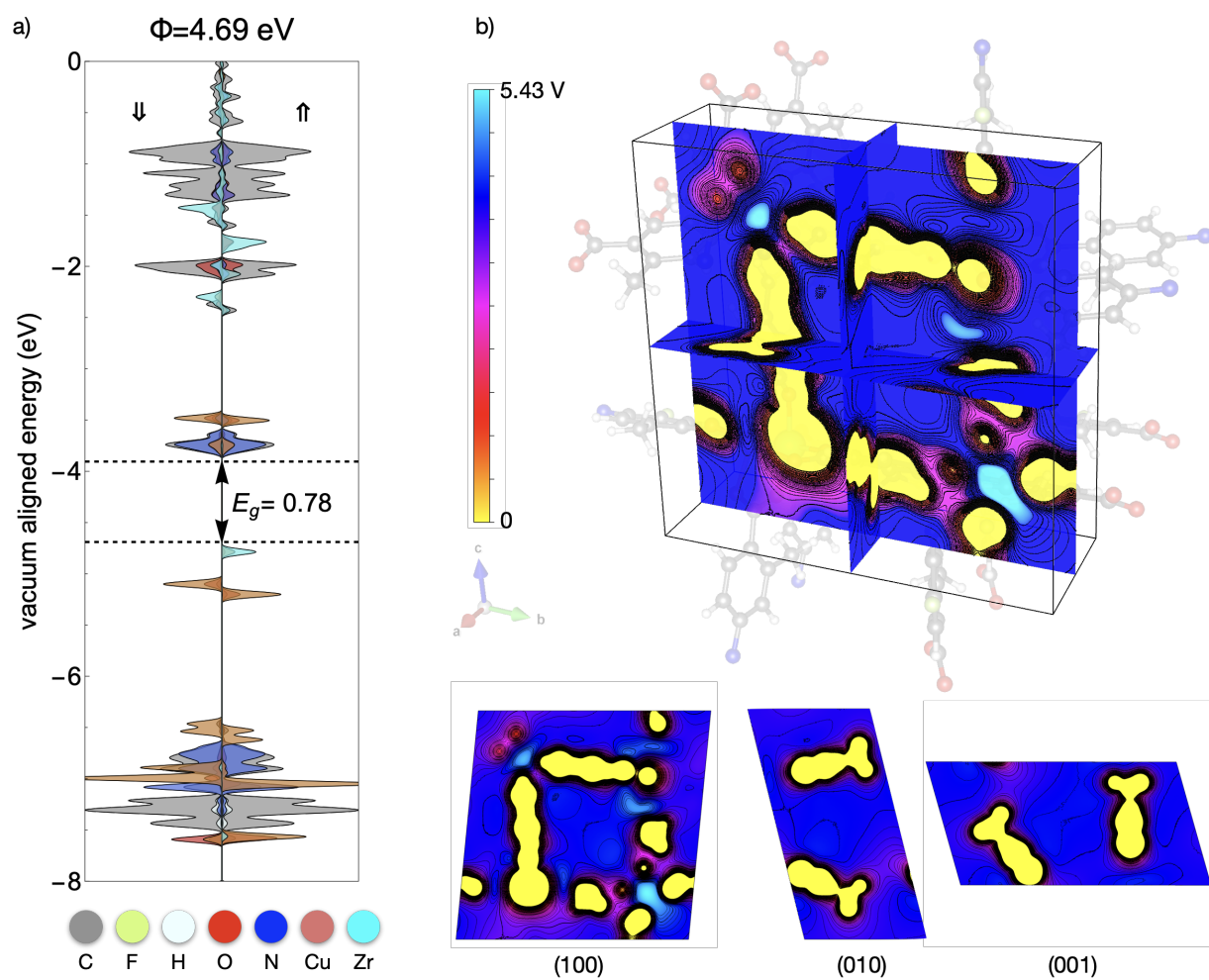


Figure 4.13: **a)** Aligned spin-separated atomic pDOS ( $r^2$ SCAN+rVV10//HSE06) of Def-Zr, **b)** 3D view of Def-Zr with electrostatic potential 2D sections contour map at half the distance of lattice vectors.

Table 4.8: Computed  $r^2$ SCAN+rVV10 crystallographic data and properties of Def-Zr, Mg.  $a$ ,  $b$ ,  $c$  are the lattice parameters and the corresponding angles  $\alpha$ ,  $\beta$  and  $\gamma$ . The optimal volume  $V$ , bulk modulus  $B_0$ . The relative energy  $\Delta E$  with respect to the most stable phase AFM2 and the absolute values of the local magnetic moment  $|m_{\text{Cu}}|$  at the Cu sites are computed from the  $r^2$ SCAN+rVV10//HSE06 results.

Property	Calculated ( $r^2$ SCAN+rVV10)	
	Zr	Mg
Space group	P1	
$a$ (Å)	8.79	8.82
$b$	17.17	17.06
$c$	17.02	17.02
$\alpha$	84.45	83.96
$\beta$	76.09	75.22
$\gamma$	74.18	74.69
Volume (Å <sup>3</sup> )	2400.53	2387.33
$B_0$ (GPa)	3.16	3.17

#### 4.5.2 Magnesium substitution (Def-Mg)

Relaxation with functionals  $r^2$ SCAN+rVV10 yielded the optimal structure, crystal parameters can be found in table 4.8. Magnesium substitution into the nodes showed similar EP values in the pore. Band gap and workfunction values were recovered indicating VBM was similar to the original case (M5-F-AFM2),  $E_g = 2.70$  and  $\Phi = 6.60$  eV. In this context, the density of states remains similar in the valence band. Additionally, Def-Mg also presents the same original band gap transitions, i.e. LCMT and LLCT excitations which also makes it a good candidate for photocatalysis.

Finally, plotting Def-Zr, Mg density of states against HER, OER and CO<sub>2</sub> reduction/oxidation reactions we can notice Def-Zr is not a candidate for photocatalysis, however, since Def-Mg DOS is similar to M5-F-AFM2, it has a band gap inside the visible and spectra and presents the transitions desired, it is a potential catalyst for the compound already mentioned throughout this work.

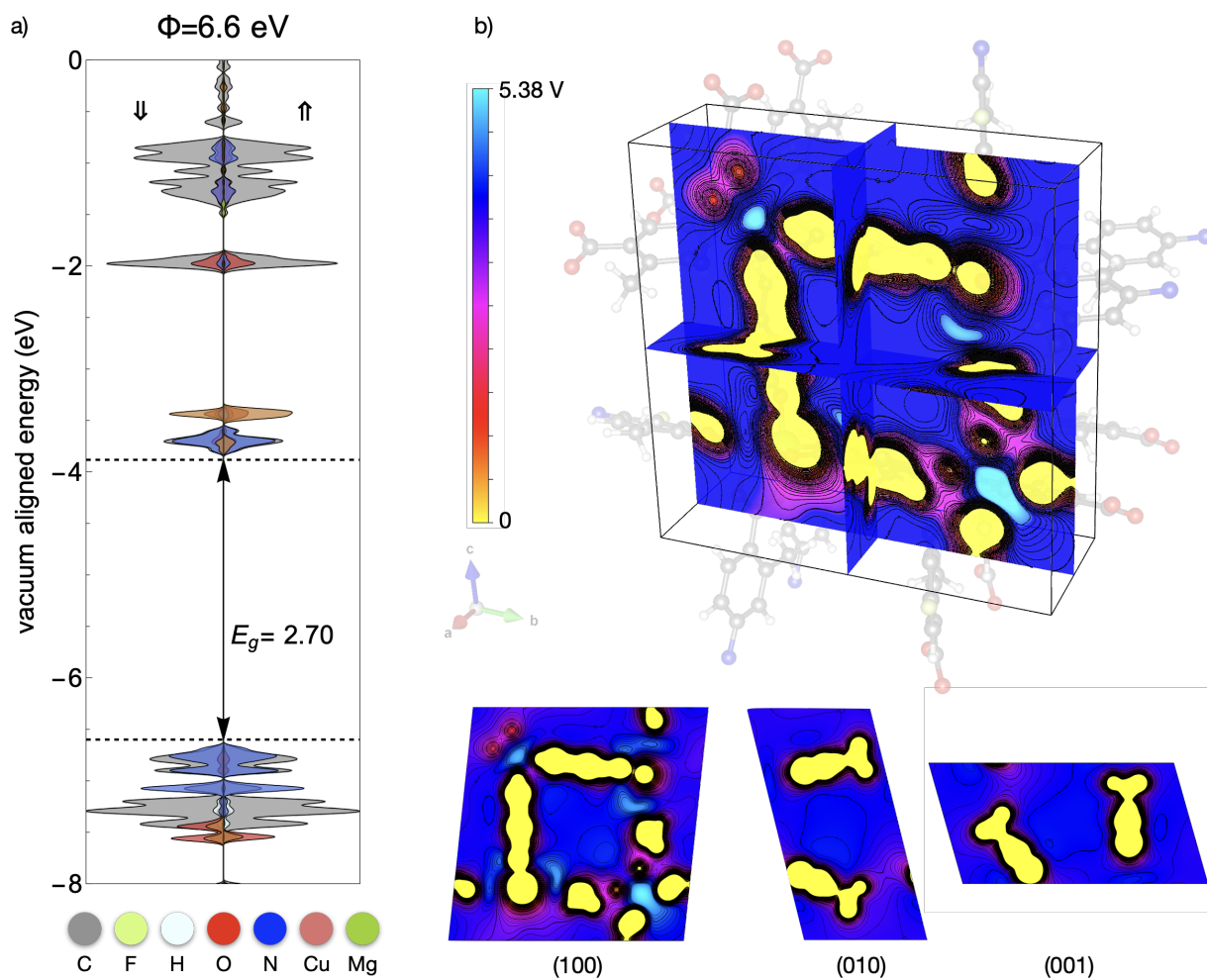


Figure 4.14: **a)** Aligned spin-separated atomic pDOS ( $r^2$ SCAN+rVV10//HSE06) of Def-Zr, **b)** 3D view of Def-Mg with electrostatic potential 2D sections contour map at half the distance of lattice vectors.



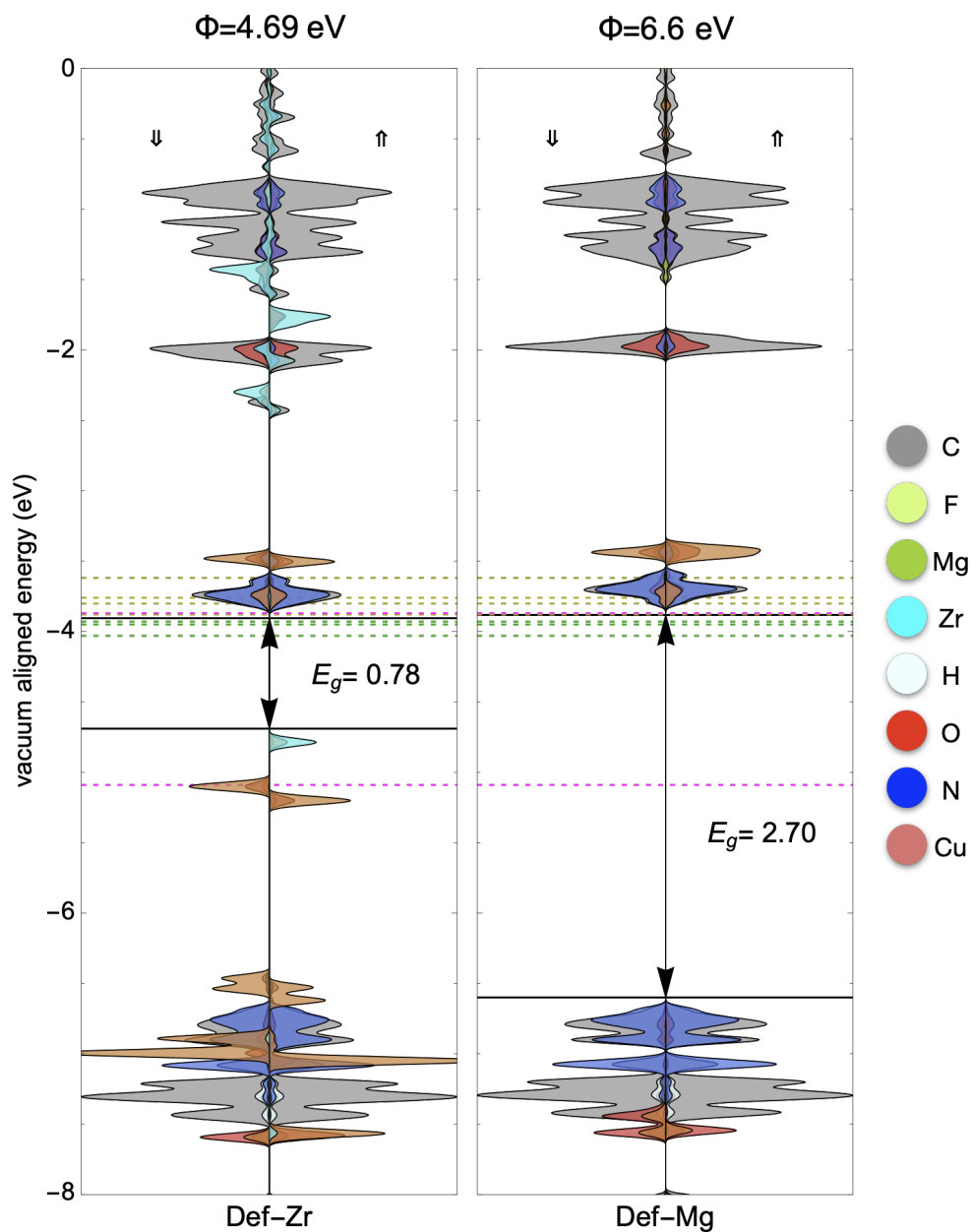


Figure 4.15: Absolute band edge positions and band gaps of Def-Zr, Mg. Purple, green and dark yellow dashed lines represent the same redox potential energy as Fig 4.11. Although some CO<sub>2</sub> reduction reactions fall above the LUCO, they still overlap with available states in the CBM.

## Chapter 5

# Conclusions & Outlook

We have presented here computational analysis (spin-DFT) of H<sub>2</sub>ABDC-based MOF. Owing to linker functionalization by monosubstitution, we were able to study three different structures, each considering four magnetic states (NM, FM, AFM1, AFM2). Electronic properties were calculated using the Vienna Ab Initio Package (VASP) using a plane wave cut-off energy of 850 eV and a Monkhorst-Pack grid of  $2 \times 1 \times 1$  for  $k$ -points mesh.  $r^2$ SCAN+rVV10 + rVV10 functionals were used for electronic relaxation. The difference in electronic properties between magnetic and non-magnetic for MOF-F, Cl, Br highlights the importance of including the spin contribution in DFT calculations when dealing with MOFs. After electronic relaxation, it was found that the AFM2 state is the most stable configuration for MOF-X, X = F, Cl, Br; although stability depended on linker substitution which was the case for MOF-Br wherein AFM1 and AFM2 showed no difference in energy stability.

Spin-projected density of states was obtained with the hybrid functional HSE06. Band edge positions were aligned according to their vacuum level energy, which was calculated at the center of the pore. Workfunction and band gap values were similar between the nine magnetic states,  $\Phi = 6.5 - 6.6$  eV and  $E_g = 2.5 - 2.7$  eV except for the other three non-magnetic states which showed a reduced workfunction and band gap,  $\Phi = 5.9$  eV and  $E_g = 0.81$  eV. In the same way, all magnetic states showed ligand-to-metal charge transfer (LMCT) as well as ligand-to-ligand charge transfer (LLCT). Aligned band edge positions against redox potentials allowed to filter out which MOF act as catalysts for water splitting and CO<sub>2</sub> reduction. As it turns out, excitons created by LMCT have longer lifetimes than by other band gaps transitions. For this reason, it is preferable that if possible MOF show only ligand-to-metal excitations. With this objective in mind, two types of defects were analyzed using AFM2 state of MOF-F for its wide band gap: zirconium

and magnesium node substitution.

Zirconium substitution changed original electronic structure and showed a reduced band gap value outside the visible spectra. Furthermore, it lost LMCT and LLCT transitions making it not a favorable model. On the other hand, magnesium substitution preserved some features such as similar workfunction and a band gap value inside the visible spectra. Therefore, Def-Mg is also considered as possible catalysts for CO<sub>2</sub> reduction and water splitting, ruling out Def-Zr defect model.

In this way, our findings suggest MOFs<sub>5</sub>-ABDC-X (X = F, Cl, Br) are potential candidates for water splitting and CO<sub>2</sub> reduction. Building upon the results obtained, future work will focus on ABDC functionalization with I, NH<sub>2</sub>, NO<sub>2</sub>, and linker related defects that could present even better electronic properties.

## **Appendix A**

# **Detailed spin-projected atomic-pDOS**

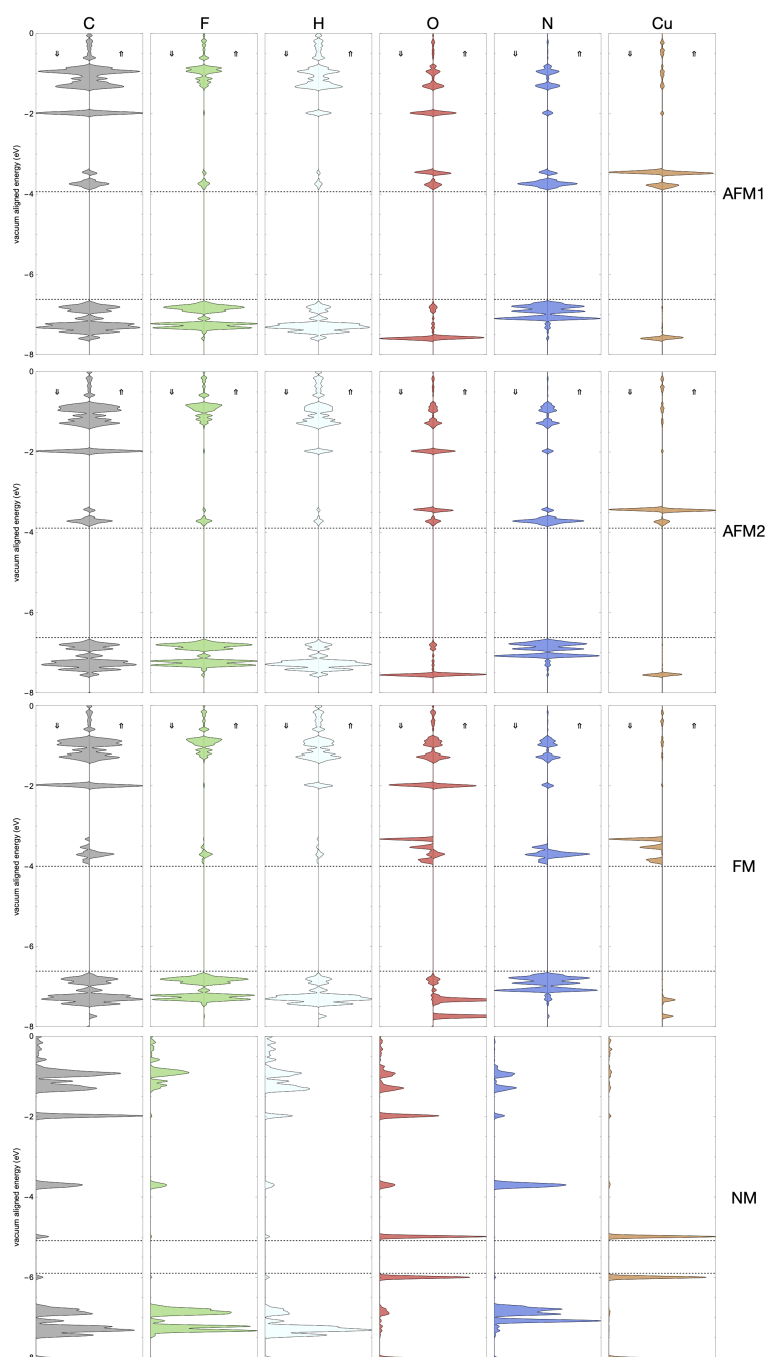


Figure A.1:  $r^2\text{SCAN}+r\text{VV10}/\text{HSE06}$  detailed atomic partial density of states for all M5-F magnetic configurations: antiferromagnetic AFM, ferromagnetic FM and non-magnetic NM.

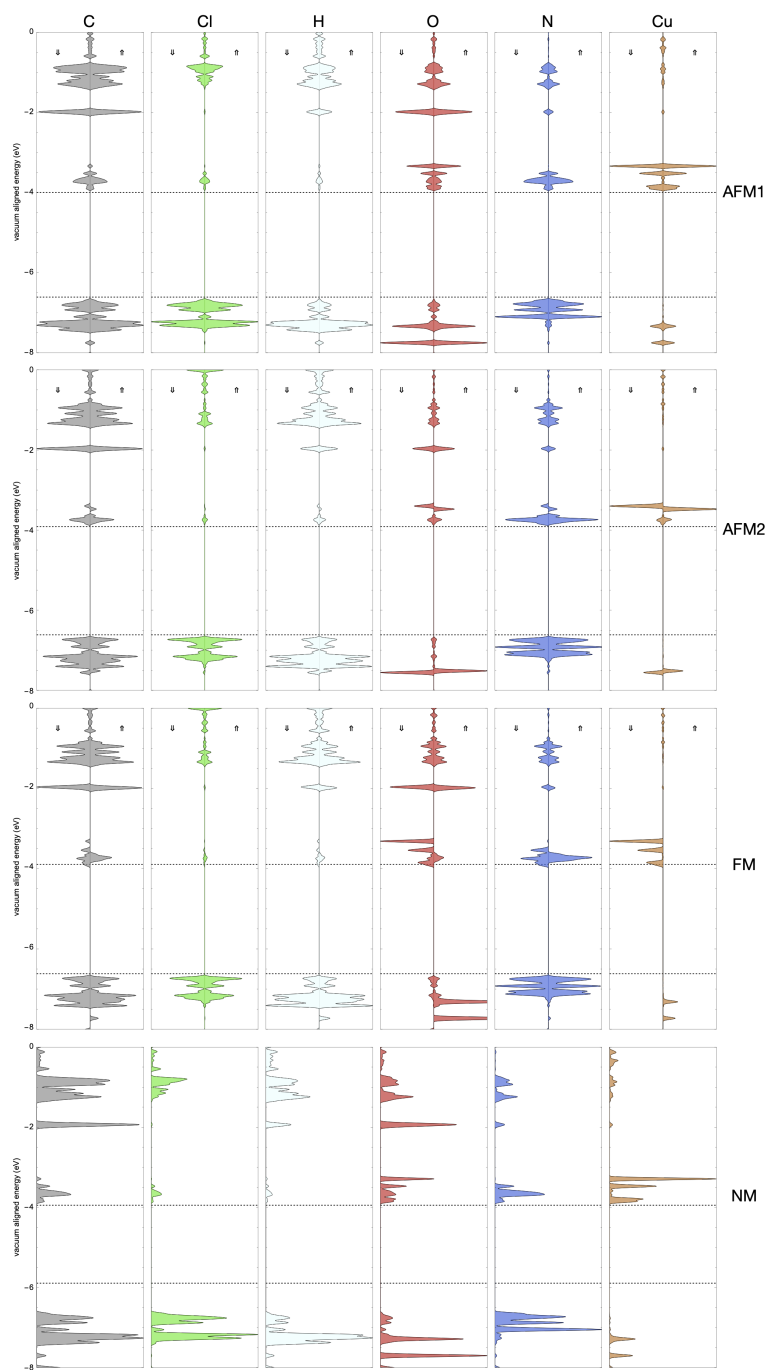


Figure A.2:  $r^2$ SCAN+rVV10/HSE06 detailed atomic partial density of states for all M5-Cl magnetic configurations: antiferromagnetic AFM, ferromagnetic FM and non-magnetic NM.

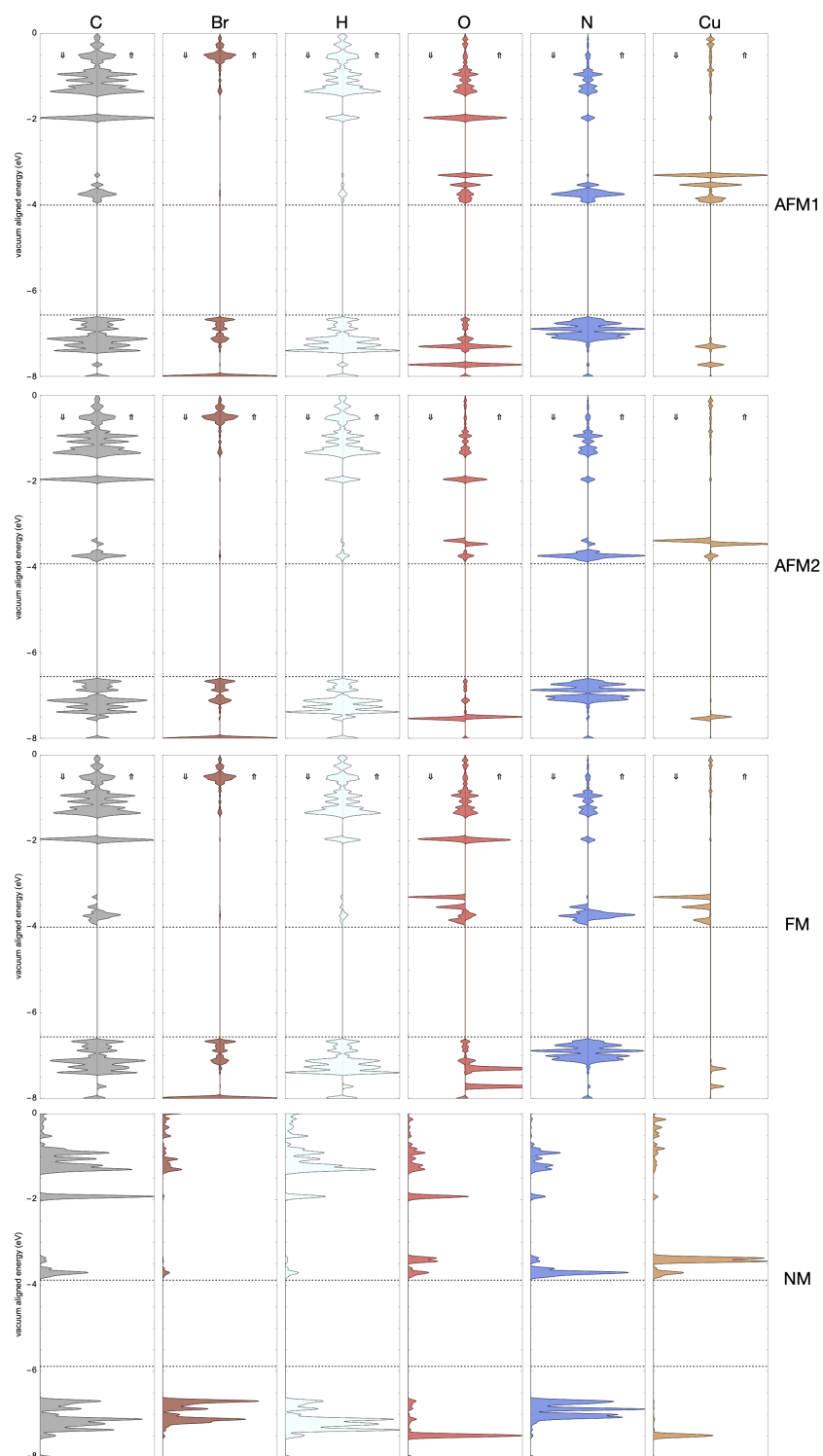


Figure A.3:  $r^2$ SCAN+rVV10/HSE06 detailed atomic partial density of states for all M5-Br magnetic configurations: antiferromagnetic AFM, ferromagnetic FM and non-magnetic NM.

## **Appendix B**

# **Detailed spin-projected atomic orbital-pDOS**



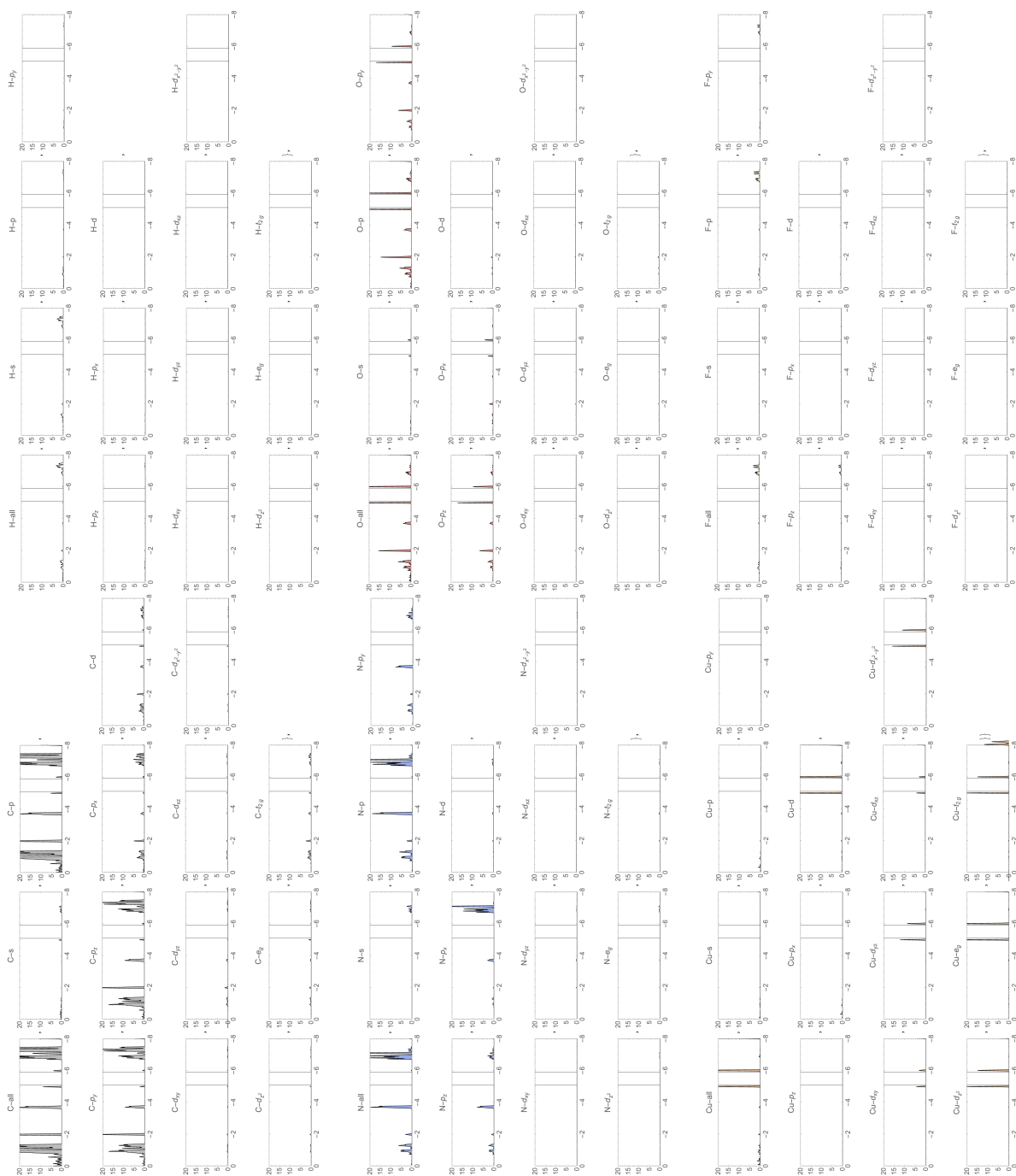
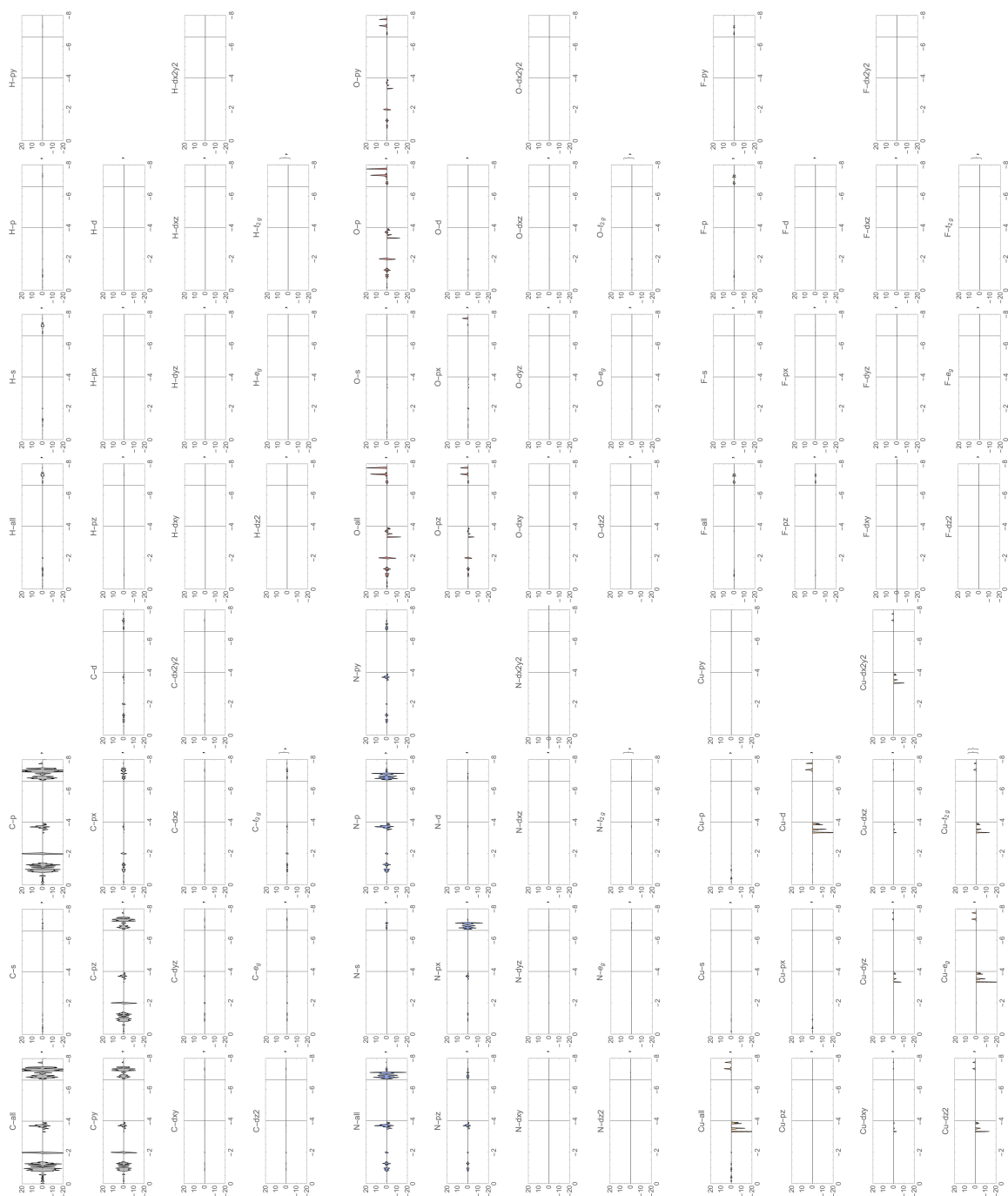


Figure B.1:  $r^2$ SCAN+rVV10/HSE06 detailed atomic orbital partial density of states of M5-F-NM.

Figure B.2:  $r^2$ SCAN+rVV10/HSE06 detailed atomic orbital partial density of states of M5-F-FM.

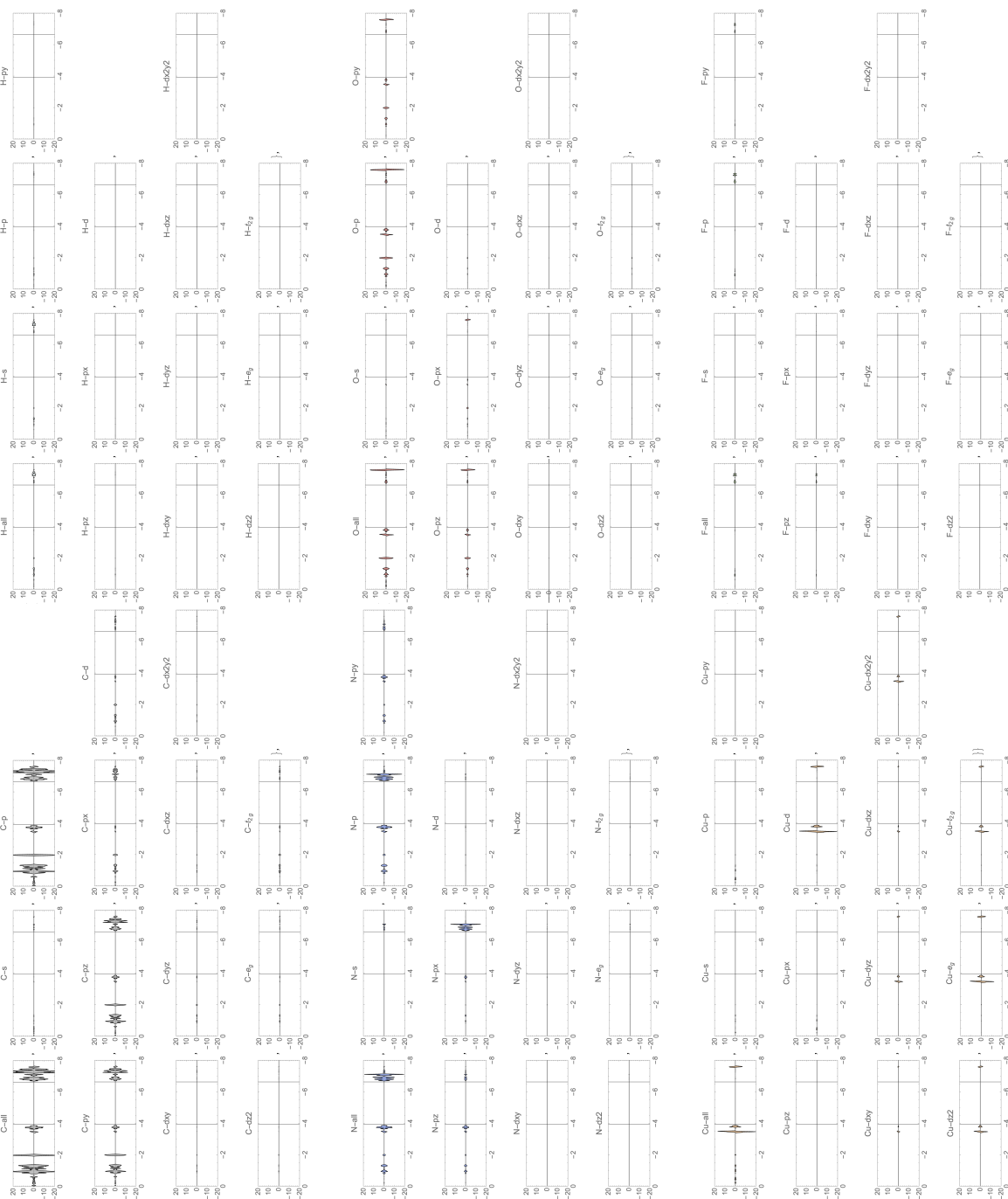


Figure B.3:  $r^2$ SCAN+rVV10/HSE06 detailed atomic orbital partial density of states of M5-F-AFM1.

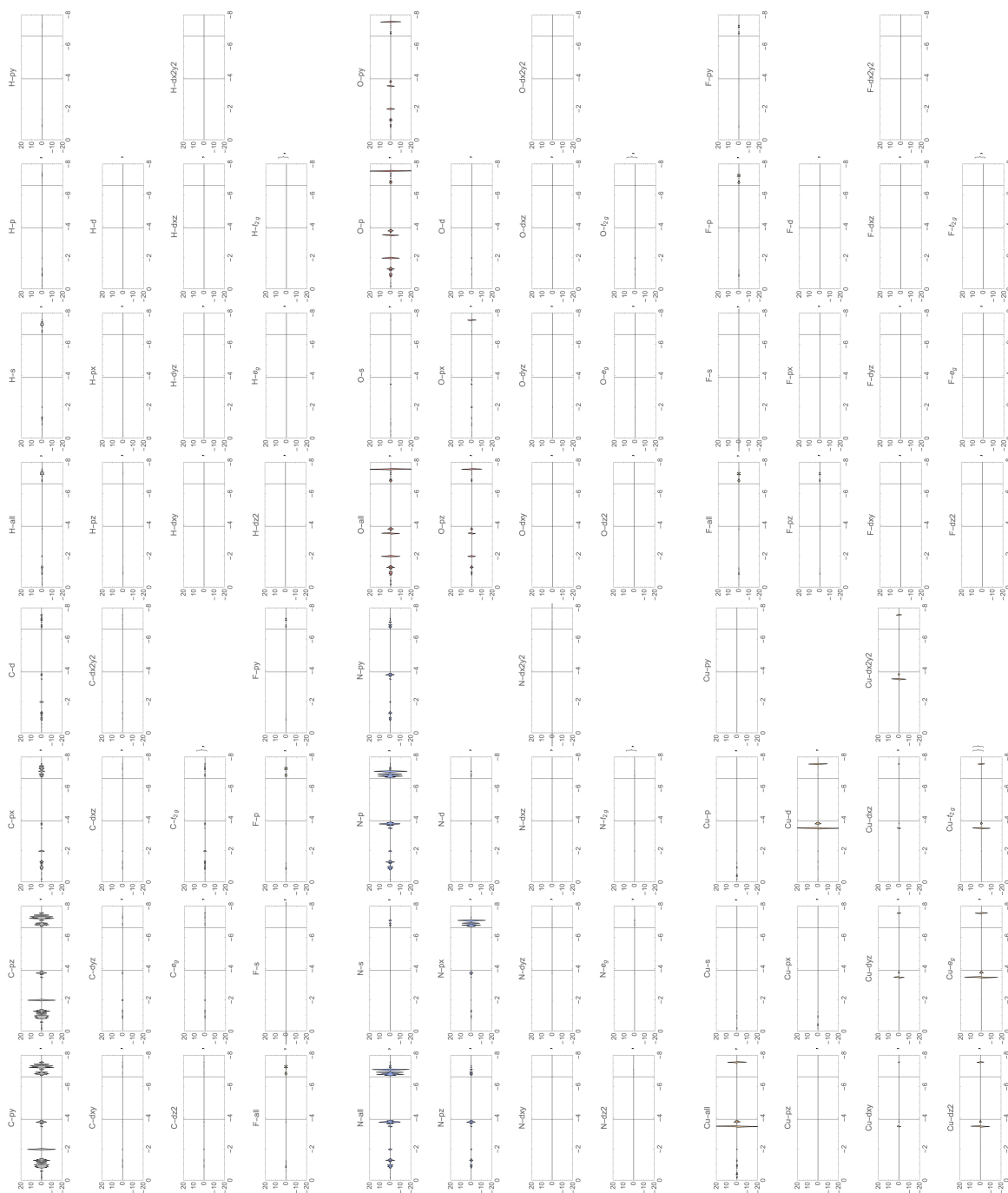


Figure B.4:  $r^2$ SCAN+rVV10/HSE06 detailed atomic orbital partial density of states of M5-F-AFM2.

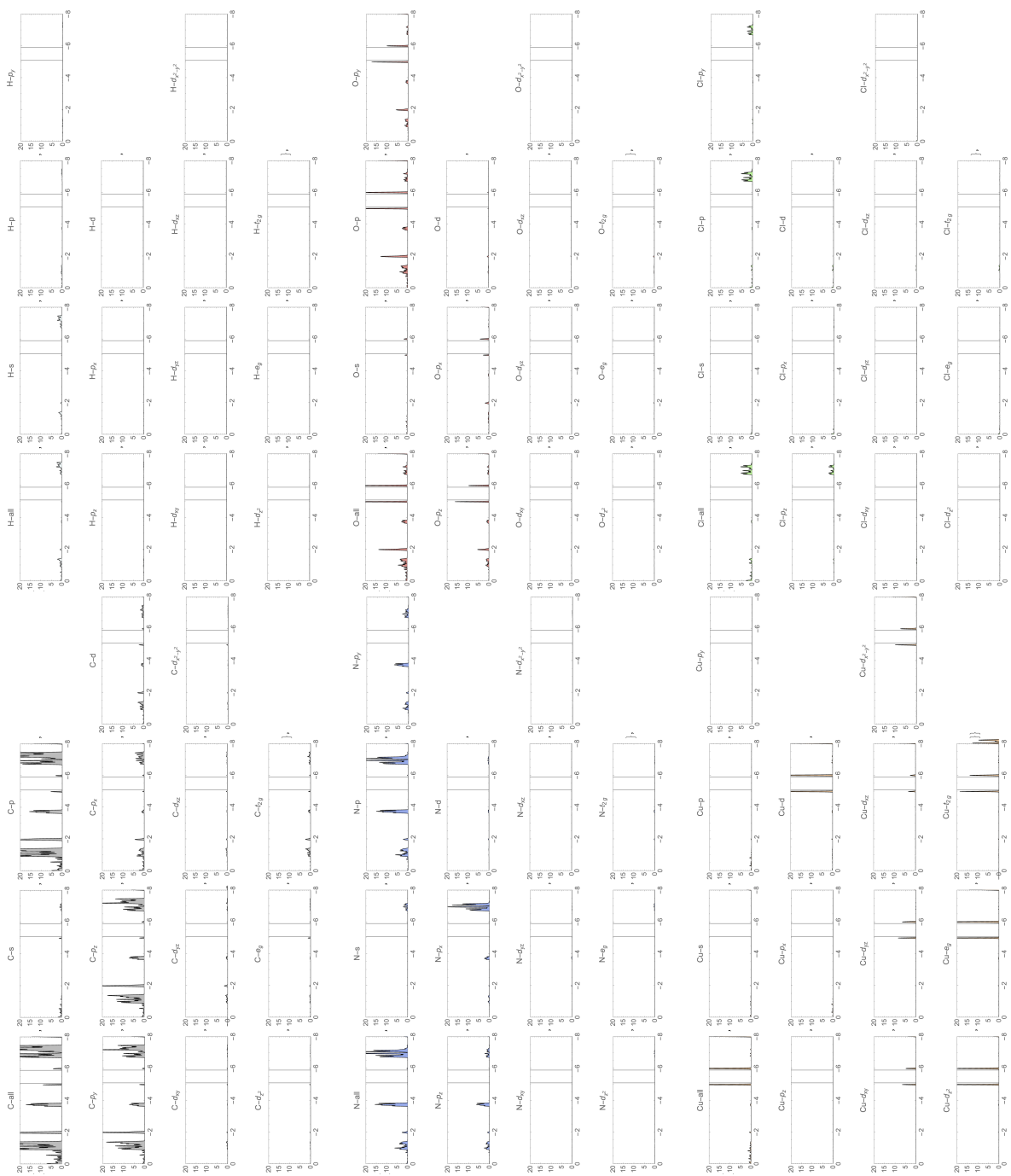
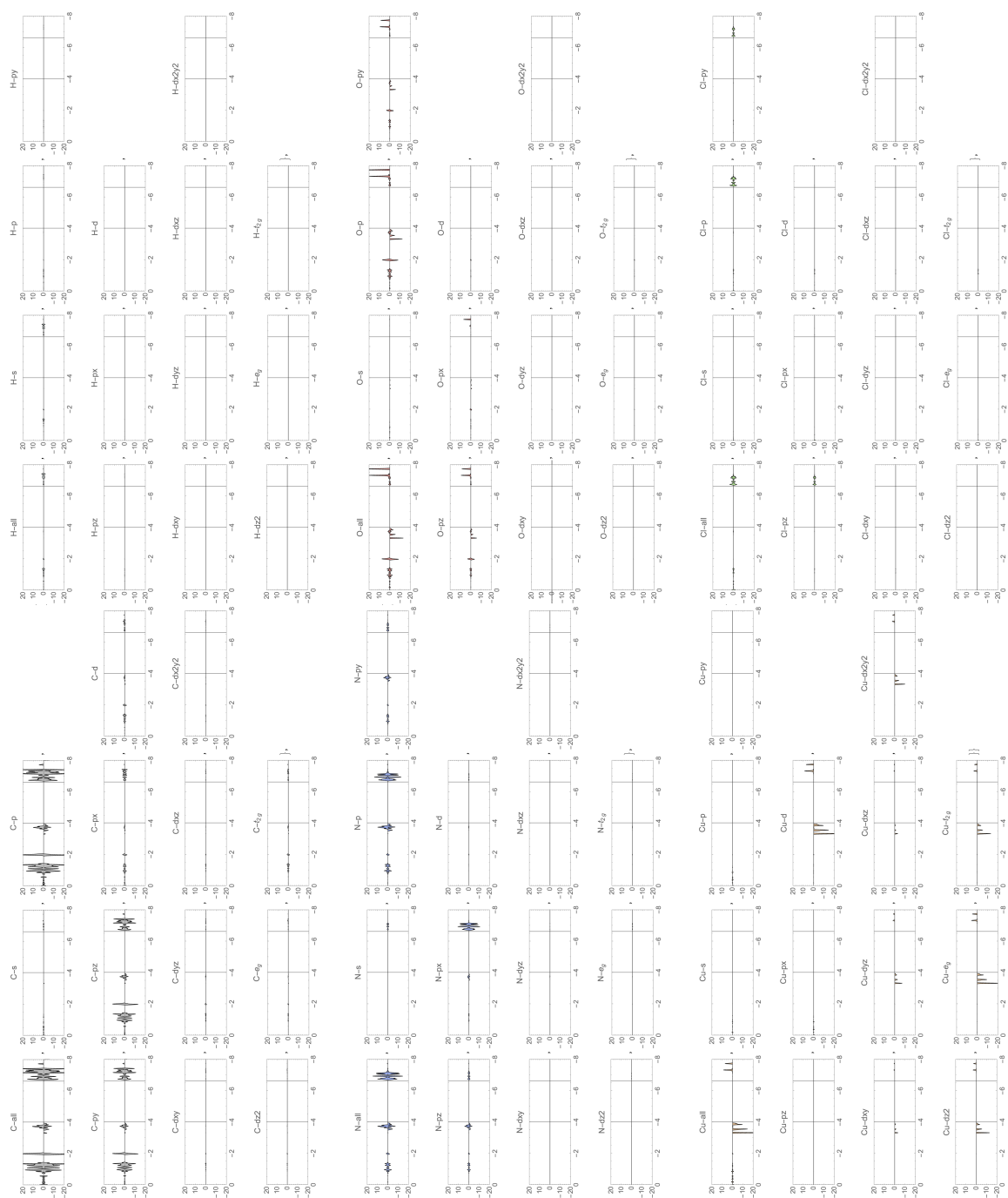


Figure B.5:  $r^2$ SCAN+rVV10/HSE06 detailed atomic orbital partial density of states of M5-Cl-NM.

Figure B.6:  $r^2$ SCAN+rVV10/HSE06 detailed atomic orbital partial density of states of M5-CI-FM.

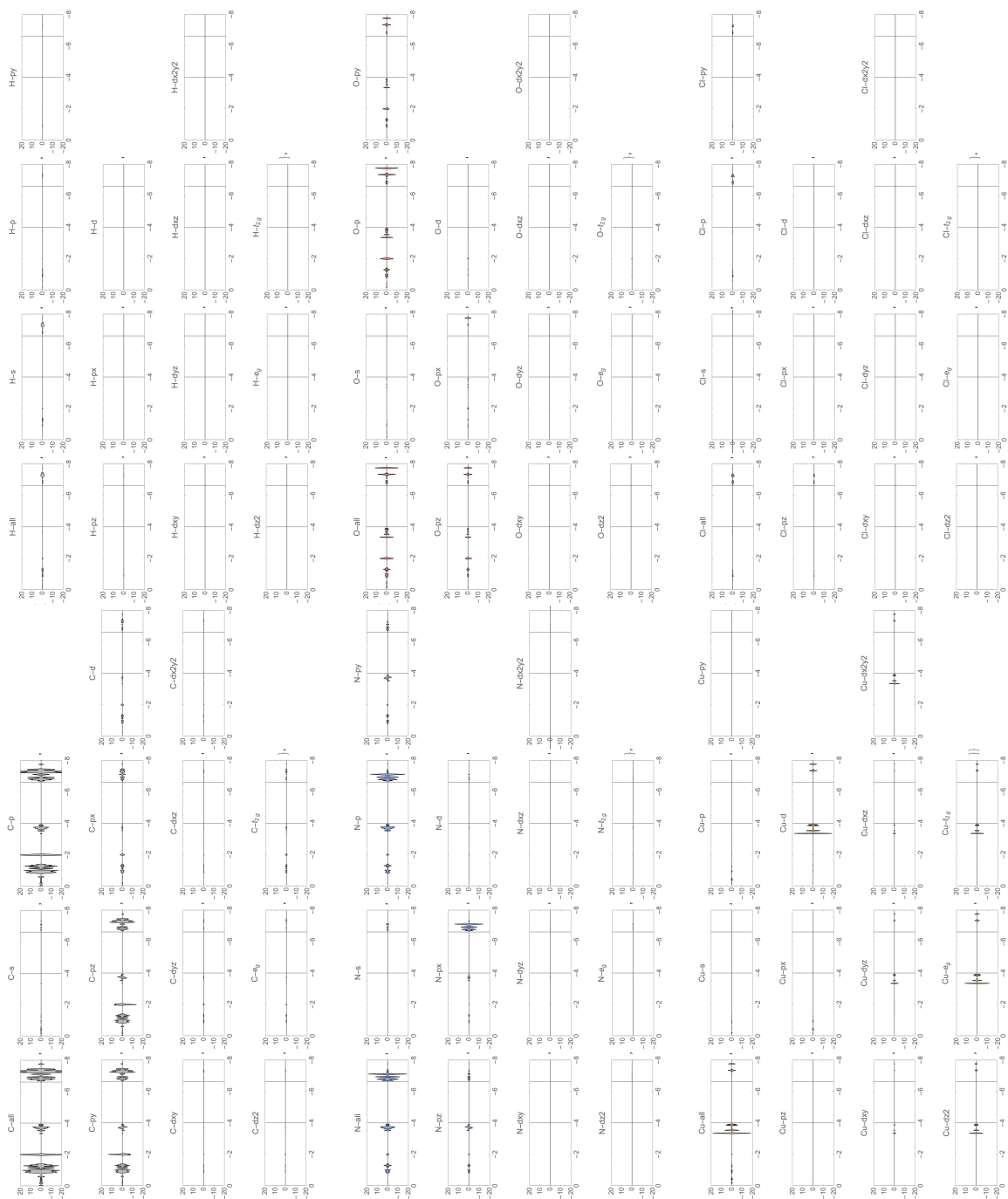
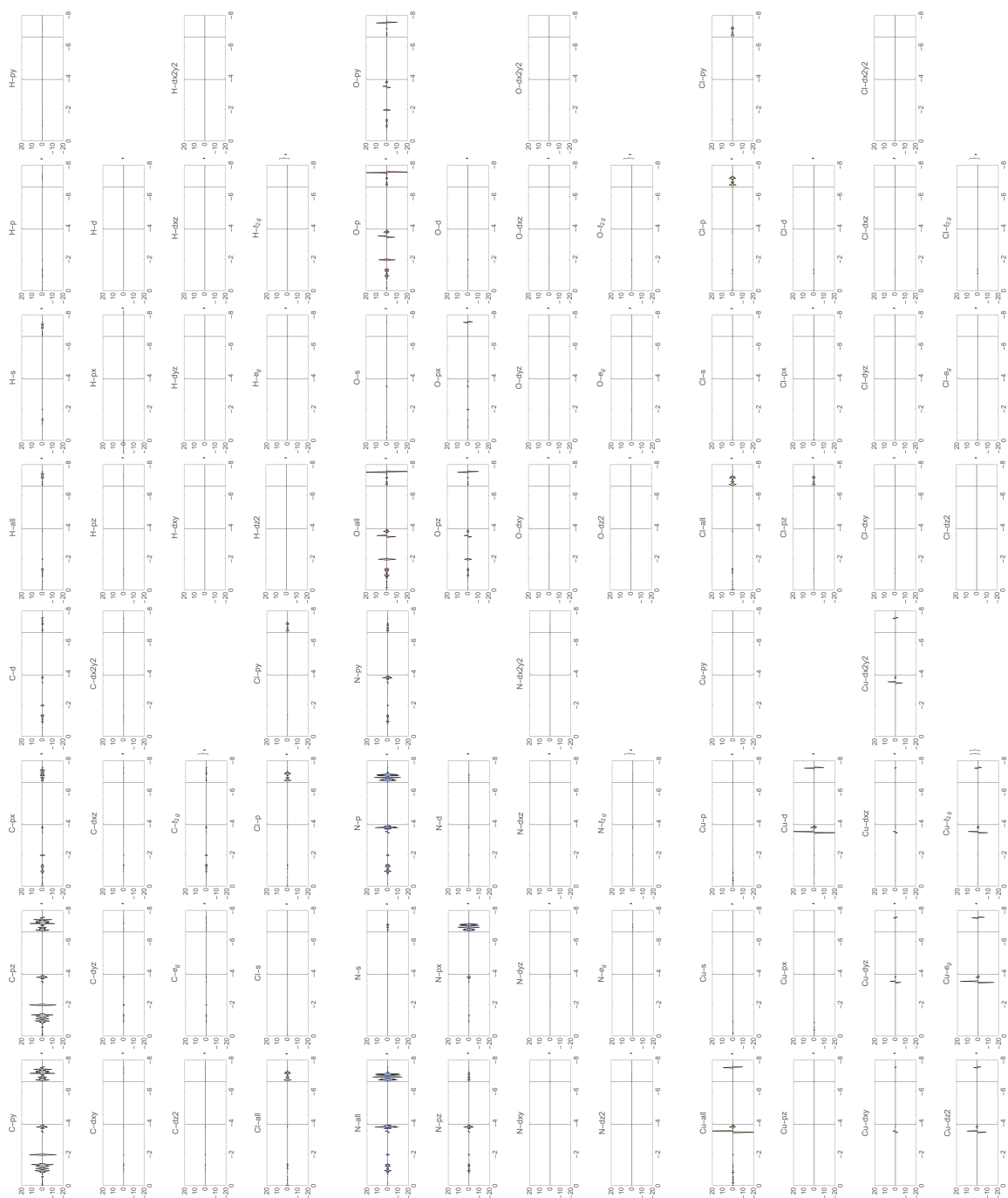


Figure B.7:  $r^2$ SCAN+rVV10/HSE06 detailed atomic orbital partial density of states of M5-Cl-AFM1.

Figure B.8:  $r^2$ SCAN+rVV10/HSE06 detailed atomic orbital partial density of states of M5-Cl-AFM2.



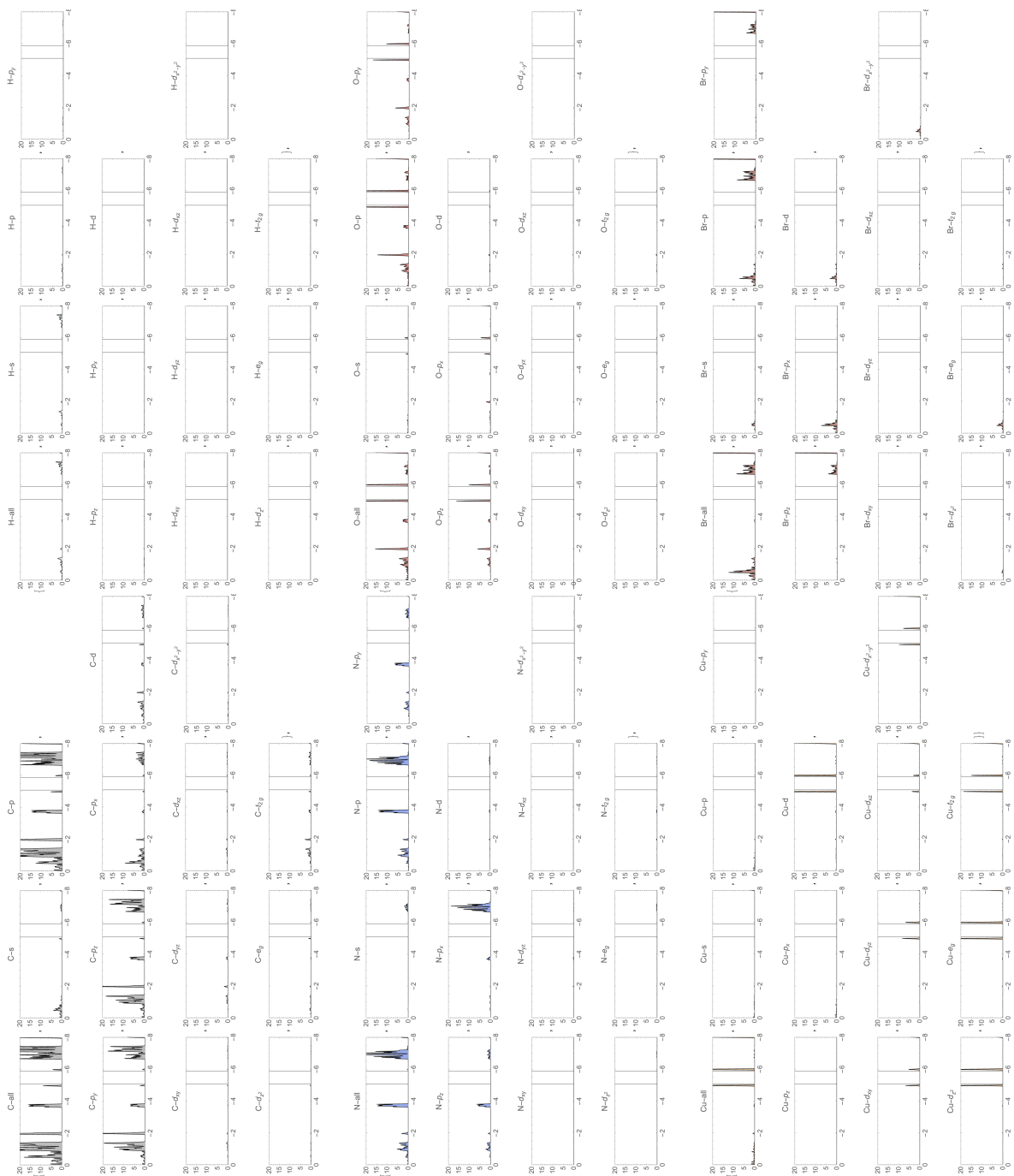


Figure B.9:  $r^2$ SCAN+rVV10/HSE06 detailed atomic orbital partial density of states of M5-Br-NM.

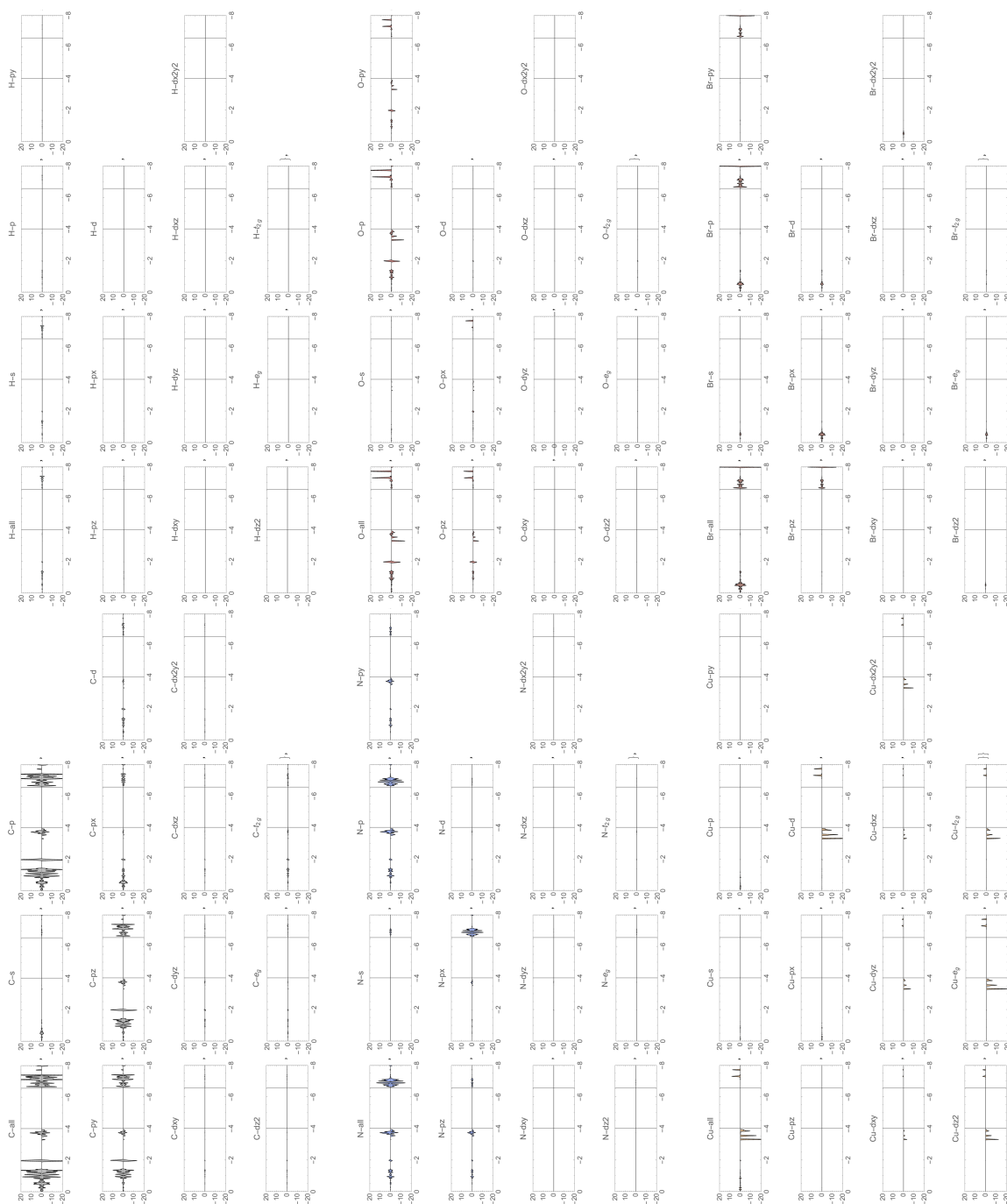


Figure B.10:  $r^2$ SCAN+rVV10/HSE06 detailed atomic orbital partial density of states of M5-Br-FM.

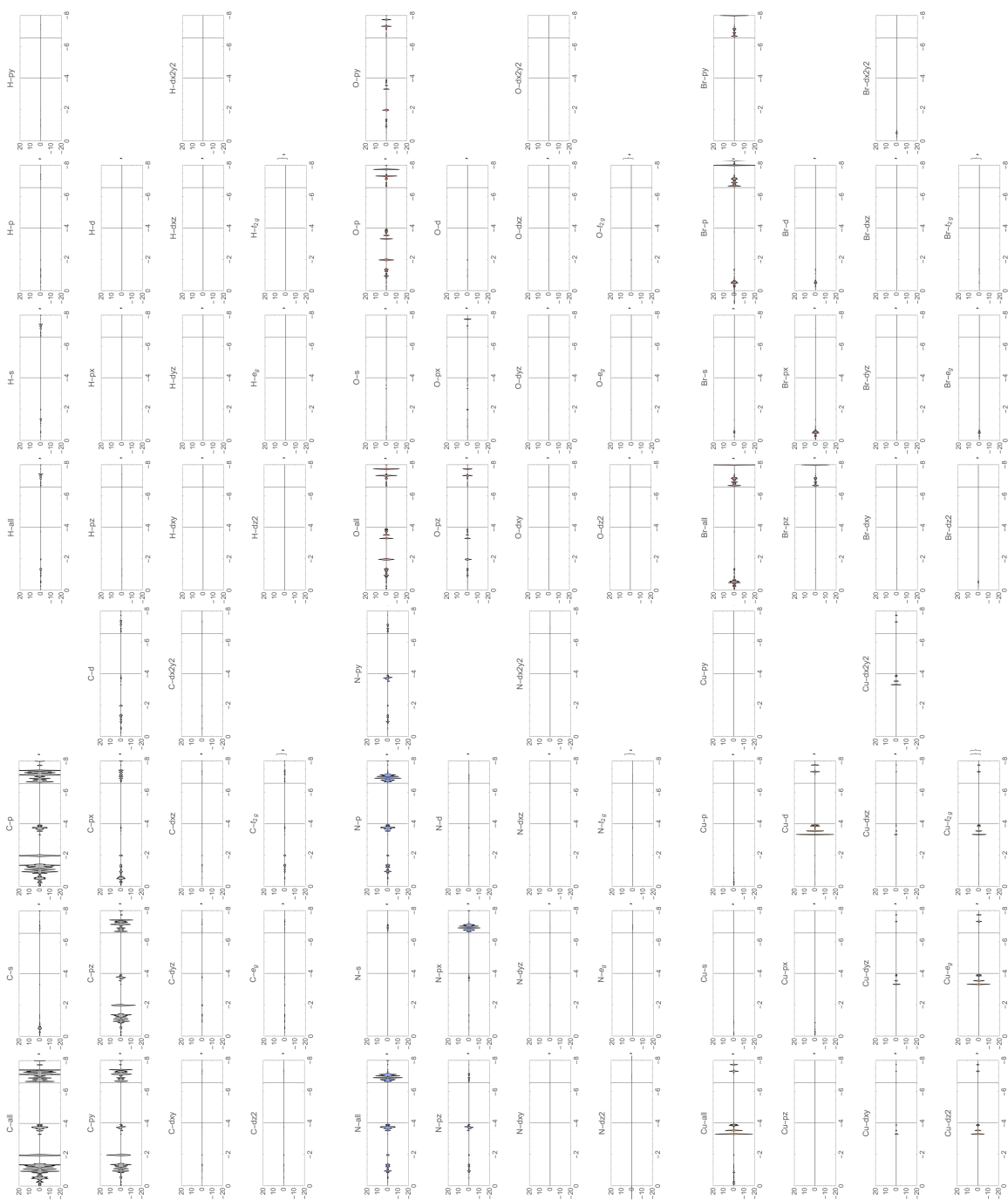
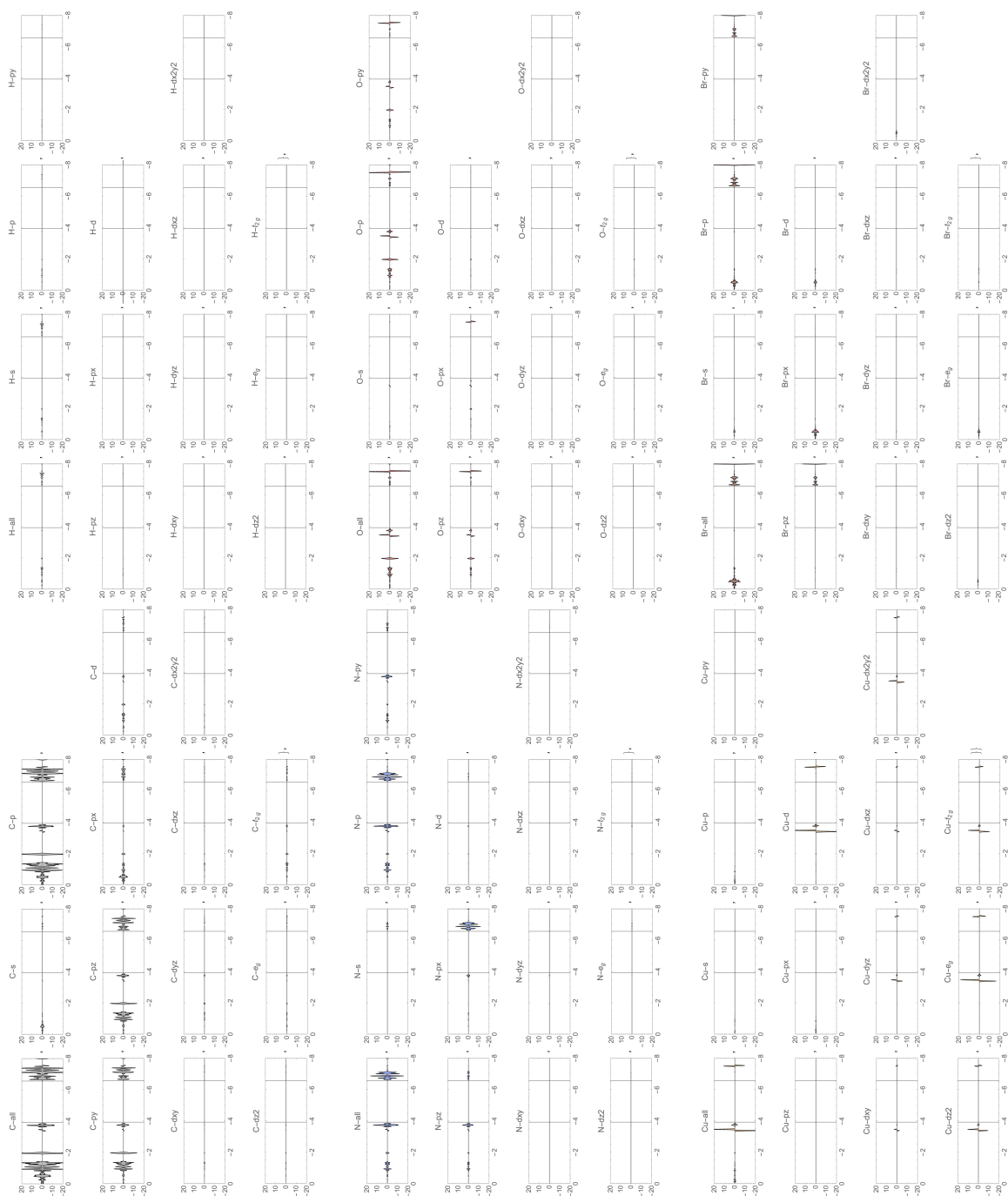


Figure B.11:  $r^2$ SCAN+rVV10//HSE06 detailed atomic orbital partial density of states of M5-Br-AFM1.

Figure B.12:  $r^2$ SCAN+rVV10/HSE06 detailed atomic orbital partial density of states of M5-Br-AFM2.

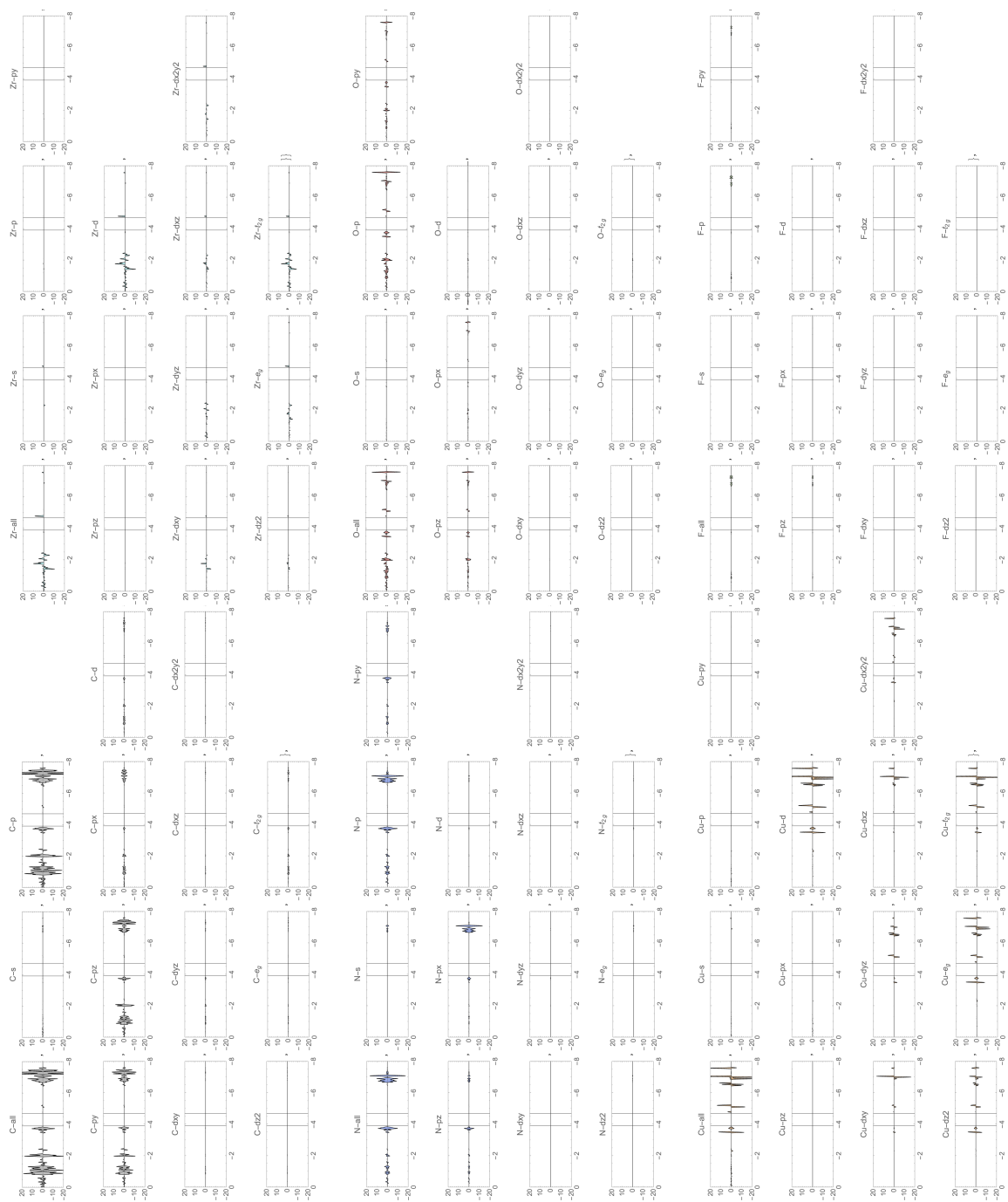
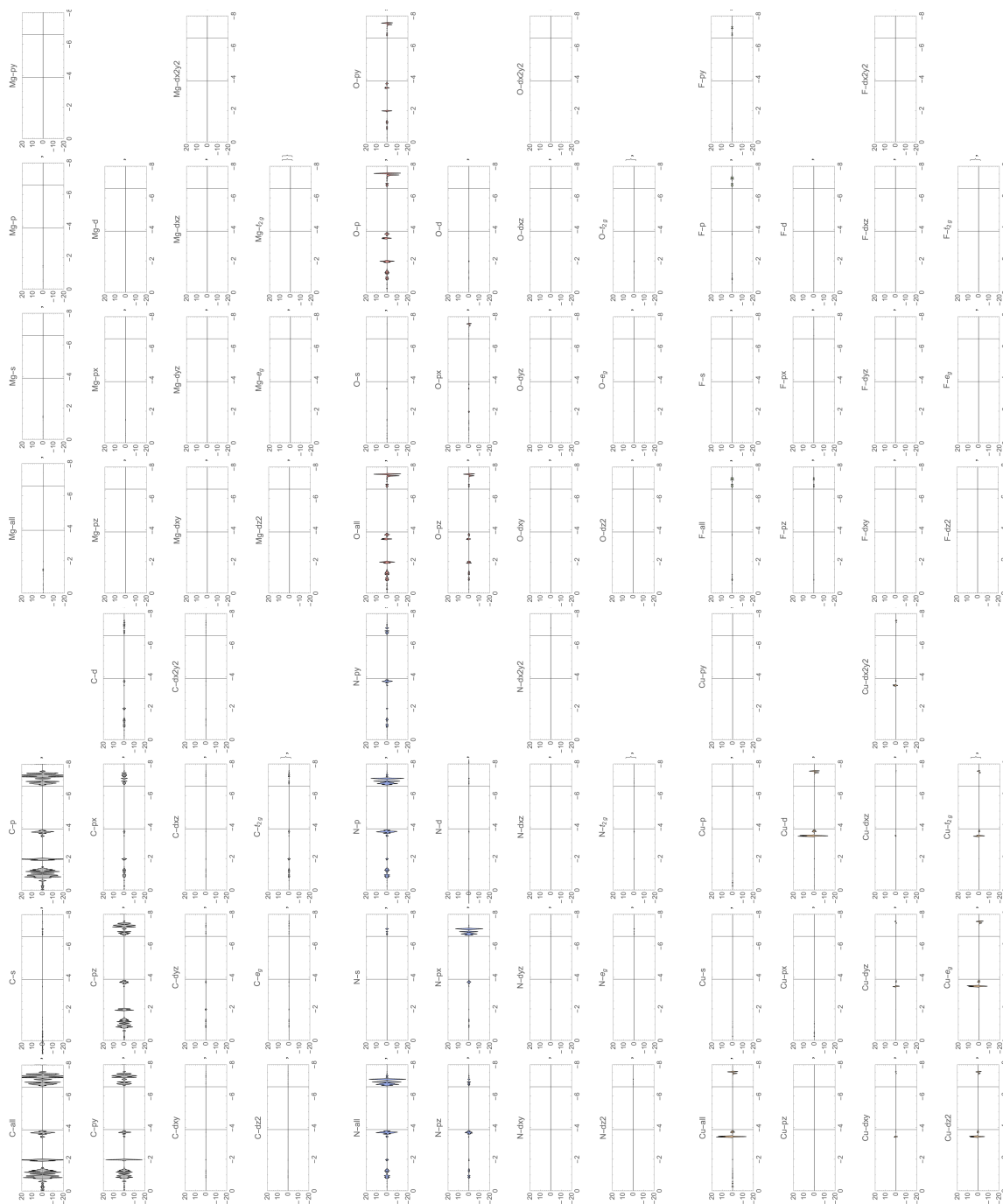


Figure B.13:  $r^2$ SCAN+rVV10/HSE06 detailed atomic orbital partial density of states of Def-Zr.

Figure B.14:  $r^2$ SCAN+rVV10/HSE06 detailed atomic orbital partial density of states of Def-Mg.



# Bibliography

- [1] Yaghi, O. M.; Kalmutzki, M. J.; Diercks, C. S. *Introduction to reticular chemistry: metal-organic frameworks and covalent organic frameworks*; John Wiley & Sons, 2019.
- [2] Mancuso, J. L.; Mroz, A. M.; Le, K. N.; Hendon, C. H. Electronic structure modeling of metal–organic frameworks. *Chemical reviews* **2020**, *120*, 8641–8715.
- [3] Wu, X.-P.; Gagliardi, L.; Truhlar, D. G. Cerium metal–organic framework for photocatalysis. *Journal of the American Chemical Society* **2018**, *140*, 7904–7912.
- [4] Feynman, R. *Feynman and computation*; CRC Press, 2018; pp 63–76.
- [5] Sholl, D. S.; Steckel, J. A. *Density functional theory: a practical introduction*; John Wiley & Sons, 2022.
- [6] Furukawa, H.; Cordova, K. E.; O’Keeffe, M.; Yaghi, O. M. The chemistry and applications of metal-organic frameworks. *Science* **2013**, *341*, 1230444.
- [7] Li, X.; Zhu, Q.-L. MOF-based materials for photo-and electrocatalytic CO<sub>2</sub> reduction. *EnergyChem* **2020**, *2*, 100033.
- [8] Silva, A. R.; Alexandre, J. Y.; Souza, J. E.; Neto, J. G. L.; de Sousa Júnior, P. G.; Rocha, M. V.; Dos Santos, J. C. The Chemistry and Applications of Metal–Organic Frameworks (MOFs) as Industrial Enzyme Immobilization Systems. *Molecules* **2022**, *27*, 4529.
- [9] Yaghi, O. M.; O’Keeffe, M.; Ockwig, N. W.; Chae, H. K.; Eddaoudi, M.; Kim, J. Reticular synthesis and the design of new materials. *Nature* **2003**, *423*, 705–714.
- [10] Kanan, D. K.; Carter, E. A. Band gap engineering of MnO via ZnO alloying: a potential new visible-light photocatalyst. *The Journal of Physical Chemistry C* **2012**, *116*, 9876–9887.



- 
- [11] Öhrström, L.; Amombo Noa, F. M. An improved water-harvesting cycle. *Science* **2021**, *374*, 402–402.
- [12] Giustino, F. *Materials modelling using density functional theory: properties and predictions*; Oxford University Press, 2014.
- [13] Hartree, D. R. The wave mechanics of an atom with a non-Coulomb central field. Part I. Theory and methods. 1928.
- [14] Hartree, D. R. The wave mechanics of an atom with a non-coulomb central field. Part II. Some results and discussion. 1928.
- [15] Hartree, D. R. The wave mechanics of an atom with a non-coulomb central field. part iii. term values and intensities in series in optical spectra. 1928.
- [16] Hohenberg, P.; Kohn, W. Inhomogeneous electron gas. *Physical review* **1964**, *136*, B864.
- [17] Kohn, W.; Sham, L. J. Self-consistent equations including exchange and correlation effects. *Physical review* **1965**, *140*, A1133.
- [18] Sousa, S. F.; Fernandes, P. A.; Ramos, M. J. General performance of density functionals. *The Journal of Physical Chemistry A* **2007**, *111*, 10439–10452.
- [19] Perdew, J. P.; Schmidt, K. Jacob's ladder of density functional approximations for the exchange-correlation energy. 2001.
- [20] Vosko, S. H.; Wilk, L.; Nusair, M. Accurate spin-dependent electron liquid correlation energies for local spin density calculations: a critical analysis. *Canadian Journal of physics* **1980**, *58*, 1200–1211.
- [21] Perdew, J. P.; Zunger, A. Self-interaction correction to density-functional approximations for many-electron systems. *Physical Review B* **1981**, *23*, 5048.
- [22] Perdew, J. P.; Burke, K.; Ernzerhof, M. Generalized gradient approximation made simple. *Physical review letters* **1996**, *77*, 3865.
- [23] Perdew, J. P.; Chevary, J. A.; Vosko, S. H.; Jackson, K. A.; Pederson, M. R.; Singh, D. J.; Fiolhais, C. Atoms, molecules, solids, and surfaces: Applications of the generalized gradient approximation for exchange and correlation. *Physical review B* **1992**, *46*, 6671.

- [24] Zhao, Y.; Truhlar, D. G. A new local density functional for main-group thermochemistry, transition metal bonding, thermochemical kinetics, and noncovalent interactions. *The Journal of chemical physics* **2006**, *125*, 194101.
- [25] Tao, J.; Perdew, J. P.; Staroverov, V. N.; Scuseria, G. E. Climbing the density functional ladder: Nonempirical meta-generalized gradient approximation designed for molecules and solids. *Physical review letters* **2003**, *91*, 146401.
- [26] Sun, J.; Ruzsinszky, A.; Perdew, J. P. Strongly constrained and appropriately normed semilocal density functional. *Physical review letters* **2015**, *115*, 036402.
- [27] Bartók, A. P.; Yates, J. R. Regularized SCAN functional. *The Journal of chemical physics* **2019**, *150*, 161101.
- [28] Furness, J. W.; Kaplan, A. D.; Ning, J.; Perdew, J. P.; Sun, J. Accurate and numerically efficient r2SCAN meta-generalized gradient approximation. *The journal of physical chemistry letters* **2020**, *11*, 8208–8215.
- [29] Furness, J. W.; Kaplan, A. D.; Ning, J.; Perdew, J. P.; Sun, J. Construction of meta-GGA functionals through restoration of exact constraint adherence to regularized SCAN functionals. *The Journal of Chemical Physics* **2022**, *156*, 034109.
- [30] Vydrov, O. A.; Van Voorhis, T. Nonlocal van der Waals density functional made simple. *Physical review letters* **2009**, *103*, 063004.
- [31] Sabatini, R.; Gorni, T.; De Gironcoli, S. Nonlocal van der Waals density functional made simple and efficient. *Physical Review B* **2013**, *87*, 041108.
- [32] Heyd, J.; Scuseria, G. E.; Ernzerhof, M. Hybrid functionals based on a screened Coulomb potential. *The Journal of chemical physics* **2003**, *118*, 8207–8215.
- [33] Kittel, C.; McEuen, P. *Introduction to solid state physics*; John Wiley & Sons, 2018.
- [34] Blundell, S. *Magnetism in condensed matter*. 2003.
- [35] Dirac, P. A. M. The quantum theory of the electron. *Proceedings of the Royal Society of London. Series A, Containing Papers of a Mathematical and Physical Character* **1928**, *117*, 610–624.

- [36] Dirac, P. A. M. The quantum theory of the electron. Part II. *Proceedings of the Royal Society of London. Series A, Containing Papers of a Mathematical and Physical Character* **1928**, *118*, 351–361.
- [37] Pauli Jr, W. On the quantum mechanics of magnetic electrons. *Nature* **1927**, *119*, 282.
- [38] Rajagopal, A.; Callaway, J. Inhomogeneous electron gas. *Physical Review B* **1973**, *7*, 1912.
- [39] vienna ab initio simulation package, <https://www.vasp.at/info/about/>
- [40] Birch, F. Finite elastic strain of cubic crystals. *Physical review* **1947**, *71*, 809.
- [41] Tyuterev, V.; Vast, N. Murnaghan's equation of state for the electronic ground state energy. *Computational materials science* **2006**, *38*, 350–353.
- [42] Tranchemontagne, D. J.; Hunt, J. R.; Yaghi, O. M. Room temperature synthesis of metal-organic frameworks: MOF-5, MOF-74, MOF-177, MOF-199, and IRMOF-0. *Tetrahedron* **2008**, *64*, 8553–8557.
- [43] Wang, C.; Xie, Z.; deKrafft, K. E.; Lin, W. Doping metal-organic frameworks for water oxidation, carbon dioxide reduction, and organic photocatalysis. *Journal of the American Chemical Society* **2011**, *133*, 13445–13454.
- [44] Alvaro, M.; Carbonell, E.; Ferrer, B.; Llabrés i Xamena, F. X.; Garcia, H. Semiconductor behavior of a metal-organic framework (MOF). *Chemistry—A European Journal* **2007**, *13*, 5106–5112.
- [45] others,, *et al.* DFTB+, a software package for efficient approximate density functional theory based atomistic simulations. *The Journal of chemical physics* **2020**, *152*, 124101.
- [46] Butler, K. T.; Hendon, C. H.; Walsh, A. Electronic chemical potentials of porous metal-organic frameworks. *Journal of the American Chemical Society* **2014**, *136*, 2703–2706.
- [47] Pattengale, B.; Yang, S.; Ludwig, J.; Huang, Z.; Zhang, X.; Huang, J. Exceptionally long-lived charge separated state in zeolitic imidazolate framework: implication for photocatalytic applications. *Journal of the American Chemical Society* **2016**, *138*, 8072–8075.